

Διερεύνηση ντετερμινιστικού  
μοντέλου ελικοειδούς εκτονωτή  
για διφασική εκτόνωση

Τομέας: Θερμότητας

Επιβλέπων: Σωτήριος Καρέλλας, Καθηγητής ΕΜΠ

Αθήνα 2021



AMALIA STEINHAUER

Investigation of a deterministic model of a scroll expander for wet expansion

**Section: Thermal Engineering**

**Supervisor: Sotirios Karellas, Professor**



SCHOOL OF MECHANICAL ENGINEERING

Athens 2021

## Preface

This diploma thesis was conducted in the context of my studies in the School of Mechanical Engineering in NTUA. To begin with, I would like to thank Professor Sotirios Karellas who trusted me and provided me with the great opportunity to engage in such an absorbing topic.

I am also extremely grateful to Postdoctoral Researcher Konstantinos Braimakis, MSc student Evropi Monokrousou and PhD Candidate Trifonas Roumpedakis for their continuous guidance and support. I thank them for their time given to answer to my questions. Their help constituted a key factor to compose and complete my diploma thesis and to have a deeper insight into the scroll expander technology.

Last but not least, I want to express my profound gratitude to my family-Mother, Father and Sister- for their unqualified support during my studies. Special thanks to my friends for their encouragement, and especially Chr. for his help and unconditional support.

Υπεύθυνη δήλωση για λογοκλοπή και για κλοπή πνευματικής ιδιοκτησίας:

Έχω διαβάσει και κατανοήσει τους κανόνες για τη λογοκλοπή και τον τρόπο σωστής αναφοράς των πηγών που περιέχονται στον οδηγό συγγραφής Διπλωματικών Εργασιών. Δηλώνω ότι, από όσα γνωρίζω, το περιεχόμενο της παρούσας Διπλωματικής Εργασίας είναι προϊόν δικής μου εργασίας και υπάρχουν αναφορές σε όλες τις πηγές που χρησιμοποίησα.

Ονοματεπώνυμο

Αμαλία Σταϊνχάουερ

## Contents

1.	Introduction .....	13
1.1	Compression and Expansion devices .....	13
1.1.1	Compressors.....	13
1.1.2	Expanders.....	13
1.2	Scroll expanders.....	18
1.2.1	General description .....	18
1.2.2	Applications of scroll machines .....	20
1.3	Literature review on expanders .....	23
1.3.1	Theoretical studies .....	23
1.3.2	Experimental studies .....	32
1.4	Thesis scope .....	40
2.	Deterministic model .....	41
2.1	Introduction into expander modelling .....	41
2.1.1	Deterministic model of scroll compressor/expander.....	42
2.1.2	Introducing PDSim .....	42
2.1.3	Adaptation of PDSim models.....	44
2.2	Scroll geometry .....	46
2.2.1	Scope .....	46
2.2.2	Two-Arc geometry.....	46
2.2.3	Arc-Line-Arc geometry.....	47
2.3	Deterministic model description .....	48
2.3.1	Flow models .....	48
2.3.2	Heat transfer and pressure drop models .....	53
2.3.3	Performance assessment indexes.....	58
2.3.4	Scroll energy balance .....	59
2.3.5	Deterministic model solution algorithm.....	60
2.3.6	Deterministic model limitations .....	62
3.	Deterministic model results and discussion .....	63
3.1	Commercial scroll expander simulation results.....	63
3.1.1	Investigation of heat transfer in the tubes.....	64
3.1.2	Investigation of pressure drop in the tubes.....	66
3.1.3	Investigation of leakages.....	68
3.1.4	Total influence of the internal losses .....	69
3.1.5	Parametric investigation of the influence of the rotational speed.....	71
3.1.6	Comparison between single-phase and two-phase flows .....	75
3.2	Prototype scroll expander simulation results.....	78
3.2.1	Investigation of involutes angles and inlet port areas .....	79
3.2.2	Investigation of inlet port area and built-in volume ratio.....	87
4.	Discussion .....	90

5. Future work.....	92
6. List of Tables.....	93
7. List of Figures .....	94
8. References .....	98

## Σύνοψη

Τα τελευταία χρόνια έχει γίνει μία στροφή προς εναλλακτικούς κύκλους παραγωγής ηλεκτρισμού, θέρμανσης και ψύξης. Προς αυτή την κατεύθυνση, η συγκεκριμένη διπλωματική εργασία εστιάζει στην προσομοίωση ενός κύκλου Ericsson. Συγκεκριμένα, η λειτουργία ενός ελικοειδούς εκτονωτή ερευνάται εκτενώς μέσω της ανάπτυξης ενός ντετερμινιστικού μοντέλου. Η δημιουργία αυτού του μοντέλου βασίζεται -στο υπάρχον PDSim- μοντέλο ανοικτού κώδικα και περιλαμβάνει την προσθήκη μοντέλων μεταφοράς θερμότητας και μοντέλων ροής εντός του PDSim. Αρχικά, μελετάται ένας ελικοειδής συμπιεστής ο οποίος λειτουργεί αντίστροφα, δηλαδή ως εκτονωτής. Η απόδοση του εκτονωτή που προκύπτει εξετάζεται με την αλλαγή διάφορων παραμέτρων, συμπεριλαμβανομένου του λόγου πίεσης, της ξηρότητας εισαγωγής και την περιστροφική ταχύτητα του εκτονωτή. Επιπρόσθετα, διερευνώνται οι επιδράσεις των εσωτερικών απωλειών στην απόδοση του εκτονωτή. Σύμφωνα με τα αποτελέσματα, όταν η ξηρότητα στην είσοδο του εκτονωτή είναι 0.8, ο μέγιστος ισεντροπικός βαθμός απόδοσης που αποδίδει ο εκτονωτής είναι σχεδόν 65%, ενώ μεγιστοποιείται στα 66% όταν ο λόγος πίεσης είναι ελαφρώς μεγαλύτερος από 3.3, ο οποίος αποτελεί και τον λόγο πίεσης του σημείου σχεδιασμού. Η πρόβλεψη ότι η επιρροή των διαρροών στην απόδοση του εκτονωτή είναι μεγαλύτερη από αυτή που ασκούν τα φαινόμενα μεταφοράς θερμότητας επιβεβαιώνεται και από τα αποτελέσματα. Η μεγαλύτερη πτώση στον βαθμό απόδοσης λόγω των διαρροών βρέθηκε ίση με 3%. Επίσης, η αύξηση της περιστροφικής ταχύτητας του εκτονωτή επηρεάζει αρνητικά την ισεντροπική του απόδοση, μειώνοντάς την από 81% για 3000 rpm σε 57% για 6000 rpm. Ακόμη, πιστοποιείται πως η λειτουργία του ρευστού R123zd(E) στη μονοφασική ροή οδηγεί σε μεγαλύτερη απόδοση συγκριτικά με τη λειτουργία του στη διφασική περιοχή. Στη συνέχεια, εισάγεται το γεωμετρικό μοντέλο ενός πρωτότυπου ελικοειδή εκτονωτή έτσι ώστε να εξεταστεί η επίδραση των γωνιών έναρξης της εσωτερικής και της εξωτερικής καμπύλης της σταθερής σπείρας και της επιφανείας εισόδου του εκτονωτή στον αδιαβατικό και στον ογκομετρικό βαθμό απόδοσης του εκτονωτή. Τέλος, μεταβάλλοντας των εσωτερικό λόγο όγκων και την επιφάνεια εισόδου στον εκτονωτή ταυτόχρονα για την περίπτωση κατά την οποία ο αδιαβατικός βαθμός απόδοσης βελτιστοποιείται, εκτιμώνται οι αλλαγές οι οποίες συντελούνται στην απόδοση του πρωτότυπου εκτονωτή.

## Abstract

In recent years, the alternative trigeneration cycles constitute a promising technology to produce electric, heating and cooling power. For this reason, this diploma thesis is focused on the simulation of an Ericsson cycle. More specifically, the operation of a scroll expander has been studied extensively by applying a deterministic model. The development of this model is based on the existing open-source PDSim model and is conducted by integrating the heat transfer and flow models. Firstly, a commercial scroll compressor model considering its use in reverse as an expander is investigated. The performance of this scroll expander is examined by changing several parameters, namely the pressure ratio, the inner vapor quality and the rotational speed of the expander. The effects of the internal losses on the expander efficiency are also estimated. According to the results, when the inlet vapor quality is 0.8, the commercial expander exhibits its maximum isentropic efficiency equal to just below 65%, while it peaks at 66% for a pressure ratio of a little more than 3.3, which constitutes the design one. The prediction that leakages influence the expander performance more than heat transfer is verified by the results, with the highest degradation due to leakages being found at 3%. Additionally, the increase in the rotational speed exerts profoundly negative impacts on the isentropic performance of the expander, dropping from 81% for 3000 rpm to 57% for 6000rpm. Also, it is verified that the single-phase operation of R1233zd(E) leads to higher expander performance comparing to the respective two-phase. Subsequently, the geometrical model of a prototype scroll expander is applied to examine the influences of the inner and outer starting involute angles of the fixed scroll and inlet port area on the adiabatic and volumetric efficiencies. Finally, by altering the built-in volume ratio and the inlet port area of the prototype expander concurrently for the case of maximum adiabatic efficiency, the changes in the scroll expander performance are reexamined.



## Nomenclature

$A$	Area	$m^2$
$A_{port}$	Inlet port area	$m^2$
$A_{shell}$	Shell external surface	$m^2$
$a$	Heat transfer coefficient in the tube	$W/m^2/K$
$\alpha_{1\varphi}$	Single-phase heat transfer coefficient	$W/m^2/K$
$\alpha_{2\varphi}$	Two-phase heat transfer coefficient	$W/m^2/K$
$\alpha_{co}$	Two-phase heat transfer coefficient for condensation	$W/m^2/K$
$\alpha_l$	Pure liquid heat transfer coefficient	$W/m^2/K$
Bo	Boiling number	-
Co	Convection number	-
$c_p$	Specific heat	$kJ/kg/K$
$D$	Inner tube diameter	$m$
$d$	Distance between centers of arcs in discharge region	$m$
$F$	Parameter of evaporation	-
$F_{rl}$	Froude number	-
$f$	Friction factor	-
$G$	Mass flux	$kg/m^2/s$
$g$	Gravitational acceleration	$m/s^2$
$h_1$	Enthalpy in the inlet of the expander	$kJ/kg$
$h_2$	Enthalpy in the outlet of the expander	$kJ/kg$
$h_{2s}$	Isentropic enthalpy in the outlet of the expander	$kJ/kg$
$h_{amb}$	Convection heat transfer coefficient shell/ambient	$W/m^2/K$
$h_{disc}$	Discharge enthalpy	$kJ/kg$
$h_{disc,a}$	Assumed discharge enthalpy	$kJ/kg$
$h_{fg}$	Vaporization enthalpy	$kJ/kg$
$h_{mean}$	Mean enthalpy	$kJ/kg$
$h_s$	Scroll height	$m$
$K$	Entrainment slip ratio	-
$K_e$	Effective slip ratio	-
$k$	Thermal conductivity	$W/m/K$
$k_f$	Refrigerant thermal conductivity	$W/m/K$
$L$	Tube length	$m$

$M$	Ratio of isentropic nozzle to real mass flow rate	-
$\dot{m}$	Mass flow rate	kg/s
$\dot{m}_{nozzle}$	Mass flow rate of the isentropic nozzle	kg/s
$\dot{m}_{ref}$	Refrigerant mass flow rate	kg/s
$N$	Parameter of evaporation	-
$Nu$	Nusselt number	-
$n$	Rotational speed	rpm
$Pr_f$	Prandtl refrigerant number	-
$p^*$	Ratio of saturation to critical pressure	-
$p_{ratio}$	Pressure ratio	-
$p_{up}$	Upstream pressure of the flow path	kPa
$\dot{Q}_{amb}$	Heat flux shell/ambient	W
$\dot{Q}_{CV}$	Heat flux among the CVs	W
$\dot{Q}_{wall}$	Heat flux shell/working fluid	W
$\dot{Q}_{tubes}$	Heat flux tubes/working fluid	W
$Re$	Reynolds number	-
$Re_D$	Reynolds number for $D$ hydraulic diameter	-
$Re_{dh}$	Reynolds number for $d_h$ tube hydraulic diameter	-
$r_{HT}$	Residual of the scroll energy balance	W
$r_{a1}$	Radius of arc 1 in discharge region	m
$r_{a2}$	Radius of arc 2 in discharge region	m
$r_b$	Radius of base cycle	m
$r_0$	Orbiting radius	m
$s_r$	Arc length of leakage path	m
$T_{amb}$	Ambient temperature	°C
$T_f$	Fluid temperature	°C
$T_{inlet}$	Inlet temperature	°C
$T_{mean}$	Mean temperature	°C
$T_{outlet}$	Outlet temperature	°C
$T_{wall}$	Wall temperature	°C
$VR$	Volume ratio	-
$V_{disp}$	Displacement volume of expander	$m^3$
$V_{ratio}$	Volume ratio	-

$v_g$	Specific volume of saturated gas	$m^3/kg$
$v_l$	Specific volume of saturated liquid	$m^3/kg$
$\dot{W}_{el}$	Net electrical power	W
$\dot{W}_{mech}$	Mechanical power	W
$\dot{W}_{ml}$	Mechanical losses	W
$\dot{W}_{motor,los}$	Motor losses	W
$\dot{W}_{PV}$		W
$x$	Vapor quality	-
$x_{a1}$	x-coordinate for center of arc 1	m
$x_{a2}$	x-coordinate for center of arc 2	m
$x_{fis}$	x-coordinate for fixed inner starting angle	m
$x_{fos}$	x-coordinate for fixed outer starting angle	m
$x_{inlet}$	Inlet vapor quality	-
$y_{a1}$	y-coordinate for center of arc 1	m
$y_{a2}$	y-coordinate for center of arc 2	m
$y_{fis}$	y-coordinate for fixed inner starting angle	m
$y_{fos}$	y-coordinate for fixed outer starting angle	m
<b><u>Greek Symbols</u></b>		
$\delta_f$	Flank gap	m
$\delta_r$	Radial gap	m
$\varepsilon$	Surface roughness	m
$\eta_{ad}$	Adiabatic efficiency	-
$\eta_g$	Generator efficiency	-
$\eta_{is}$	Isentropic efficiency	-
$\eta_{ml}$	Mechanical efficiency	-
$\eta_{vol}$	Volumetric efficiency	-
$\theta$	Crank angle	rad
$\mu$	Viscosity	Pa/s
$\mu_f$	Refrigerant viscosity	Pa/s
$\xi$	Cross-over term	-
$\rho_{crit}$	Critical density	$kg/m^3$
$\rho_f$	Refrigerant density	$kg/m^3$
$\rho_g$	Density of saturated vapor	$kg/m^3$
$\rho_{inlet}$	Inlet density	$kg/m^3$
$\rho_{up}$	Density of the upstream flow	$kg/m^3$

$\rho_l$	<i>Density of saturated liquid</i>	$kg/m^3$
$\rho_{sat}$	<i>Saturation density</i>	$kg/m^3$
$\sigma$	<i>Ratio of upstream to downstream area</i>	-
$\phi$	<i>Involute angle</i>	$rad$
$\varphi_{i0}$	<i>Inner involute initial angle</i>	$rad$
$\varphi_{ie}$	<i>Inner involute ending angle</i>	$rad$
$\varphi_{is}$	<i>Inner involute starting angle</i>	$rad$
$\varphi_{o0}$	<i>Outer involute initial angle</i>	$rad$
$\varphi_{oe}$	<i>Outer involute ending angle</i>	$rad$
$\varphi_{os}$	<i>Outer involute starting angle</i>	$rad$
$\psi$	<i>Entrainment factor</i>	-
$\psi_{bs}$	<i>Parameter for the calculation of entrainment factor</i>	-
$\psi_{cb}$	<i>Convective boiling number</i>	-
$\psi_{nb}$	<i>Nucleate boiling number</i>	-
$\omega$	<i>Rotational speed</i>	$rad/s$
<u>Acronyms</u>		
CV	<i>Control Volume</i>	
ORC	<i>Organic Rankine Cycle</i>	
VCC	<i>Vapor Compression Cycle</i>	

## 1. Introduction

### 1.1 Compression and Expansion devices

#### 1.1.1 Compressors

Not only do compressors contribute to the fluid pressure increase from the evaporating pressure to the condensation pressure, but they also facilitate the circulation of working fluid through the vapor compression cycle. There are two generic principles for compression of air or gas, positive displacement compression and dynamic compression.

In positive displacement compressors, the volumes are decreased and increased kinematically. This implies that one position input regulates the compression volumes positively. Positive displacement compressors include piston, screw, tooth and scroll compressors.

On the other hand, dynamic compression is conducted due to dynamic forces and takes place constantly. This kind of compressor accelerates the air flow, converting the velocity head into pressure. The capacity of a dynamic compressor changes in accordance with the working pressure. Dynamic compressors can be characterized either as axial or centrifugal. In axial compressors, the acceleration of air is achieved due to the action of a bladed rotor, covered at the blade ends. In centrifugal compressors, one or more impellers are rotated, and as a result, the air is accelerated. [1]

Positive displacement compressors are more suitable for small/medium-scale applications, such as Organic Rankine Cycle, air conditioning, refrigeration and water heating, because of their lower design volumes, higher pressure ratios and lower rotational speed in comparison with dynamic compressors.

#### 1.1.2 Expanders

There are two main categories of expanders, positive displacement (or volumetric) and dynamic (or turbines), depending on their operating principle, shown in Figure 1.




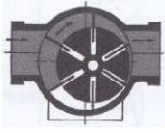



volumetric expanders $work = \int v dp$				dynamic expanders $work \sim u^2$		
						
piston	screw	scroll	vane	axial	cantilever	radial

Figure 1. Types of expanders [2]

Turbines increase the internal energy of the fluid by using rotating blades. In this case, pressure and forces are quite low, but there are high flow velocities. Dynamic turbomachines are divided into axial, cantilever and radial. [2] The axial turbines differ from radial due to the fact that any change in average flow radius occurs in the first. For this reason, the axial turbines are appropriate to manage high mass flows; however, the expansion ratio, which these turbines can handle in an efficient way, is limited. On the other hand, the simple flow path through the machine allows the use of multistage axial turbines, in which high pressure ratios are reached. In an axial turbine, the flow passes through the impulse and the reaction stages. In the impulse stage, the total pressure drop realized by stator converging nozzle design, to accelerate flow and decrease pressure. On the other hand, rotor blades change the flow direction, but the pressure remains constant. The force that moves rotor blades is caused partially by flow impingement and reaction due to the flow acceleration at the last convergent part. In radial turbines, because of stator blades, the flow is deflected and enters the rotor with a high peripheral component of absolute velocity. Turbine expanders are usually efficient for large-scale systems with an output power above 50 kW. [3]

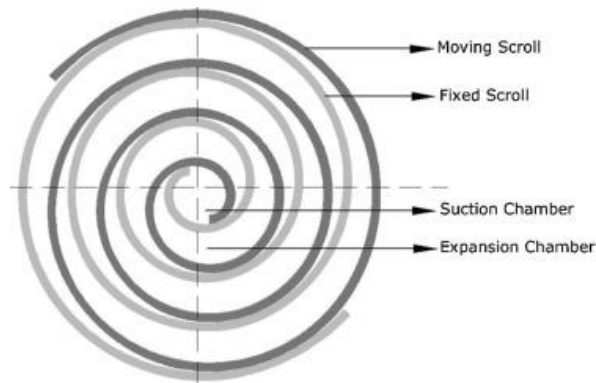
On the other hand, volumetric expanders produce mechanical work by altering the volume of a working chamber. These expanders are more suitable for high pressures, huge forces, relatively low rotational speeds and small flow velocities, and consequently, positive displacement expanders are more favorable for small ORC applications.

In the following, an analysis of the main types of volumetric expanders used in ORC applications is included.

#### 1.1.2.1 Scroll expanders

Scroll expanders are positive displacement machines with orbital motion. Due to the wide use of scroll compressors in refrigeration, air conditioning and heat pump applications, it is common to modify scroll machines and create scroll type expanders from them for commercial and scientific purposes. This type of expander is involved in small-scale power generation units, below 50 kWe, with a representative value of isentropic efficiency equal to 65% [4]. However, in applications with low power output, namely below 10 kW, scroll expanders are cost-effective. In general, their overall isentropic efficiency can be as high as 87%. [5]

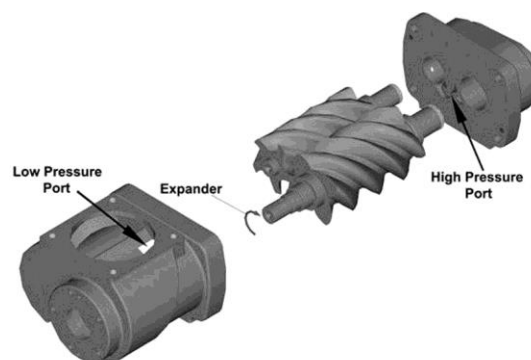
The geometrical model of scroll expanders is based on Archimedean spirals using the same generating circle and separated by a given offset. Scroll expanders consist of a fixed and an orbiting wrap. In Section 1.2.1, the operating principle of a scroll expander is described.



**Figure 2.**Typical schematic of a scroll expander [6]

### 1.1.2.2 Screw expanders

Being a positive displacement type, screw expanders can substitute turbo machines because of their high efficiency, high pressure ratio, low rotational speed and tolerance of two-phase fluids. [7] A single-screw expander consists of a screw and two symmetrically collocated planar gate rotors. The working process is carried out concurrently on both sides of the main rotor, and as a result, only the one side of the rotor is mainly analyzed in the literature. The screw expander operation is linked to the variation of volumetric rates in three dimensions. That means that the intake port is located at the top of the housing. In this stage, the fluid enters the screw expander with high pressure and moves towards the rear edge by increasing its volume. When a total revolution of chambers occurs, the volume of the chamber is at its maximum and the fluid covers the entire length of the screws. The exhaust port of a single screw expander is constructed in the bottom of the housing. As a result, the mixture of lubrication oil and working fluid flows from the high-pressure to the low-pressure edge and circulates smoothly in the system.



**Figure 3.**The principle of a single- screw expander [8]

The low leakages at the intake port are attributed to the minor clearance volume. For an efficient operation of a screw expander it is necessary to exist an adequate area between the screws in

order to prevent working fluid, which does not produce work, entering. The extension of the paths between the two lobes facilitates the rising of the fluid displacement per revolution. Moreover, the interaction between the screws provokes contact forces, and as a result, friction losses. In contrast with scroll expanders, screw expanders can achieve much higher rotational speeds due to the uninterrupted rotation of all moving parts during the expansion process.

Screw expanders are more appropriate for applications with a power output higher than 3.5 kW and up to 200 kW [9], [10]. The isentropic efficiencies fluctuate from 27.3% to 56.35% based on several scientific data [11], whereas state-of-the-art models reach 70%. [5] Both scroll and screw expanders can present over or under expansion, because they have a specific internal built-in volume ratio.

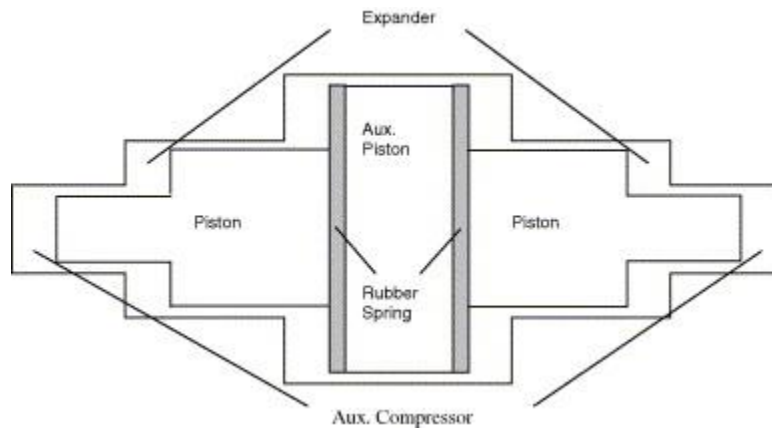
### 1.1.2.3 Piston expanders

Among the different types of positive displacement expanders, the piston-type shows some advantages over the others, such as higher built-in volume ratio, high achievable operating pressures and temperatures, their ability to take in liquid and low rotational speeds. Piston expanders are suitable for applications with low volume flow rates and low power production. The improvement of a piston expander performance can be reached applying many technics, such as expansion in stages with three coupled pistons. The disadvantage of this method is the increase of cost and construction complexity.

Piston expanders can present high internal volume ratios and their values fluctuate from 6 to 14, while their power output can reach 2 MW [12], [5]. Due to their high internal volume ratios, piston expanders can sustain large pressure ratios with reasonable efficiencies. In general, pressure ratios for piston expanders are higher than 4.5 [13]. However, these expanders only deal with restricted wet expansion. The shaft speed at maximum efficiency is 3000rpm for this type of volumetric expanders. According to [5], in case of piston expanders, the maximum pressure is achieved before the higher possible temperature. This means that the supply pressure is forced to be the highest one, and respectively, the supply temperature is increased in order to satisfy the broad range of power.

Inlet and outlet valves are adjusted in the piston expanders in order to regulate suction and discharge processes. A piston expander contains two cylinders which form four chambers. The high-pressure working fluid enters from the inlet valves towards the center and the piston is imposed to move. This motion results in work production.





**Figure 4. Schematic of piston expander structure [14]**

Taking all the above into account, as well as the data presented in [5], the subsequent table, Table 1, can be created.

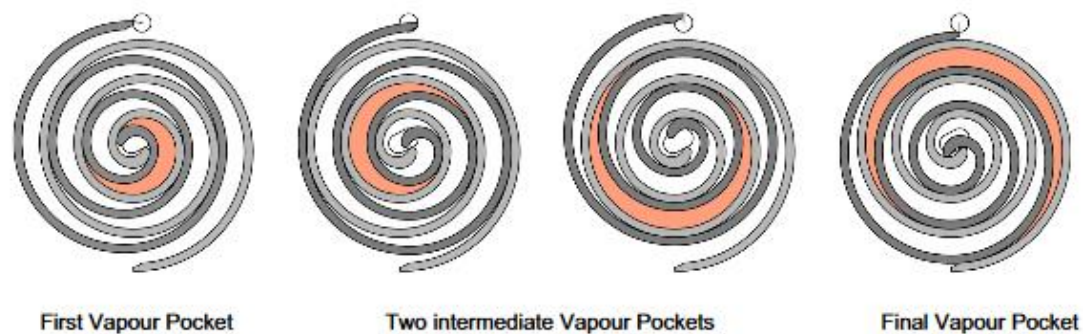
**Table 1. Working range for innovative scroll, screw and piston expanders [5]**

Variable	Scroll	Screw	Piston
Maximum Electrical Power	10 kW	200 kW	2 MW
Maximum Isentropic Efficiency	87%	70%	84%
Built-in Volume Ratio	1.5-3.5	n.a.-8	6-14
Maximum Rotational Speed	10000 rpm	21000 rpm	3000 rpm
Maximum Inlet Temperature	165 °C for air 215 °C for water vapor	490 °C for water vapor	500 °C
Maximum Pressure	40 bar	-	70 bar

## 1.2 Scroll expanders

### 1.2.1 General description

In this section, the operating principles of the scroll expanders are described. Each expansion chamber volume (i.e. the chambers enclosed by the walls of the two scrolls) changes during an expansion cycle, because of the continuous circular motion, as illustrated in Figure 5. The working fluid enters the machine at the central suction chamber at high temperature and pressure, forcing the orbiting scroll to rotate as it expands in the chambers of increasing volume. At the end of this process, the working fluid passes in the discharge stage and exits the wraps at the discharge chambers.



**Figure 5. Operating principle of a scroll expander [15]**

The built-in volume ratio of the scroll expander is the ratio of the volumes of the discharge and suction chambers. The volume ratio should be attuned to the volume expansion ratio of the working fluid based on its imposed to prevent under or over expansion. Under- expansion, Figure 6(a), takes place when the system specific volume ratio is higher than the internal built-in volume ratio of the expander. In that case, the pressure in the discharge line is lower than the pressure in the expansion chamber at the end of the expansion. On the contrary, over-expansion, Figure 6(b), happens when the imposed volume ratio to the expander is lower than the internal volume imposed by the expander. Consequently, the pressure in the discharge line is higher than the pressure in the expansion chamber at the end of the expansion. [16]

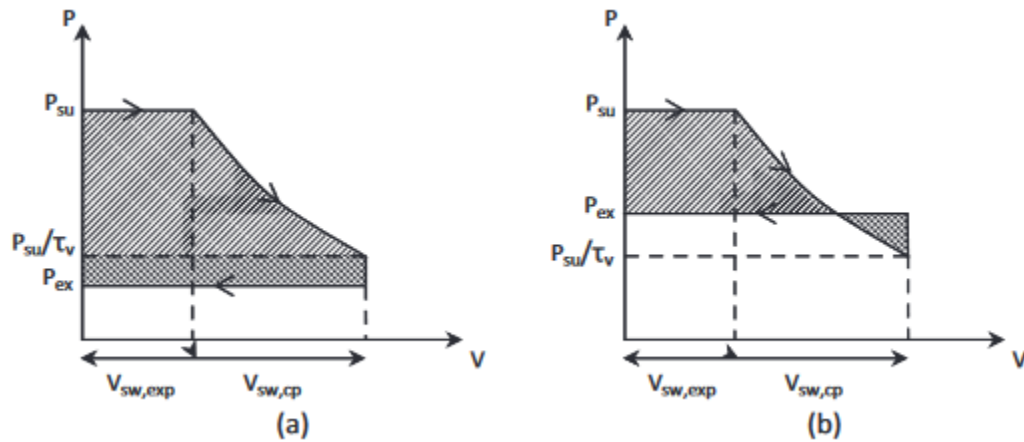


Figure 6. Under (a) and over (b) expansion losses [15]

Despite the benefits of a scroll expander working on a small-scale application, there are also some significant disadvantages. These drawbacks are associated with the existence of a tight manufacturing tolerance that ensures the suitable adjustment between the two scrolls. In case of failure, there is a huge flank clearance between the moving parts. According to [15], internal leakages, which occur in this situation, affect the isentropic efficiency of a scroll expander negatively. There are two types of leakages, flank and radial. The path caused due to the clearance between the flanks of scroll profiles, can be characterized as flank leakage  $\delta_f$ . Radial leakages are connected with the clearance between the bottom and the top layers of scrolls  $\delta_r$ , as depicted in Figure 7.

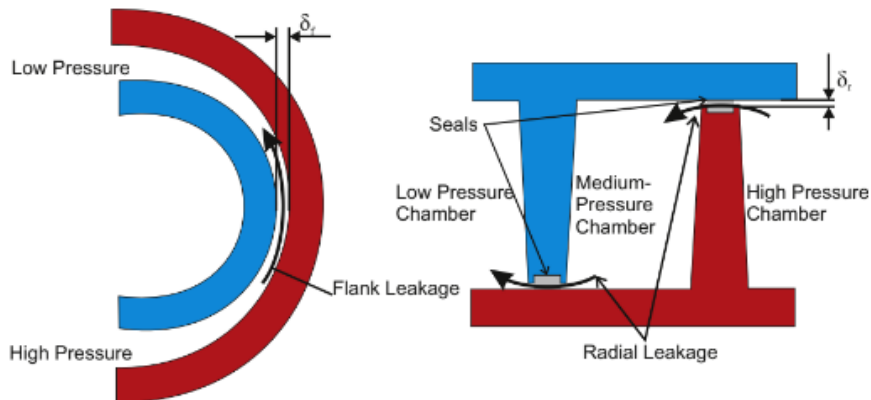


Figure 7. Flank and radial leakages occurring in a scroll expander [17]

## 1.2.2 Applications of scroll machines

First of all, it should be mentioned that scroll expanders are not used commercially. There are only commercial scroll compressors involved in Vapor Compression Cycles. Consequently, scroll expanders are constructed by modifying the respective compressors to work in a reverse mode for Organic Rankine Cycle configurations.

### 1.2.2.1 Vapor Compression Cycle

The main application of the VCC is in chillers and heat pumps. The working fluid circulates through four stages in which it is successively compressed (power input to the cycle), condensed (heat rejection), throttled (pressure/temperature drop) and evaporated (heat absorption).

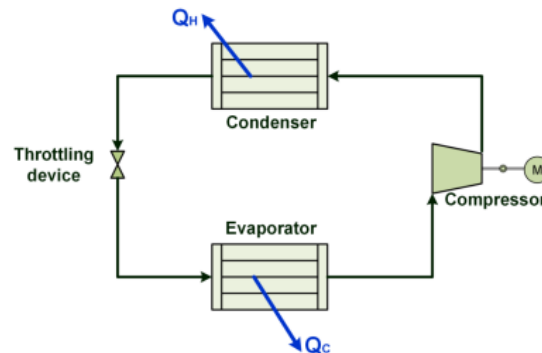
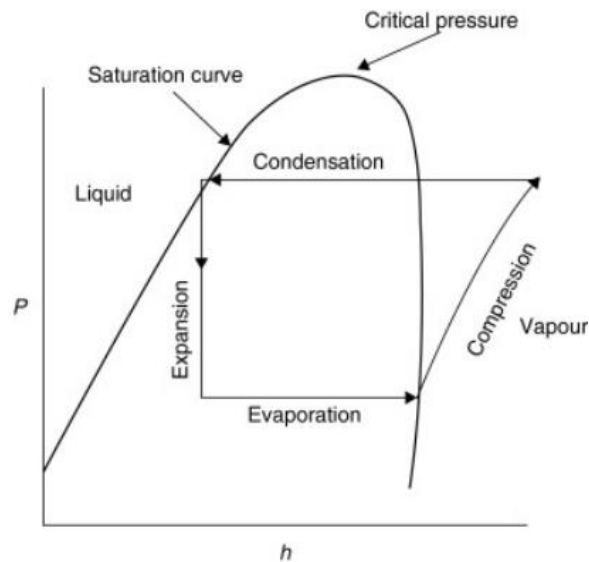


Figure 8. Vapor Compression Cycle configuration using expansion valve

A vapor compression cycle consists of four main components:

- a compressor
- a condenser
- a thermal expansion valve
- an evaporator



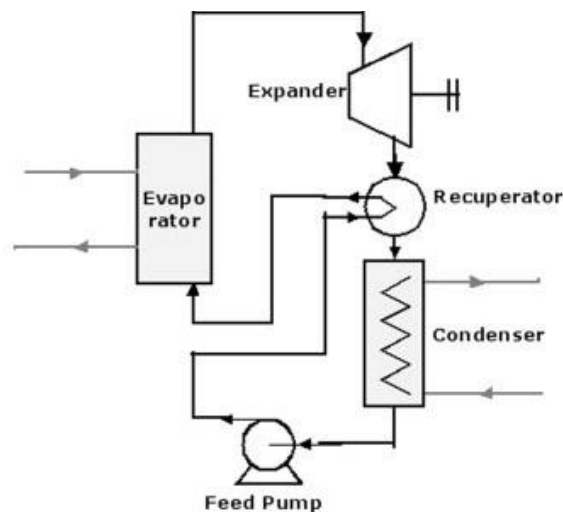
**Figure 9.P-h diagram for Vapor Compression Cycle**

The refrigerant enters the compressor as saturated vapor. In this stage the working fluid is compressed to a higher pressure with the simultaneous increase of its temperature and enthalpy. The compressed vapor refrigerant, in the thermodynamic state of superheated vapor, is next condensed. The condensation takes place in a heat exchanger, where heat is expelled from the refrigerant to cooling water or cooling air. This stage is usually completed when the working fluid becomes saturated liquid. Then the refrigerant is forced to flow through the expander or the thermal expansion valve where it is subjected to a sudden pressure reduction. As a result, the fluid temperature becomes lower and the refrigerant enters the two-phase region with the concurrent acquisition of the corresponding properties. The liquid and vapor mixture are then routed through the evaporator. The mixture absorbs the heat from the ambient air with the assistance of fans. Therefore, the evaporation and the saturation of working fluid happen and the VCC is finalized. Moreover, the ambient air is cooled in a specific temperature which is determined by the required conditions for the enclosed space.

### 1.2.2.2 ORC technology

ORCs are capable of absorbing heat from low energy and temperature sources (<300 °C) to produce electricity [18]. Therefore, heat sources characterized by low-grade energy, such as geothermal, solar energy, heat absorbed from biomass combustion, waste heat recovery from divergent industrial activities and heat from diesel engines, are suitable for ORC applications. This cycle differs from the conventional Rankine cycle in terms of the working fluid; namely, ORCs utilize organic fluids instead of water as working fluids. These fluids present lower critical temperatures and pressures than water. ORC configurations constitute also an attractive and sustainable solution for small-scale decentralized combined heat and power production (CHP).

Figure 10 illustrates the main parts that compose a plain recuperative ORC configuration. A feed pump contributes to the pressure increase of working fluid and facilitates its passing through the regenerator, in which the refrigerant is preheated. The incorporation of a regenerator in an ORC is not always feasible. It is necessary that the outlet turbine temperature is quite higher than the outlet pump temperature. After this stage, the working fluid is evaporated and superheated, reaching its maximum temperature. An expander connected with a generator expands the working fluid. It should be highlighted that there are no commercial scroll expanders. There are only commercial scroll compressors that can be modified and used in ORC systems as expanders if their operation is reversed. The condensation stage of the desuperheated vapor takes place in a condenser.



**Figure 10.** Typical ORC configuration

In order to select the working fluid of an ORC application, environmental factors and availability should be taken into account. The environmental factors are associated with the global

warming, a low GWP value is desired, and ozone layer, the ODP value should be exact or almost zero. Among the divergent refrigerants, their saturation temperatures determine to what extent they are suitable to be used for each ORC application. Figure 11 shows the T-s diagrams of some organic fluids.

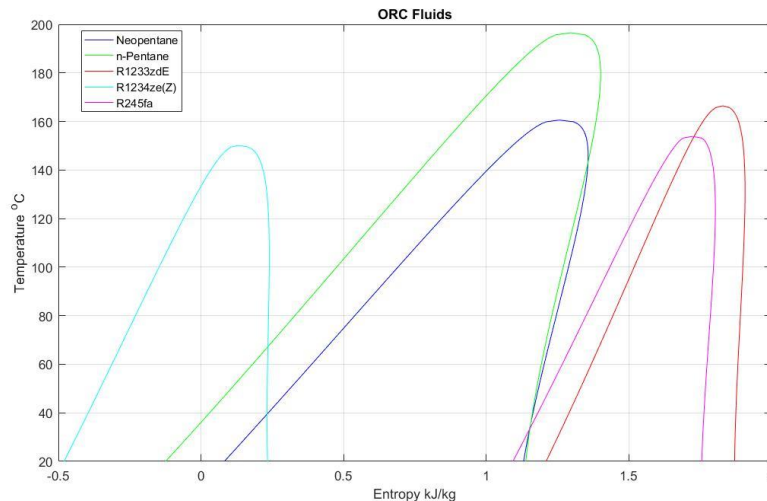


Figure 11. T-s diagrams for neopentane, n-Pentane, R1233zd(E), R1234ze(Z) and R245fa

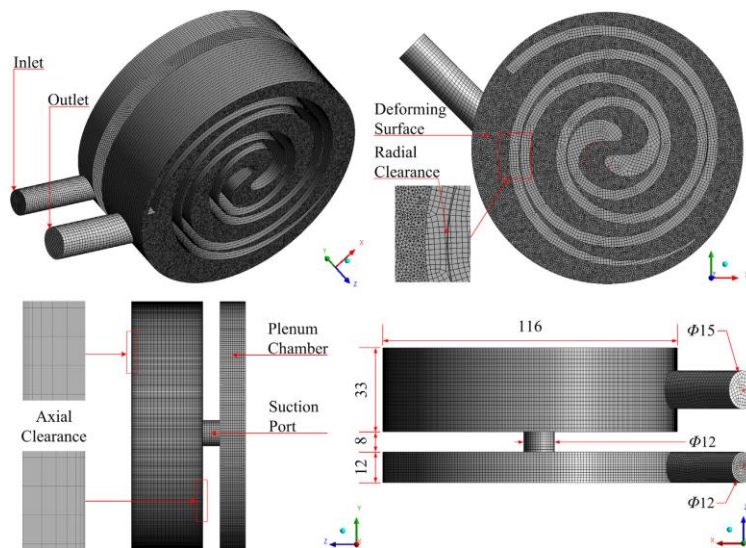
### 1.3 Literature review on expanders

Several studies have been conducted to investigate the influence of scroll expander features and flow characteristics on expander performance, and as a result, overall system efficiency. Computational Fluid Dynamic (CFD) and numerical simulations are performed on scroll expanders based on theoretical models to predict the general behavior of an expander and system.

#### 1.3.1 Theoretical studies

P. Song et al. [19] and M. Wei et al. [20] have engaged in a scroll expander for a small-scale ORC system. The calculation of transient characteristics of the aerodynamic variables, such as pulsating mass flow rate through the suction port, asymmetric spread of the internal flow, gas forces and applied moments on the orbiting scroll are described in detail on these papers. For a known geometrical formation, the unsteady flow has been examined in the suction stage of a scroll expander, in which the circulated refrigerant was R123. Moreover, the finite volume method has been used for the simulation. The flow model and the dynamic mesh were constructed based on the Reynolds Averaged Navier-Stokes turbulence model. To increase the precision for rapidly strained flows and whirling flows, they introduced k-epsilon model. The

main simulated operation conditions were the inlet temperature (132 °C), suction pressure (11 bar), discharge static pressure (4.4 bar) and rotational speed (2000 rpm). It was also estimated how the grid density affects the efficiency of the scroll expander. For different grid numbers, namely  $56 \times 10^4$ ,  $82 \times 10^4$  and  $125 \times 10^4$ , the corresponding expander efficiency is estimated equal to 40.5%, 41.7% and 41.8% respectively.



**Figure 12.**Computational domain of Wei's scroll expander model [20]

Kim et al. [21] presented the influence of the incorporation of a combined scroll expander-compressor unit in a two-stage compression  $\text{CO}_2$  trans-critical cycle on the COP of the cycle. This design leads to the recovery of throttling losses, and as thus, the improvement of the total COP was achieved. Apropos the scroll expander simulation, the isentropic, volumetric and mechanical efficiencies were assumed equal to 90%, 85% and 90% respectively. The initial design conditions were restricted by the suction pressure (3.5 MPa), discharge pressure (10 MPa) and expander inlet temperature (35°C). The rotational speed was regulated constantly at 2000rpm. In this case the isentropic efficiency of the scroll expander was 86.12%. Then, the effect of scroll expander suction and discharge pressure on the performances was examined, as it can be shown in Figure 13 and Figure 14.



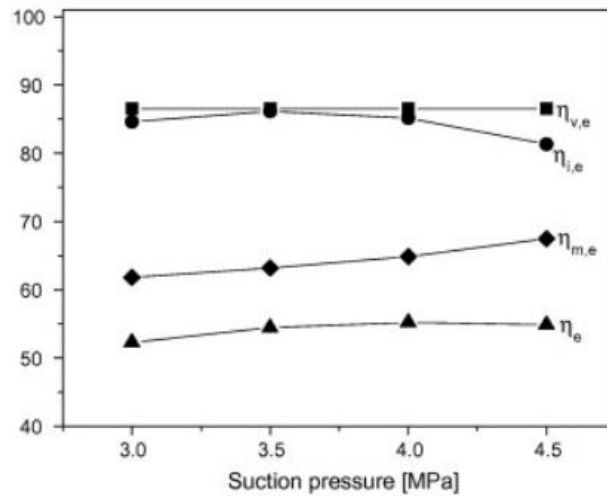


Figure 13. Scroll expander efficiencies for different suction pressures [21]

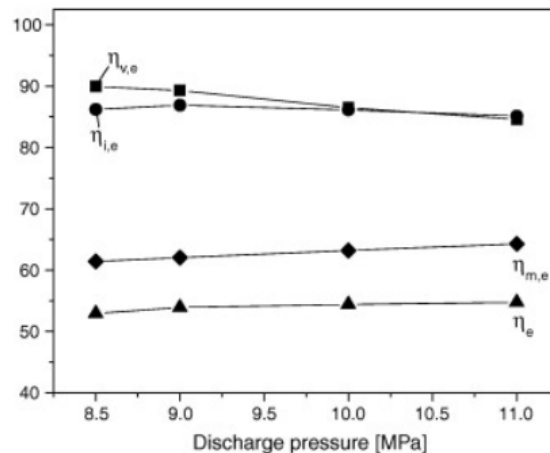


Figure 14. Scroll expander efficiencies for different discharge pressures [21]

In paper [22], the efficiency of a scroll expander used for regaining the energy of the exhausted high-pressure air from a PEM fuel cell has been investigated. Not only was energy conservation equation involved in the numerical analysis, but the radial leakage model also has been expressed according to Liansheng model (1998). The definitions and the equations of both radial and flank leakages are determined. Additionally, the main performance parameters, which are the theoretical expansion ratio ( $\rho$ ), the delivery ( $Q$ ), the indicated work ( $W_i$ ), the indicated isentropic efficiency ( $\eta_{ie}$ ) and the isentropic efficiency ( $\eta_e$ ), were calculated. The geometry of the scroll expander was constructed in line with a prototype expander designed and invented by National Engineer Research Center (NERC) for Fluid Machinery & Compressors at Xi'an Jiaotong University. The suction pressure fluctuated from 1.5 bar to 4 bar, when the rotating speeds ranged from 900 to almost 2800 rpm. Changing the suction pressure and the rotational speed

during the simulation, variations in expansion ratio and isentropic efficiency took place in accordance with Figure 15 and Figure 16.

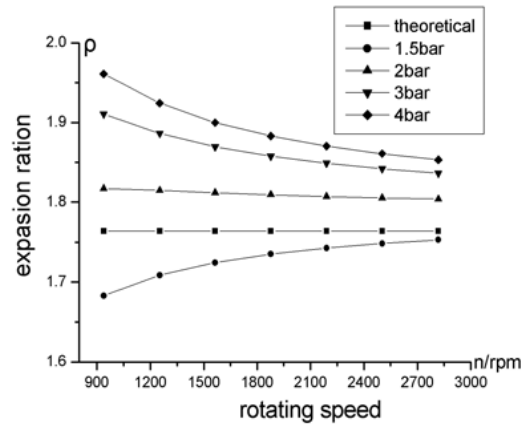


Figure 15. Fluctuation of expansion ratio due to the change in rotating speed [22]

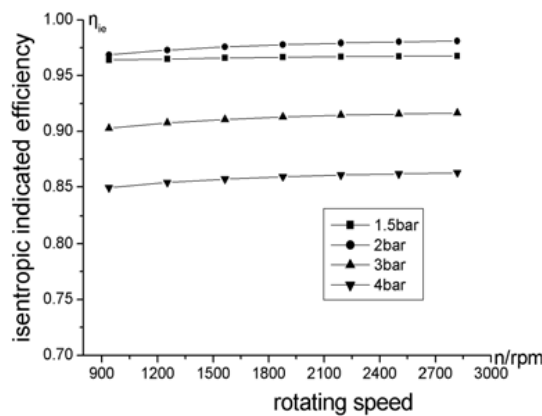
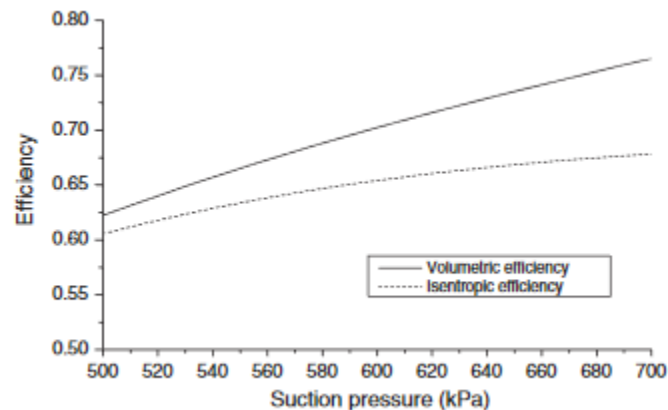


Figure 16. Fluctuation of isentropic indicated efficiency due to the change in rotating speed [22]

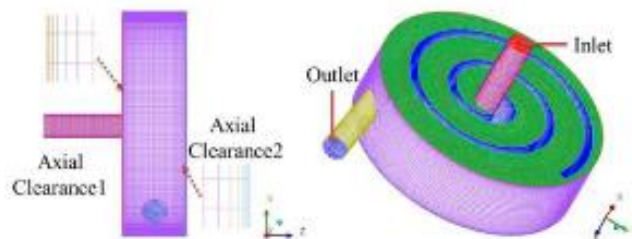
In [23], the theoretical study of a scroll expander-generator for small scale Organic Rankine Cycle with R123 as the working fluid was carried out. To achieve this, several models were introduced to calculate the thermodynamic, mechanical and load resistance. The geometric variables were not modified in the simulation. The formula used for the energy conservation of a specific control volume is described in [24]. Moreover, leakage and heat transfer affected the whole procedure and the scroll expander efficiency. The definitions of leakage areas were taken from [25], as well as the throttle nozzle model followed the principles from [24]. The suction and discharge process were analyzed using equations from [25], while the heat transfer model was presented in [26]. To construct the mechanical model, the vapour force, which increases the friction loss of the bearings and creates a rotary moment to move the orbiting scroll, was

estimated by the equations from [25]. During the simulation, the rotating speed varied from 1266.6 to 2103 rpm. The results of the simulation indicate that the stable rotating speed, volumetric and isentropic efficiency change with the variation of suction pressure, discharge pressure and generated current. As for the stable rotating speed and volumetric efficiency, a rise in suction pressure could cause their increase. However, if the discharge pressure or generated current increase, it can be observed a decrease in the stable rotating speed and the volumetric efficiency. The suction pressure fluctuated between 5 and 7 bar. The increase of suction pressure leads to the maximization of isentropic efficiency, from 0.61 to 0.69, as shown in Figure 17.



**Figure 17.** The variation of isentropic and volumetric efficiencies with the concurrent increase of the suction pressure [23]

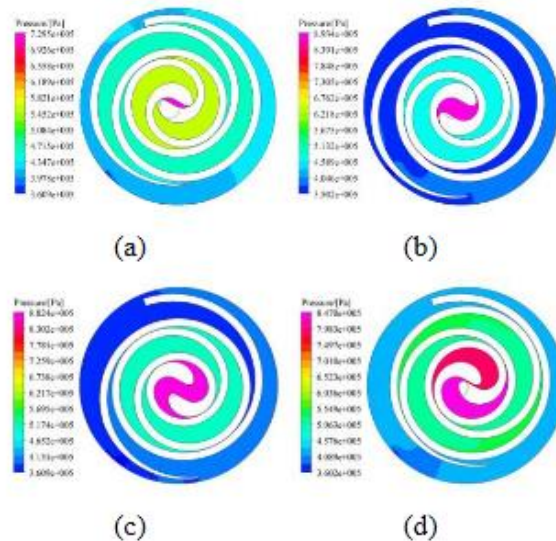
Three-dimensional numerical simulations of a scroll expander integrated in an ORC were executed with the dynamic mesh technology in [27]. The refrigerant used for this project was R245fa. The unsteady flows and thermodynamic efficiencies were performed in this study. Firstly, the grid model of the scroll expander was made in accordance with Figure 18.



**Figure 18.** Computational unstructured mesh of the scroll expander [27]

The k-ε turbulent model with renormalization group was adopted for the construction of flow model. As for the simulation initial parameters, the inlet pressure and temperature were

adjusted to 0.9 MPa and 405 K, respectively. The discharge pressure was considered equal to 0.3 MPa. In this paper, the numerical analysis was conducted for two divergent rotating speed values, 1000 and 1500 rpm. However, the unsteady flows were examined only for the case of 1000 rpm. Pressure, velocity vector and temperature distributions are presented and illustrated in report [27]. Therefore, the following figure, Figure 19, demonstrates the pressure variation on a cross-section area perpendicular to z-axis.



**Figure 19. Pressure distribution in the working chambers on a cross-section area perpendicular to z-axis [27]**

To investigate the efficiency of a small- scale ORC, S. Clemente et al. [28] merged the code of a one-dimensional model of a scroll expander with a thermodynamic model of a whole ORC system. By changing the geometric parameters of scroll devices and the working fluid, the performance of both scroll compressor and expander could be estimated by the detailed model of scroll machines. A deterministic model of scroll expander was introduced to calculate its geometry. This model was based, among other studies referred on [28], on Chen's deterministic model [26]. The R245fa was selected as the working fluid of ORC. To predict the scroll expander performance, the rotational speed was regulated to 3000 rpm and the superheating temperature (inlet expander temperature) could be 130 °C, 140 °C or 150 °C. The pressure ratio in this numerical simulation varied between 3 and 7. Consequently, an isentropic efficiency equal to 65% was achieved. Following the same methodology, the code was modified and executed for a new scroll geometry in order to increase the scroll expander performance. To attain this, the length of the wraps was increased from 2.75 to 4.75 revolutions, and as a result, a larger build-in expander ratio became feasible. The main coding parameters were remained stable. In this case, the pressure ratio could take a value from 4 to 9, when the isentropic efficiency of the scroll expander reached the 70%. In the following figures, the quantification of

each type of losses for both short and long scroll design are presented. As illustrated in Figure 20 and Figure 21, the optimum expansion ratio is displaced from 3.5 to 5.5.

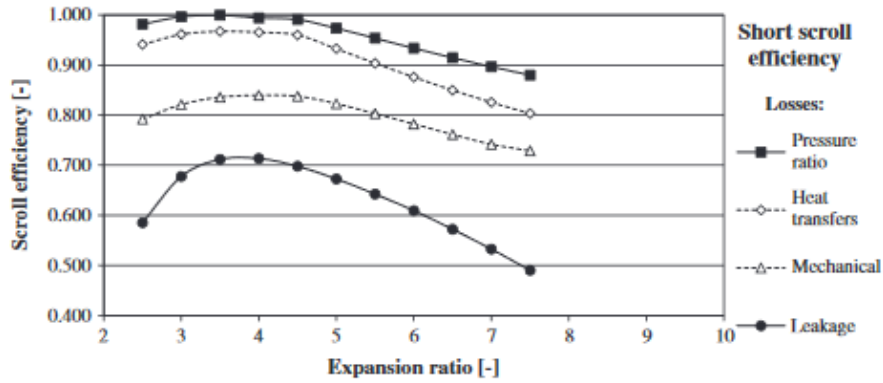


Figure 20.Scroll efficiencies as a function of expansion ratio for the short scroll expander [28]

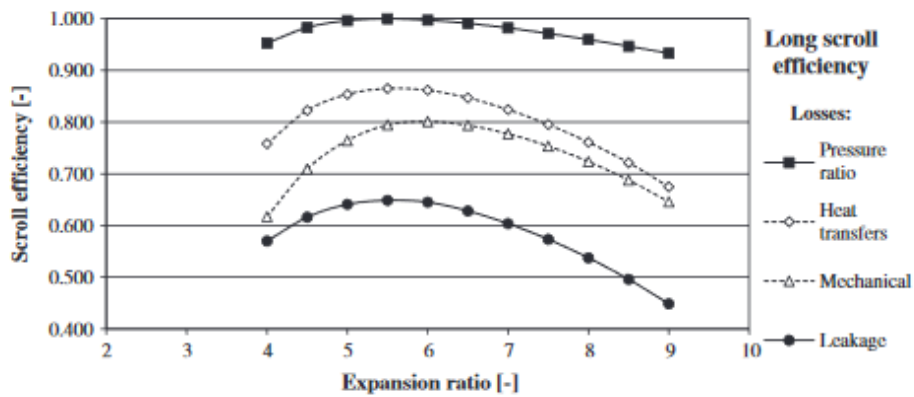
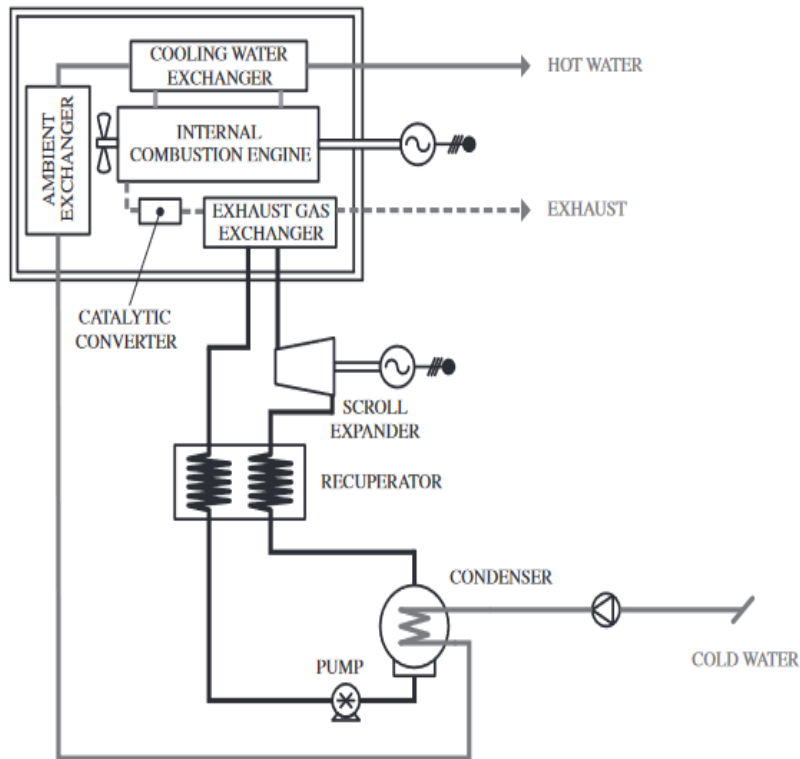


Figure 21.Scroll efficiencies as a function of expansion ratio for the long scroll expander [28]

In the second part of Clemente’s study, several applications were simulated based on a cycle parameter analysis. However, in this project, only the case of heat recovery from an internal combustion engine is presented. The configuration of this implementation can be shown in Figure 22.



**Figure 22. Micro-CHP configuration [28]**

This engine can be applied for residential and commercial buildings, in which the recovered heat is exploited in order to make domestic hot water. It was assumed that the expander's suction temperature is 150 °C and the expander's inlet pressure was equal to 12.59bar. The circulated refrigerant was R245fa. As for the isentropic efficiency of the expander, it was adjusted to 67.3%, when the expansion ratio was 5.

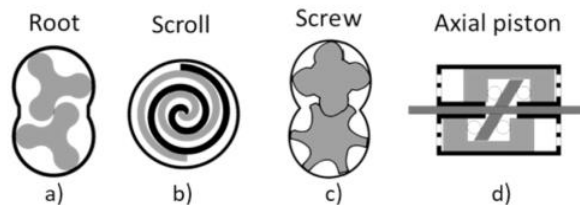
All the previous studies are concentrated on a brief table (Table 2). This table consists of the inlet temperatures (°C), suction pressures (bar), pressure ratios, types of expanders, working fluids, isentropic efficiencies (%) and rotational speeds (rpm) which characterize the expanders included in the referred theoretical investigations.

**Table 2. Non-exhaustive list of theoretical studies on expanders**

<i>Type of study</i>	<i>Inlet temperature (°C)</i>	<i>Suction Pressure (bar)</i>	<i>Pressure Ratio</i>	<i>Type of expander</i>	<i>Working fluid</i>	<i>Isentropic efficiency (%)</i>	<i>RPM</i>	<i>Reference</i>
CFD	132	11	-	Scroll	R123	40.5, 41.7, 41.8	2000	P. Song et al. (2015) [19], M. Wei et al. [20]
Theoretical	35	35	2.86	Scroll	CO <sub>2</sub>	86.12	2000	Kim et al. (2008) [21]
Theoretical	-	1.5, 2, 3, 4	1.67-1.96	Scroll	Air	85-97	900-2800	Gao, Li, Zhao, Shu (2004) [22]
Theoretical	-	5-7	-	Scroll	R123	61-69	1266.6-2103	L. Guangbin, Z. Yuanyang, L. Yunxia, and L. Liansheng (2011) [23]
CFD	132	9	-	Scroll	R245fa	-	1000, 1500	Song, Wei, Shi, Ma (2013) [27]
Theoretical	130, 140, 150	-	3-7	Scroll	R245fa	65	3000	S. Clemente et al. (2012) [28]
Theoretical	130, 140, 150	-	4-9	Scroll	R245fa	70	3000	S. Clemente et al. (2012) [28]
Theoretical	150	12.59	5	Scroll	R245fa	67.3	3000	S. Clemente et al. (2012) [28]

### 1.3.2 Experimental studies

In [29], the operation of a scroll, screw, root and piston expanders integrated into two different small-scale ORC configurations using R245fa was tested. Although the nominal power of these four types of expander was different, to determine their performance in relation to filling factors and isentropic efficiencies, this test concentrated on expanders' behavior in divergent operating conditions, including the nominal power. Moreover, the experimental configuration consisted of a brazed evaporator and recuperator, shell and tube water-cooled condenser, gear pump and a receiver. The highest isentropic efficiency was performed by the scroll expander (76%), while the screw and the piston demonstrated efficiency 53% and the roots a 47% isentropic efficiency. Additional results of this study are presented in Table 2.



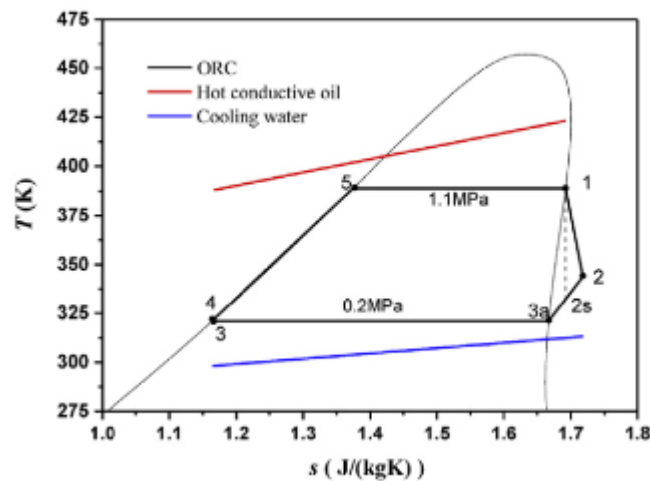
**Figure 23.**Types of volumetric expanders [29]

Additionally, several experiments were conducted by Lemort et al. [30] to examine a template of an open-drive oil-free scroll expander used for an ORC. The working fluid of this application was HCFC-123. The efficiency of the scroll expander was determined due to the calculation of specific parameters, such as mass flow rate, discharge temperature, ambient losses and internal leakages. This experiment was conducted by changing the mass flow rate (from 45.13g/s to 86.25 gr/s), the supply temperature (from 101.7°C to 165.2°C), the exhaust pressure (from 1.38 to 2.66bar), the rotational speed (1771, 2296 and 2660rpm) and the torque. The isentropic efficiency of the scroll expander in this certain test-rig fluctuated between 42.4% and 68%. To validate the experimental expander model, the following method was applied. At a first stage, the basic variables of the semi-empirical simulation model of the scroll expander were calculated based on the experimental results. Then, this model, in which the estimated parameters were included, anticipated the outlet temperature, the shaft power and the mass flow rate. All kinds of losses could be evaluated by the validated expander model. Moreover, the validated model could assess to what extent the design of the expander affects its performance and how to modify its design in order to improve the expander efficiency. This examination identified that the main reason why the expander performance was decreased, were the mechanical leakages and the supply pressure drop. Internal leakages also influenced the expander efficiency, but to a smaller degree.

Miao et al. [31] examined, an ORC system absorbing heat from a lubricant oil circuit. The test rig included the following circuits: the refrigerant R123, the cooling water, the conductive oil and the lubricant oil circuits. Figure 24 illustrates the thermodynamic changes occurred in the ORC working fluid, the cooling water and the fluid of heat source (conductive oil). In addition, the



main operating parameters in this experimental investigation were the temperature and the mass flow rate of cooling water and conductive oil, the air temperature, the shaft torque or rotational speed and R123 pumping frequency. These conditions influenced the application performance. The optimization of the total efficiency was achieved by decreasing the backpressure of the expander, rising the build-in expander's volume ratio and increasing the heat transfer happened in the evaporation stage. To analyze the scroll expander model, Lemort's [30] semi-empirical model was introduced. The measured thermal efficiency and shaft power were 5.64% and 2.65 kW, but in the optimum cycle they could reach 6.05% and 10.7 kW respectively. A comparison between mathematical calculations and experimental results was carried out. The most significant deviation between the experimental measurements and calculations was 5.5%.



**Figure 24.**T-s diagram of Miao et al. ORC configuration [31]

The developed diagrams of this study display the relevance of expander rotational speed, shaft power and system thermal efficiency to R123 mass flow rate for divergent variations on operating conditions. Thus, Figure 25 presents the influence of the ambient temperature on the produced shaft power for a range of refrigerant mass flow rate values. The scroll expander produced more electricity for lower air temperatures. The maximum expander shaft power, equaled 2630W, was performed for mass flow rate 700 kg/h and air temperature equal to -5°C.

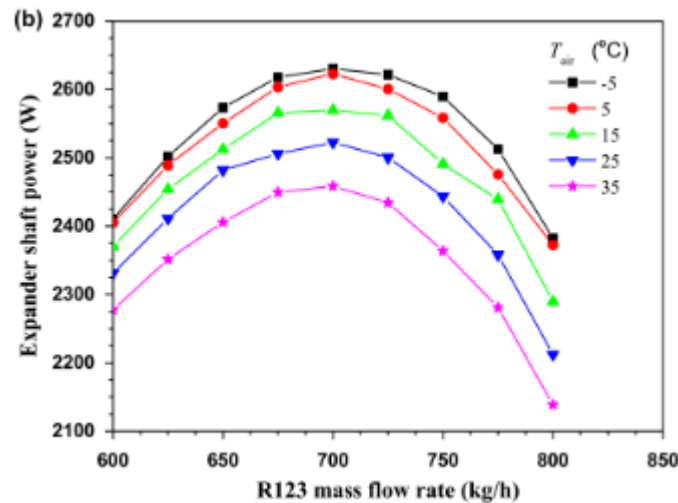


Figure 25. Expander shaft power as a function of air temperature and R123 mass flow rate [31]

Ziviani et al. [32] investigated an open-drive oil-free scroll expander characterized by nominal capacity of 5kW through experiments. The build-in volume ratio of this expander was equal to 3.5 and the scroll machine operated for a range of rotational speeds, from 800 rpm to 3000rpm. The scroll expander was used for an ORC application that was working with R245fa. The inlet temperature of the heat source fluid could be either 85°C or 110°C. In addition, the development of the expander model was based on Lemort's [30] semi-empirical model. The isentropic efficiency of the expander became maximum and equal to 58% for 1600rpm, but the maximum output power, 3.75kW, was achieved for 2500rpm.

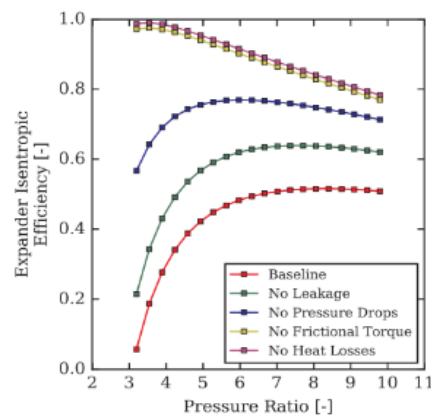


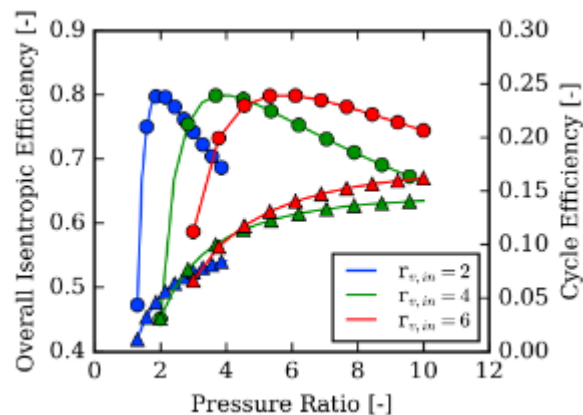
Figure 26. The effects of internal losses on expander isentropic efficiency for rotational speeds of 3000rpm [32]

The isentropic efficiency of the expander as a function of the pressure ratio is illustrated in Figure 26. It can be observed that the isentropic efficiency presented a significant increase when the

pressure drops, leakages and frictional torque were eliminated. Moreover, the heat transfer off curve performed a lower deviation from the no frictional torque curve. As a result, the impact of heat losses on expander's isentropic efficiency could be neglected.

Z. Liu et al. [33] developed a CFD model to simulate the scroll expander with the FEM method, and then, they conducted an experimental validation. Using the surface pressure and the temperature of the scroll expander components as boundary conditions, this CFD model evaluated the thermal loads and pressure. They also calculated the deformation happened due to the loads which stressed the expander. The scroll expander of this certain experiment was integrated in an ORC waste heat recovery system utilizing R123 as the working fluid. Both the numerical analysis and the experiments were carried out under four combinations of rotating speeds, discharge temperatures, inlet pressures and temperatures.

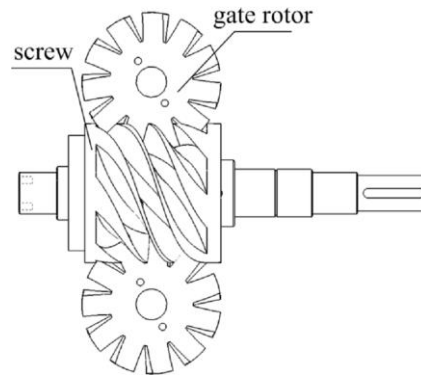
D. Ziviani et al. [34] tested a single- screw expander integrated in an ORC with liquid flooded expansion using R245fa as circulating fluid. To determine the heat and friction losses, the build-in volume ratio and the operation with lubricant oil, the experiments and the simulations were based on a semi-empirical model of the expander. Apropos of the working fluid, the refrigerants R245fa and R1233zd(E) were both selected and compared in order to examine a potential replacement of R245fa with R1233zd(E), and consequently, investigate the advantages of flooded expansion in a screw expander. In the following figure (Figure 27), it can be shown the impact of the expander internal volume ratio on the expander isentropic performance (circle markers) and cycle performance (triangle markers) as a function of pressure ratio. It is obvious that the maximum isentropic efficiency could be 80% for a specific value of the pressure ratio depending on the build-in volume ratio.



**Figure 27. Total isentropic efficiency (circle markers) and cycle efficiency (triangle markers) for three expander build-in volume ratios and different pressure ratios [34]**

Lei et al. [9] tested a single screw expander employed for an ORC system. The working fluid of this application was the R123. The aim of this experimental investigation was mainly to increase the screw expander efficiency in a wide range of expander conditions. The influence of supply

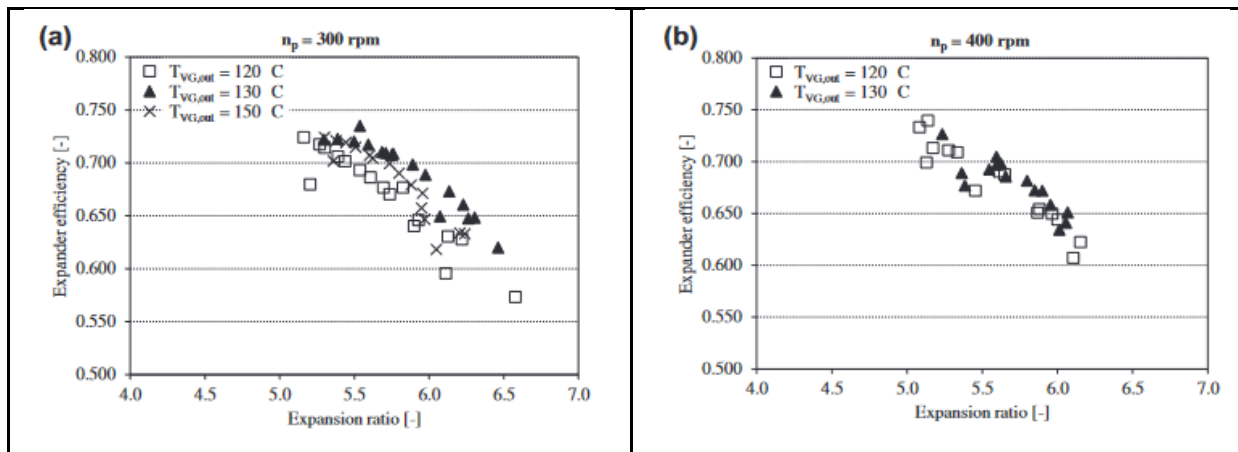
pressure and the expansion ratio was investigated for divergent rotational speeds. Based on the concept of increasing the internal volume ratio suitably and modifying the screw expander from single to double- stage by exploiting the screw grooves outlet velocity, they designed and constructed a new prototype (Figure 28). The maximum isentropic efficiency, shaft power and expansion ratio presented by experiments was 56%, 8.35 kW and 8.5, respectively. It was also ascertained that the under-expansion losses were eradicated.



**Figure 28. Structure of the Lei's single screw expander prototype [9]**

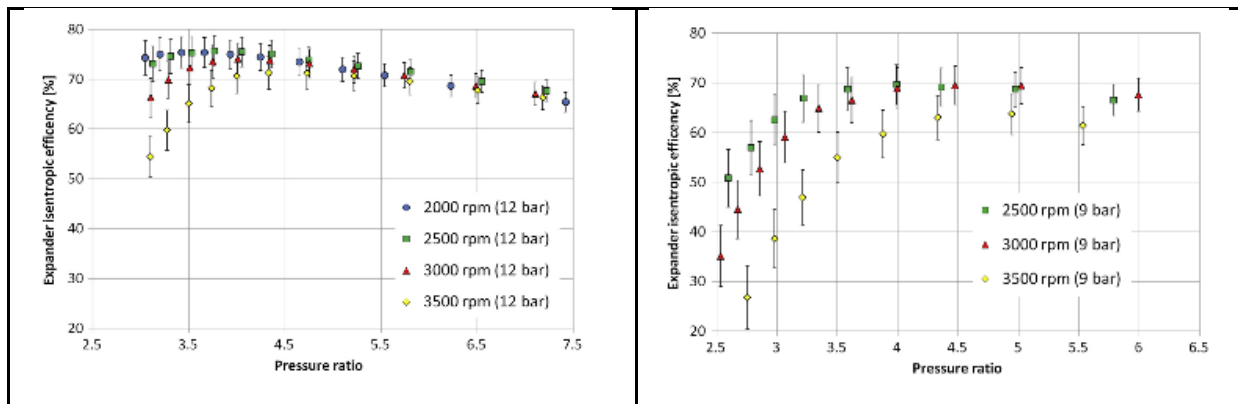
F. Ayachi et al. [35] tested a hermetic scroll expander applied for a small- scale ORC suitable for low grade heat recovery. Using the semi-empirical expander model proposed by Lemort [30] and R-245fa as refrigerant, they investigated the expander prototype changing the supply and discharge operating conditions. Supply temperature fluctuated from 105 °C to 135 °C, while the pressure ranged between 10.3 bar to 22.5 bar. The experiments showed that the hermetic scroll expander achieved high efficiencies when high supply conditions were imposed. For supply pressure equal to 20 bar, the net performance of the combined expander- generator took its maximum value (70%). In addition, the maximum power was measured equal to 2.9 kW with temperature, inlet pressure and pressure ratio at 135 °C, 22.5 bar and 3.8, respectively.

R. Bracco et al. [36] simulated and investigated a hermetic expander integrated in a domestic-scale ORC. For this study, a commercial HVAC compressor was converted into a scroll expander with a potential power output of 1.5 kW. Refrigerant R245fa was selected as the working fluid of ORC. Based on results taken from several studies, numerical simulations were carried out. The experimental calibration of the expander model revealed sufficient accuracy in the preliminary variables predicted by the relevant literature review. Firstly, several tests were conducted in order to examine the deviations between the calculated and the measured efficiencies and acquire the data for the model calibration in constant operating conditions. To optimize the system performance, determine the system potentialities and define the more effective operating conditions, more experiments were carried out. The expander shaft speed ranged from 3000 rpm to 4500 rpm. The following figure (Figure 29) presents the isentropic expander efficiency as a function of the expansion ratio for pump rotational speeds 300 rpm and 400 rpm and vapor temperatures 120 °C, 130 °C and 150°C.



**Figure 29. Expander isentropic efficiency for divergent expansion ratios, vapor temperatures and pump rotational speed equal to (a) 300 rpm and (b) 400 rpm [36]**

A scroll expander with nominal power production equal to 1.8 kW was used for an ORC tested by S. Declaye et al. [37]. As for the expander construction, an air compressor was converted appropriately in order to operate as an expander. R245fa was chosen as the working fluid of this experimental investigation. The main goal of the experiments was to create the expander performance map in different operating conditions. Therefore, the suction pressure fluctuated from 9 to 12 bar, the discharge from 1.5 to 4 bar and the rotating speed varied from 2000 to 3500 rpm. For these testing conditions, 74 values of expander isentropic efficiency were calculated and displayed in the following figure (Figure 30). As it can be observed, the maximum isentropic efficiency is 75.7%.



**Figure 30. Isentropic efficiency of expander as a function of the pressure ratio for a range of rotational speeds and inlet pressures [37]**

The following table includes the main parameters and results of the aforementioned investigations analyzed in this section as well as the deduced data from other relevant experimental studies.

**Table 3. Non-exhaustive list of experimental studies on expanders**

<i>Inlet temperature (°C)</i>	<i>Suction Pressure (bar)</i>	<i>Pressure Ratio</i>	<i>Type of expander</i>	<i>Working fluid</i>	<i>Isentropic efficiency (%)</i>	<i>RPM</i>	<i>Reference</i>
122-133	5.7-14.7	1.4-7.4	Scroll	R245fa	76	1137-7920	O. Dumont et al. (2018) [29]
75-130	6.4-12	1.9-4.17	Screw	R245fa	53	500-12450	O. Dumont et al. (2018) [29]
70-124.4	2.7-10	1.14-4.47	Roots	R245fa	47	1000-11000	O. Dumont et al. (2018) [29]
118-153	17.7-30.7	6.2-10.6	Piston	R245fa	53	1000-4000	O. Dumont et al. (2018) [29]
101.7-165.2	5.45-11.12	2.7-5.4	Scroll	HCFC-123	42.4-68	1771-2660	V. Lemort et al. (2009) [30]
142.9	7.82	3.11-5.22	Scroll	R123	70	2569	Z. Miao et al. (2017) [31]
110	13.8	5.95	Scroll	R245fa	58	1600	D. Ziviani et al. (2018) [32]
110-176.07	8.35-10	2.94-3.87	Scroll	R123	-	1986-2010	Z. Liu et al. (2018) [33]
120	-	9.34	Screw	R245fa	80	-	D. Ziviani et al. (2017) [34]
120-130	11.5	8.5	Screw	R123	73	3000	B. Lei et al. (2016) [9]
105-135	10.3-22.5	2-3.8	Scroll	R245fa	70	3000	F. Ayachi et al (2016) [35]
100	3.3-4.7	2.35-3.35	Screw	R123	87.5	1500	Tang et al. (2015) [38]
65.85	19.28	2.5-3.0	Scroll	R134a	40-80	2000	Hoque (2011) [39]
-	4.5-4.8	4.4-4.8	Scroll	R123	36.4	1200-2066	Liu et al. (2013) [40]

120-150	5	4.6	Scroll	HFE-7100	75	-	M. Jradi et al. (2014) [41]
70	-	2.4-4.0	Scroll	R134a	63-65	2400-3600	Zanelli and Favrat (1994) [42]
120-150	-	1.6-4.8	Hermetic Scroll	R134a, R123	50-68	-	M. Kane et al. (2003) [43]
90-130	13-17.5	5-6.5	Scroll	R245fa	57-75	3000, 4500	R. Bracco et al. (2013) [36]
136	-	-	Scroll	R113	63	1500-5000	Saitoh, Yamada, Wakashima (2007) [44]
77.3	-	-	Scroll	R134a	10-65	250-4000	Manolakos et al. (2007) [45]
97.5	12	3-8	Scroll	R245fa	55-75.7	2000-3500	S. Declaye et al. (2013) [37]
68-140	-	-	Scroll	R123	65	300-1300	N. Zhou et al. (2013) [46]

## 1.4 Thesis scope

---

Given the literature review above, it is found a gap of knowledge in the studies of two-phase flows in expanders and specifically for scroll expanders. Therefore, this study aims to investigate the performance of conventional scroll expanders in two phase region, by modifying an existing deterministic model of expander and evaluate the effect of specific design variables and implemented theoretical sub-models in the overall expander's performance.

More specifically, this study aims to answer in the following questions:

- How can a deterministic model for a scroll compressor be modified to simulate the performance in expander mode?
- How important is the influence of the pressure ratio, the rotational speed and the inlet stream's quality in the two-phase expander's performance?
- Which is the difference in performance loss by the introduction of two-phase flows in comparison to conventional single-phase flows?
- How much do the geometrical aspects of the scrolls impact the overall expander's efficiency?



## 2. Deterministic model

### 2.1 Introduction into expander modelling

---

Modelling can be an effective tool for the design procedure of scroll expanders, since it can improve their performance. Different types of modelling approaches exist. Deterministic models are based on the application of physical equations of mass and energy balance to predict the behavior of the expander and take into account the detailed thermodynamic processes occurring during the expansion of the working fluid. Because of this, their scope is more general, while they are more complicated and more computationally intensive. On the other hand, empirical models typically are based on constants without a physical meaning and are calibrated based on experimental data. As a result, their scope is usually limited, but they are simpler (usually in the form of polynomial regression formulas) and less computationally intensive. Finally, semi-empirical models fall combine features of both deterministic and empirical models.

The empirical and semi-empirical models are often developed to describe mostly the thermodynamic phenomena occurred during the function of scroll expanders. The direct correlation between performance parameters and operating parameters is integrated to empirical analysis. The critical parameters are extracted from experimental results. However, the complicated geometrical features of scroll expanders and their working fundamentals are eliminated when empirical modelling is applied. The semi-empirical models examined focusing on thermodynamic equations inferred from mass, energy and momentum conservations. The validation of empirical and semi-empirical models is restricted to a specific range.

A semi-empirical model of an open-drive oil-free scroll expander integrated into an ORC is presented in [30]. The refrigerant circulated in the ORC is HCFC-123. As illustrated in Figure 31, the expansion process can be separated into two main stages: isentropic and isochoric expansion. Eight variables of the scroll expander semi-empirical model can be calculated, using the expander performance measurements. In addition, supply pressure drops, internal leakages and internal expansions take place in this modelling. There are also estimated the mass flow rate, the distributed shaft power and the discharge temperature.

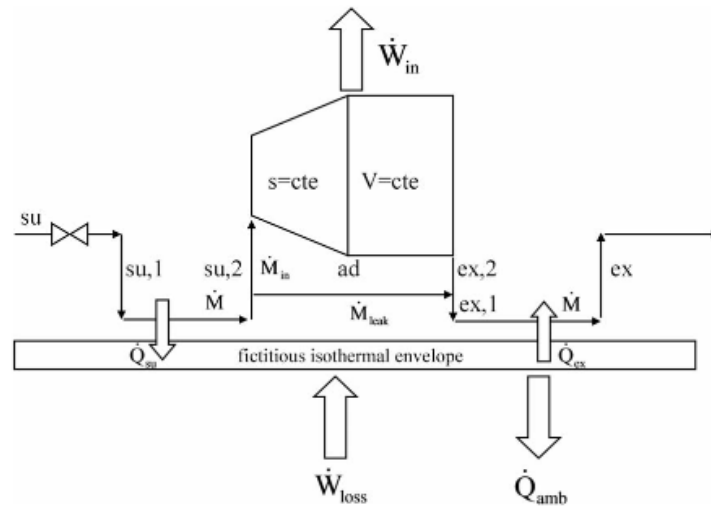


Figure 31. Lemort's semi-empirical model of a scroll expander [30]

### 2.1.1 Deterministic model of scroll compressor/expander

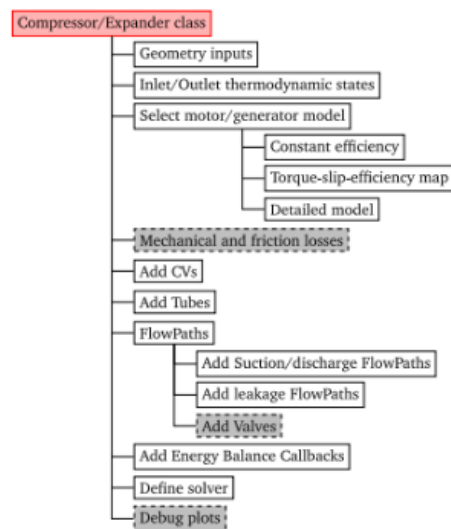
The present work is based on the deterministic scroll compressor model developed by Ian Bell [47]. The model includes two main sub-models, a geometric and a thermodynamic model. More specifically, the scroll compressor geometry, the definitions of the control volumes, leakage areas and forces are computed in the geometric model. On the other hand, the thermodynamic model simulates the expansion process of the working fluid during the operation of the machine aiming at the prediction of its performance. At the beginning of the execution process, the geometric model produces the geometric variables which, in turn, are used by the other sub-models. At every step of the overall model, the geometric parameters are updated. Therefore, the divergent sub-models are executed in an effort to find a solution for all the combinations of geometric inputs and system state points.

### 2.1.2 Introducing PDSim

The model developed by Bell is implemented in PDSim software. PDSim is developed mainly in the Python programming language and it covers both 2.x and 3.x versions. The reasons why Python was selected for the PDSim code are its free availability, the ability to be attuned to any type of device and software, the diverse packages accessible and the dynamic community [48]. To attain high computational performance, PDSim combines the high-level characteristics of Python with the low-level development through Cython. Python can be defined as an object-oriented programming language. That leads to a much simpler model forming and helps the extension of the current libraries. Moreover, GUI (Graphical User Interface) is included in PDSim due to wxPython package.

Each category of positive displacement engine constitutes a class in PDSim. These classes can be used to create a certain compressor or expander model. In Figure 32, the general construction of a class of a simulation model in PDSim is represented. Three main folders form the PDSim source code: PDSim, GUI and examples. PDSim folder consists of the following sub-folders: core, flow, misc, plot, recip, rolling and scroll. All core parts of PDSim are involved in core. The flow sub-folder contains all the flow models and flow path methods, while miscellaneous items are included in misc sub-folder. Reciprocating machine, rolling piston machine and scroll machine core classes located in recip, rolling and scroll folder respectively.

Graphical user interface is available through files integrated into GUI sub-folder. Finally, there are some examples of expander and compressor models in examples folder. [49]



**Figure 32.A common class in PDSim for a compressor or an expander model**

[49]

The usual process of description for a model of positive displacement machine is displayed in Figure 33 in pseudocode. The core class of a specific machine structure is located at the main PDSimCore class (PDSim/core/core.py).

```

# Instantiate the model
comp = CompressorClass()
# Define the inputs
# For example: comp.Vdoad = 0.5e-5)
# Define boundary conditions
Ref='Air'
inletState = State(Ref, T=298.15, P=101.325)
outletState = State(Ref, P=2*inletState.P, S=inletState.S)
mdot_guess = inletState.rho*comp.Vdisp*comp.omega/(2*pi)
# Add control volumes(ol)
comp.add_CV(ControlVolume(key, inletState, VdVfcn, becomer))
# Add inlet tube
comp.add_tube(Tube(
    key1='inlet.1', key2='inlet.2', L, D,
    mdot=mdot_guess, State1=inletState.copy(),
    fixed=1, TubeFcn=comp.TubeCode
))
# Add outlet tube
comp.add_tube(Tube(
    key1='outlet.1', key2='outlet.2', L, D,
    mdot=mdot_guess, State2=outletState.copy(),
    fixed=2, TubeFcn=comp.TubeCode
))
# Add flow paths to link flow nodes)
comp.add_flow(FlowPath(key1.key2,MdotFcn))
comp.add_flow(FlowPath(key1,key2,MdotFcn))
# Connect all the callbacks
comp.connect_callbacks(
    endcyle_callback=comp.endcyle_callback,
    heat_transfer_callback=comp.heat_transfer_callback,
    lump_energy_callback=comp.lump_energy_callback
)
# Run the solver
comp.solve(
    key_inlet='inlet.1',
    key_outlet='outlet.2',
    solver_method='RK45',
    OneCycle = False,
    UseRK = False
)

```

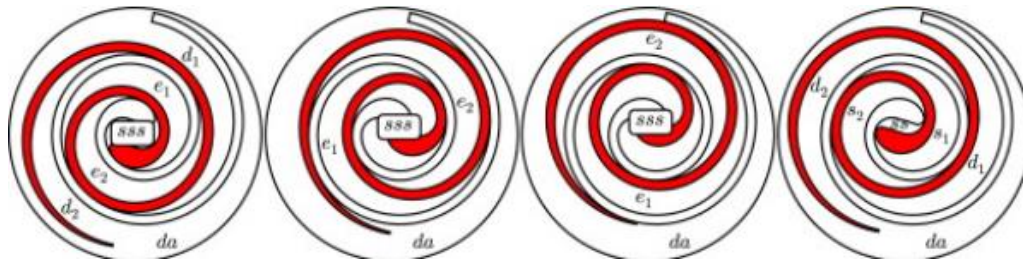
**Figure 33.** Pseudo-code of a compressor in Python-like form [48]

The PDSimCore class minimizes the computational work required to execute a model program due to some integrated methods. These techniques are: `add_CV()` for control volumes, `add_flow()` for flow paths (inlet and outlet flows, suction and discharge flows, leakage flows), `add_tube()` for both inlet and outlet tubes, key of the machine and possible injection lines and `add_valves()` for valves. [49]

### 2.1.3 Adaptation of PDSim models

In the original version of PDSim there were some gaps and simplifications with respect to the modelling of a scroll expander and in particular in two-phase expansion. Therefore, in the following subsections, the modifications and development of additional scripts on the existing classes of PDSim will be to cover the “gaps” and develop a detailed model for the respective scroll expander of the test rig.

Primarily, the way that the control volumes (CVs) are defined is altered in order for the model to work as a scroll expander instead of scroll compressor. In other words, in the split and discharge angles, the created pockets differ depending on the type of the scroll machine, namely compressor or expander. The following figure, Figure 34, illustrates the expander pockets formed over the course of one rotation. More specifically, the name of the suction chamber is *sss*, a pocket which, during the rotation, is divided into *ss*,  $s_1$  and  $s_2$  in the split angle due to the contact of the scroll wraps. These certain three control volumes are not fully separated, but they communicate through some small orifices. That leads to the pressure difference between *ss* and  $s_1$ ,  $s_2$ . In the next stage, both  $s_1$  and  $s_2$  are converted into  $e_1$  and  $e_2$  and then into  $d_1$  and  $d_2$  correspondingly. For larger volume ratios, more expansion control volumes are introduced. All these modifications are carried out in the `expander.py` situated in the subfolder PDSim/scroll.



**Figure 34. Scroll expander's generated chambers during one rotation [50]**

In addition, the functions that use the function `Flowpath`, which is calculated in the file `PDSim/flow/flow.pyx` are adjusted to the expander mode. In particular, the functions `S_to_SS` and `DA_to_D`, which are calculated in `expander.py`, use the `Flowpath` function as an object in an effort to determine the mass flow rate of the refrigerant that circulates in suction and discharge chambers respectively. By calculating the `Flowpath.A`, which is an attribute of `Flowpath` and describes the area of a specific flow path, as well as by using the attributes `Flowpath.State_up` and `Flowpath.State_down` that refer to the high- and low- pressure states in the isentropic nozzle correspondingly, the `IsentropicNozzle` function (defined in `PDSim.flow.flow_models.pyx`) is applied for the mass flow rate determination depending on the flow. The exact operation of this function is described in the following subsection, in flow models. Undeniably, so as to find the flow mass rate that enters from the inlet port to the suction chamber, the same process is necessary to be done. On the other hand, the mass flow rate delivered from the discharge pocket to the outlet port is considered fixed.

It is also essential that the definitions of all the efficiencies as well as of the mechanical losses are modified in order to describe the expander operation. These interferences take place in `expander.py` file. Their accurate definitions are given in the next paragraphs.

Apart from the alterations affiliated with the expander operation, several changes in terms of the conversion of single-phase to two-phase flow are conducted. First of all, new heat transfer and pressure drop models for the inlet and outlet tubes are introduced in the function `IsothermalWallTube` (`PDSim/flow/flow_models.pyx`) so as to describe these phenomena in wet expansion. The relative equations are given in the flow models section. Furthermore, the leakage model is changed in an effort to operate for the two-phase flow. These are defined in function `FrictionConnectedIsentropicNozzle` in the folder `PDSim/flow/flow_models`.

Finally, in order for the above alterations to be attuned to the existed code, several computing changes are carried out in other files, such as in `PDSim/scroll/core.py`, `PDSim/core/core.py` and `PDSim/core/containers.pyx`.

## 2.2 Scroll geometry

### 2.2.1 Scope

As for the geometric model, the base circle and the involutes of the scroll compressor are defined. This geometry is relied on a specific form in which the involutes are unwrapped from a circle. In particular, the displacement volume  $V_{disp}$ , the volume ratio  $V_{ratio}$ , the thickness of the fixed scroll wrap, the orbiting radius and the angles  $\varphi_{i0}$ ,  $\varphi_{os}$  and  $\varphi_{is}$  are known and constitute the input variables of the geometric function defined in `scroll_geo.py`. By applying this function, all the geometric parameters, namely the base circle radius, the scroll height,  $\varphi_{ie}$ ,  $\varphi_{oe}$  and  $\varphi_{o0}$  can be specified. Having defined the basic geometric variables, all the formed control volumes during a whole rotation, namely the suction, compression and discharge chambers, and their corresponding derivatives are calculated in `symm_scroll_geo.pyx`. Especially for the discharge chamber, two models are proposed, the two-arc and the arc-line-arc geometrical types, which are fully analyzed in the two subsequent subsections. This is followed by describing all the flow paths that take place throughout the scroll operation. To be more precise, the equations that describe the radial and flank leakages as well as those connected with the suction and discharge areas and discharge port are given. Concluding the above, the main aim is to determine the volume of every chamber, their derivatives and the flow areas in every rotating angle ( $\theta$ ). The description of these operations is presented in section 2.1.3 in detail.

### 2.2.2 Two-Arc geometry

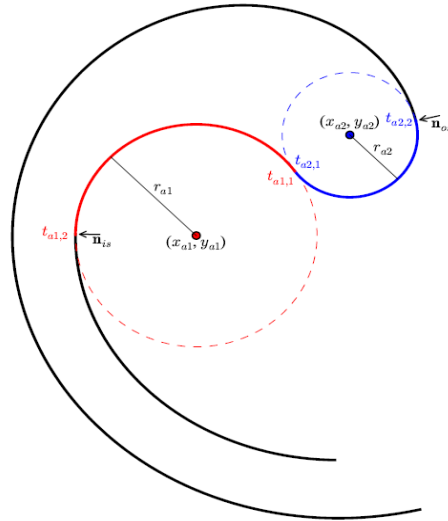
As for the two-arc geometry, the curves in this case can be determined by the Figure 35, in which the arc 1 is integrated with the inner involute, whereas the arc 2 is connected with the outer one. As depicted in this figure, the arcs and their respective involutes are tangent and coincident simultaneously. Taking this fact into consideration and analyzing their normal vectors, the coordinates of the center of each arc are easy to be prescribed. [47] In the next expressions,  $\varphi_{i_s}$  and  $\varphi_{o_s}$  are the starting angles of inlet and outlet involutes and constitute the key geometric parameters in the investigation described in section

$$x_{a1} = x_{fi_s} - \sin \varphi_{i_s} \cdot r_{a1} \quad 2.1$$

$$y_{a1} = y_{fi_s} + \cos \varphi_{i_s} \cdot r_{a1} \quad 2.2$$

$$x_{a2} = x_{fo_s} - \sin \varphi_{o_s} \cdot r_{a2} \quad 2.3$$

$$y_{a2} = y_{fo_s} + \cos \varphi_{o_s} \cdot r_{a2} \quad 2.4$$



**Figure 35.**The illustration of the two-arc geometry [47]

Consequently, the depicted geometrical parameters can be expressed by the following mathematical equation:

$$\sqrt{(x_{a1} - x_{a2})^2 + (y_{a1} - y_{a2})^2} = r_{a1} + r_{a2} \quad 2.5$$

In addition, this geometry respects the correlation  $r_{a1} \geq r_{a2} + r_o$ , where  $r_o$  constitutes the orbiting radius of the scroll machine, in order for the scroll involutes not to collide into each other. After defining all the above, the correlations that connect the radii of the two arcs with the  $\varphi_{i_s}$  and  $\varphi_{o_s}$  are given in [47]. The perfect matching of arcs 1 and 2 is achieved for the following equation:

$$\varphi_{i_s} = \varphi_{o_s} + \pi \quad 2.5$$

In this case the radius of the arc 1 is provided by:

$$r_{a1} = r_{a2} + r_o \quad 2.6$$

### 2.2.3 Arc-Line-Arc geometry

Firstly, according to [47], in order to specify the discharge geometry in an arc-line-arc scroll compressor (equivalent with the suction area in a respective scroll expander), the radii of the two arcs are needed to be estimated. In an effort to discourage the collision, the geometry should also respect the correlation  $r_{a1} \geq r_{a2} + r_o$ . As well for the Arc-Line-Arc geometry, the most suitable meshing profile is acquired based on the equations 2.5 and 2.6. The distance ( $d$ ) between the centers of the two arcs is given by the equation:

$$\sqrt{(x_{a2} - x_{a1})^2 + (y_{a2} - y_{a1})^2} = d \quad 2.7$$

In the subsequent figure, Figure 36, the set of the curves included in the Arc-Line-Arc geometry is presented.

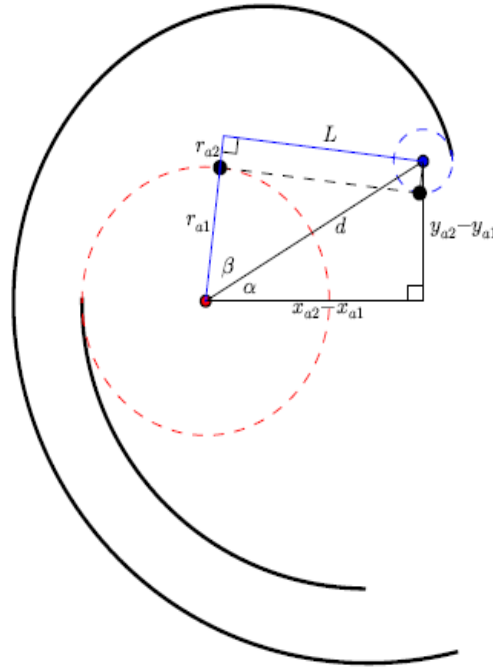


Figure 36. The geometric parameters of an Arc-Line-Arc machine [47]

## 2.3 Deterministic model description

### 2.3.1 Flow models

First of all, the divergent flow models contained in PDSim are used so as to define the mass flow rate in all paths. The inputs of flow models indulged in the deterministic model are the flow area and the pressure difference through a certain flow path. Moreover, a pressure model is adapted to the flow models' script in order to calculate any pressure drop that occurs in the inlet and outlet tubes. Apart from the pressure model, a heat transfer model is also included in flow models. This model determines the amount of heat transfer exchanged not only between the working fluid and the shell of the expander in both inlet and outlet tubes, but also between the working fluid and the shell of the expander in the CVs.

The refrigerant flows between two adjoining CVs or from one CV to a tube, and as a result, many flow paths are constructed throughout the rotation of the scroll expander. The formed flow paths can be separated into two categories. There are the primary flow paths affiliated with flows carried out between CVs and tubes openly associated and constitute extensive flow areas.



As for the other type, there are also, because of the existing small cavities, the leakage flow paths refer to non-openly associated CVs. Suitable flow models render the calculation of the mass flow rate for both types of flow paths feasible relied on their flow area and pressure difference.

### 2.3.1.1 Primary flow models

Initially, in terms of the type of primary flow, it can be assumed that flow is adiabatic and compressible since it can be simplified by a respective flow conducted in a convergent nozzle. Consequently, to evaluate the mass flow rate of the primary two-phase flow, the following equation is used [50]:

$$\dot{m} = X_d C_d A_{th} \sqrt{\frac{2 \int_{p_{down}}^{p_{up}} v_e dp}{v_{e,down}^2 - \sigma v_{e,up}^2}} \quad 2.9$$

Where:

- $X_d$  is the area correction factor (vena contracta coefficient). More specifically, due to the fact that the flow passes through orifices, a flow contraction slightly downstream of these orifices takes place, and as a result, the cross-section area and the mass flow rate become minimum and maximum respectively. It is assumed that  $X_d=1$ , but there is a need for an experimental verification.
- $C_d$  is the discharge coefficient ( $C_d=0.77$ ) presented by Morris (1991)
- $A_{th}$  is the throat area of the nozzle and is defined in every rotation angle of scroll expander
- $\sigma$  is the area ratio of downstream to upstream regions
- $v_e$  is the effective mixture specific volume

The effective mixture volume is calculated from the following equation for both downstream and upstream areas.

$$v_e = [x \cdot v_g + K_e \cdot (1 - x)v_l] \left[ x + \frac{(1 - x)}{K_e} \right] \quad 2.10$$

Where  $K_e$  constitutes the effective slip ratio and can be calculated as

$$K_e = \psi + \frac{(1 - \psi)^2}{K - \psi} \quad 2.11$$

Where  $K$  represents the entrainment slip ratio obtained from

$$K = \psi + (1 - \psi) \sqrt{\frac{1 + \psi \cdot \frac{(1-x) \cdot v_l}{x \cdot v_g}}{1 + \psi \cdot \frac{(1-x)}{x}}} \cdot \sqrt{\frac{v_g}{v_l}} \quad 2.12$$

Where  $\psi$  is the mass fraction of liquid which circulates through the gas phase, being at the same velocity with the gas. Should there is no entrainment,  $\psi$  is equal to zero.

### 2.3.1.2 Leakage flow models

As it has been mentioned, there are two genres of leakage flow paths, radial and flank. The leakage models are formed in the PDSim/flow/flow\_models.pyx file. The specific function in which all the below calculations take place is the FrictionCorrectedIsentropicNozzle.

#### ➤ Radial flow paths

Primarily, in the radial flow path, the flow circulates through a cylindrical section characterized by a height  $\delta_r$ , which constituted the gap between the top and the bottom layers. The radii of the inlet and outlet scroll wraps,  $r_1$  and  $r_2$  respectively can also be defined with their difference being equal to the wrap thickness.

The fluid is assumed as ideal and compressible, and hence, an isentropic compressible nozzle flow model is adapted. The flow passes from an upstream state characterized by higher pressure to a downstream state during the expansion procedure.

As a result, the mass flow rate is given by

$$\dot{m}_{nozzle} = A \cdot \sqrt{p_{up} \cdot \rho_{up}} \cdot \sqrt{\frac{2k}{k-1} \cdot \left( p_{ratio}^{\frac{2}{k}} - p_{ratio}^{\frac{k+1}{k}} \right)} \quad 2.13$$

The throat area for the radial leakages is calculated relied on the following correlation:

$$A = s_r \cdot \delta_r \quad 2.14$$

In the above equation,  $s_r$  depicts the arc length of the leakage path and it is equal to  $2\pi r_1$ .

Thus, the Reynolds number is determined by:

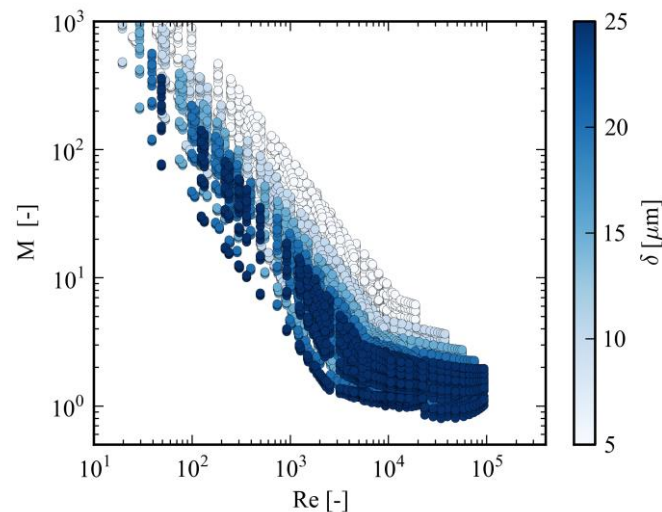
$$Re = \frac{\dot{m} \cdot d}{A \cdot \mu} \quad 2.15$$

Where  $d$  is the hydraulic diameter, standing at  $2\delta$ , whereas  $\mu$  is the viscosity of the upstream state.

However, the isentropic nozzle model does not include the frictions appeared due to the small orifices, and as a result, a correction term is required for the radial gaps. For this reason, a numerical process is introduced in an effort to predict the mass flow rate of the radial losses including the real fluid properties and a variable area. To achieve this, in [47], the frictional flow model is developed by conducting a numerical investigation for four refrigerants. In particular, the upstream pressure is changed with a restriction of a maximum value of the pressure ratio. In this stage, mass flow ratio is defined to describe the deviation of the mass flow rate of the isentropic nozzle and this of the real model.

$$M = \frac{\dot{m}_{nozzle}}{\dot{m}_{real}} \quad 2.16$$

The values of the mass flow ratio are illustrated in the next figure, Figure 37, which is obtained from the simulation data for the radial leakages.



**Figure 37. Mass flow ratio calculations for the radial leakages depending on the Reynolds number and the radial leakage gap [47]**

This correction term can be acquired from the following correlation which is developed based on 12000 simulation points [47]:

$$M = \frac{\alpha_0 \left(\frac{L}{L_0}\right)^{\alpha_1}}{\alpha_2 \left(\frac{\delta}{\delta_0}\right)} [\xi (\alpha_4 R_e^{\alpha_5} + \alpha_6) + (1 - \xi)(\alpha_7 R_e^{\alpha_8} + \alpha_9)] + \alpha_{10} \quad 2.17$$

The  $\xi$  refers to the cross-over term and is calculated by:

$$\xi = \frac{1}{1 + \exp[-0.01 \cdot (Re - Re')]} \quad 2.18$$

Moreover, the coefficients from  $a_0$  to  $a_{10}$  as well as the  $Re'$  are given by the following table, Table 4. [47]

**Table 4. Coefficients used for the radial leakage model**

<i>Coefficient</i>	<i>Value</i>	<i>Coefficient</i>	<i>Value</i>
$a_0$	2.59321070e+04	$a_6$	-1.28861161e-02
$a_1$	9.14825434e-01	$a_7$	-1.51202604e+02
$a_2$	-1.77588568e+02	$a_8$	-9.99674458e-01
$a_3$	-2.37052788e-01	$a_9$	1.61435039e-02
$a_4$	-1.72347611e+05	$a_{10}$	8.25533457e-01
$a_5$	-1.20687600e+01	$Re'$	5.24358195e+03

Consequently, the corrected mass flow is given by:

$$\dot{m}_{corr} = \frac{\dot{m}_{nozzle}}{M} \quad 2.19$$

➤ Flank flow paths

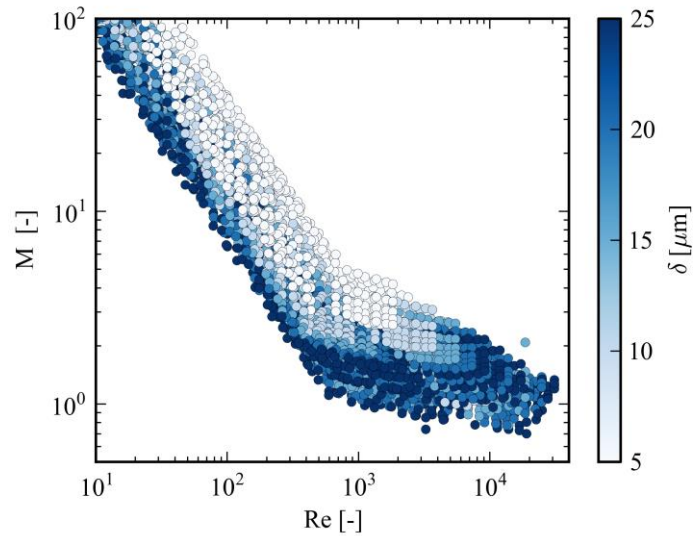
The flank flow paths are situated between the scroll wraps of the expander. Following the same methodology as with the radial leakages, the isentropic nozzle model (through the relative IsentropicNozzle function) is used for the calculation of the mass flow rate.

Although the  $\dot{m}_{nozzle}$  correlation is also the same even for the case of flank leakages, the throat area for the flank leakages is defined:

$$A = h_s \cdot \delta_f \quad 2.20$$

In this analysis, both  $\delta_f$  and  $\delta_r$  amount to 20 $\mu$ m.

Where the  $h_s$  presents the height of the scroll and  $\delta_f$  is the flank gap between the inner wall of one scroll and the outer wall of the other scroll. The numerical data which refer to the mass flow ratio connected with the flank leakages are presented in the following figure, Figure 38, as a function of the Reynolds number and the flank leakage gap.



**Figure 38.** Mass flow ratio calculations for the flank leakages depending on the Reynolds number and the radial leakage gap [47]

By this investigation, the coefficients for the mass flow ratio linked to the flank leakages are given in the subsequent table, Table 5.

**Table 5.** Coefficients used for the flank leakage model

<i>Coefficient</i>	<i>Value</i>	<i>Coefficient</i>	<i>Value</i>
$a_0$	-2.63970396e+00	$a_6$	-5.10200923e-01
$a_1$	-5.67164431e-01	$a_7$	-1.20517483e+03
$a_2$	8.36554999e-01	$a_8$	-1.02938914e+00
$a_3$	8.10567168e-01	$a_9$	6.89497786e-01
$a_4$	6.17402826e+03	$a_{10}$	1.09607735e+00
$a_5$	-7.60907962e+00	$Re'$	8.26167178e+02

### 2.3.2 Heat transfer and pressure drop models

Primarily, the heat transfer and the pressure drop models are used in an effort to determine the heat flux and the pressure drop that occur in the inlet and the outlet tubes of the scroll expander.

In each tube either the inlet node or the outlet node is known. More specifically, in the tube affiliated with the suction of the scroll expander, the thermodynamic state of the node in the inlet of this tube is known, whereas in the outlet tube, the outlet conditions are known. By using the function IsothermalWallTube for a given mass flow rate, the conditions in the outlet of the inlet tube and in the inlet of the outlet tube are calculated. This function involves all the correlations, which are described in the following sections of this report, associated with the heat transfer and pressure drop models.

Furthermore, some assumptions are established in the formation of these models. In other words, the flow can be characterized as homogeneous and turbulent simultaneously. Apart from that, in the case of two-phase flow, the evaporation or the condensation of the working fluid is carried out.

It can be also mentioned that the refrigerant exchanges heat with the expander shell. The temperature linked to the expander wall is equal to  $T_{wall}$ , and as a result, the respective heat delivered from the working fluid to the wall and vice versa,  $\dot{Q}_{wall}$ , is defined by the following expression:

$$\dot{Q}_{wall} = \alpha \cdot (T_{wall} - T_{mean}) \cdot D \cdot \pi \cdot L \quad 2.21$$

In eq. 2.21, the  $\alpha$  presents the heat transfer coefficient in the tube,  $T_{mean}$  is the mean temperature related to the known state and  $D$  and  $L$  are the inner diameter and the length of the tubes correspondingly. Having calculated the exchanged heat transfer and determined the mean enthalpy in a specific node and the mass flow rate of the working fluid, the enthalpy of the refrigerant in an unknown state can be evaluated using the following equation:

$$h = h_{mean} + \frac{\dot{Q}_{wall}}{\dot{m}} \quad 2.22$$

### 2.3.2.1 Heat transfer calculation in the tubes

#### Two-phase

First of all, depending on the direction of the heat transfer that happens in the tubes, the procedure can be characterized either as evaporation or as condensation. To be more precise, if the temperature of the tubes' walls ( $T_{wall}$ ) is higher than the mean temperature of the refrigerant ( $T_{mean}$ ), an evaporation process will be conducted. The condition in which  $T_{wall}$  is lower than  $T_{mean}$  entails the condensation procedure. In this section, the semi-empirical correlations related to both evaporation and condensation are presented for two-phase flow. [51]

➤ **Correlations of Shah evaporation**

Primarily, the two-phase heat transfer coefficient is defined as:

$$a_{2\phi} = \psi \cdot a_l \quad 2.23$$

In eq. 2.24,  $a_l$  depicts the pure-liquid heat transfer coefficient and is calculated by the following equation:

$$\alpha_l = 0.023 \left( \frac{G \cdot (1 - x) \cdot D}{\mu_f} \right)^{0.8} Pr_f^{0.4} \frac{k_f}{D} \quad 2.24$$

In this certain correlation,  $G$  constitutes the mass flux and can be estimated by:

$$G = \frac{\dot{m}}{A} \quad 2.25$$

Moreover,  $\mu_f$ ,  $Pr_f$  and  $k_f$  are the viscosity, the Prandtl number and the thermal conductivity of the refrigerant. For a given isobaric heat capacity ( $c_p$ ), the Prandtl number can be estimated as:

$$Pr = \frac{\mu \cdot c_p}{k} \quad 2.26$$

In order to determine the  $\psi$  parameter, it is necessary to conduct the following calculations:

In the first stage, three non-dimensional numbers are defined, with  $x$  being the vapor quality of the working fluid:

The convection number:

$$C_o = \left( \frac{1}{x} - 1 \right)^{0.8} \sqrt{\frac{\rho_f}{\rho_g}} \quad 2.27$$

The Froude number:

$$Fr_l = \frac{G^2}{\rho_f^2 g D} \quad 2.28$$

The boiling number:

$$Bo = \frac{q''}{G \cdot h_{fg}} \quad 2.29$$

The  $\rho_g$  and  $\rho_l$  refer to the densities of the saturated vapor and liquid of the refrigerant respectively, whereas  $h_{fg}$  depicts the vaporization enthalpy. Finally,  $q''$  constitutes the heat flux.

Subsequently, the  $F$  and  $N$  parameters of the Shah evaporation are estimated:

$$F = \begin{cases} 14.70, Bo > 0.0011 \\ 15.43, Bo \leq 0.0011 \end{cases} \quad 2.30$$

$$N = \begin{cases} C_o, Fr_l \geq 0.04 \\ 0.38, Fr_l^{-0.3} C_o, Fr_l < 0.04 \end{cases} \quad 2.31$$

Before the coefficient  $\psi$  being computed, the  $\psi_{bs}$ ,  $\psi_{nb}$  and  $\psi_{cb}$  should be calculated by utilizing the next equations:

The convective boiling number:

$$\psi_{cb} = \frac{1.8}{N^{0.8}} \quad 2.32$$

The nucleate boiling number:

$$\psi_{nb} = \begin{cases} 230\sqrt{Bo}, & N > 0.1 \text{ and } Bo > 0.00003 \\ 1 + 46\sqrt{Bo}, & N > 0.1 \text{ and } Bo < 0.00003 \end{cases} \quad 2.33$$

The  $\psi_{bs}$ :

$$\psi_{bs} = \begin{cases} F\sqrt{Bo} \exp(2.74N^{-0.15}), & 0.1 \leq N \leq 1.0 \\ F\sqrt{Bo} \exp(2.74N^{-0.10}), & N < 0.1 \end{cases} \quad 2.34$$

And lastly:

$$\psi = \begin{cases} \max(\psi_{bs}, \psi_{cb}), & N \leq 0.1 \\ \max(\psi_{nb}, \psi_{cb}), & N > 0.1 \end{cases} \quad 2.35$$

### ➤ Correlations of Shah condensation

In terms of the Shah condensation, the overall two-phase heat transfer coefficient for a specific vapor quality is:

$$\alpha_{2\phi} = a_l \left( (1-x)^{0.8} + \frac{3.8x^{0.76}(1-x)^{0.04}}{(p^*)^{0.38}} \right) \quad 2.36$$

In the above equation,  $p^* = p_{sat}/p_{crit}$  and  $a_l$  is estimated by:

$$\alpha_l = 0.023 \left( \frac{G \cdot D}{\mu_f} \right)^{0.8} Pr_f^{0.4} \frac{k_f}{D} \quad 2.37$$

### Single-phase

In the case of single-phase flow, the heat transfer coefficient is calculated based on the Gnielinski model. Thus, the Nusselt number is given by:



$$Nu = \frac{f}{8} \cdot (Re - 1000) \cdot \frac{Pr}{1 + 12.7 \cdot \sqrt{\frac{f}{8}} \cdot Re^{0.6666} - 1} \quad 2.38$$

Where  $f$  constitutes the friction factor and can be estimated by applying the eq. 2.41. Consequently, the heat transfer coefficient is given by:

$$a_{1\varphi} = k \cdot \frac{Nu}{D} \quad 2.39$$

### 2.3.2.2 Pressure drop calculation in the tubes

In the following calculations, it is assumed that the flow is homogeneous. Firstly, the pressure gradient is given by the following correlation:

$$\frac{dp}{dz} = \frac{-f \cdot G^2}{2 \cdot D \cdot \rho} \quad 2.40$$

Where  $\rho$  is the density of the fluid,  $G$  is the mass flux and  $D$  is the hydraulic diameter. The parameter  $f$  presents the friction factor and depending on the flow's genre (single or two phase), the following correlations are used.

The friction factor is computed for the single-phase flow based on the Churchill (1977) correlation (relied on a Darcy friction factor where  $f_{\text{laminar}}=64/Re$ ):

$$f = 2 \left[ \left( \frac{8}{Re_D} \right)^{12} + \frac{1}{(A + B)^{1/3}} \right]^{1/12} \quad 2.41$$

And  $A$  and  $B$  parameters are defined:

$$A = \left[ -2.457 \cdot \log \left[ \left( \frac{7}{Re_D} \right)^{0.9} + 0.27 \cdot \left( \frac{\varepsilon}{D} \right) \right] \right]^{16} \quad 2.42$$

$$B = \left( \frac{37,530}{Re_D} \right)^{16} \quad 2.43$$

Where  $\varepsilon$  is the roughness and  $D$  is the hydraulic diameter of the tube.

To estimate the friction factor when the flow is two-phase, the Blasius (1913) correlation is used:

$$f = \frac{0.079}{Re_{dh}^{0.25}}, \quad 3,000 < Re_{dh} < 100,000 \quad 2.44$$

Once the pressure gradient is calculated, the pressure drop is easy to be prescribed by multiplying with the length (L) of the tube.

$$\Delta p = \frac{dp}{dz} \cdot L \quad 2.45$$

### 2.3.3 Performance assessment indexes

In this section, the divergent performances of a scroll expander as well as the electrical and mechanical power are defined.

Primarily, the adiabatic efficiency of a scroll expander:

$$\eta_{ad} = \frac{h_1 - h_2}{h_1 - h_{2s}} \quad 2.46$$

Where  $h_1$  and  $h_2$  constitute the enthalpies in the inlet and outlet of the working fluid at the machine correspondingly. Moreover,  $h_{2s}$  is the isentropic enthalpy that refers to the outlet of the expander. The adiabatic efficiency contributes to the determination of the deviation between the real and the isentropic expansion of the fluid.

The volumetric efficiency can be computed by:

$$\eta_{vol} = \frac{\dot{m}_{ref}}{\omega/2\pi \cdot V_{disp}/V_{ratio} \cdot \rho_{inlet}} \quad 2.47$$

In eq. 2.45,  $\dot{m}_{ref}$  is the mass flow rate that circulates through the scroll machine,  $V_{disp}$  is the displacement volume,  $V_{ratio}$  is the built-in volume ratio and  $\rho_{inlet}$  is the density of the refrigerant in the inlet of the scroll expander. The volumetric efficiency represents the ratio of the real mass flow rate to the theoretical mass flow rate for the same rotational speed.

The isentropic performance is calculated according to the following correlation:

$$\eta_{is} = \frac{\dot{W}_{el}}{\dot{m}_{ref}(h_1 - h_{2s})} \quad 2.48$$

The  $\dot{W}_{el}$  depicts the net electrical power produced by the scroll expander and is estimated by:

$$\dot{W}_{el} = \dot{W}_{mech} - \dot{W}_{motor,los} \quad 2.49$$

The mechanical power is:

$$\dot{W}_{mech} = \eta_{ml} \dot{W}_{PV} \quad 2.50$$

Where  $\eta_{ml}$  is the mechanical efficiency and is equal to:

$$\eta_{ml} = 1 - \frac{\dot{m}_{ref} \cdot (h_1 - h_2)}{\dot{W}_{PV}} \quad 2.51$$

Finally, using the generator efficiency  $\eta_g$ , the motor losses can be calculated.

$$\dot{W}_{motor,los} = (1 - \eta_g) \dot{W}_{mech} \quad 2.52$$

### 2.3.4 Scroll energy balance

In order to apply the energy conservation balance on the scroll expander, a single-lump energy balance model is established. A crucial assumption introduced in the model is that there are no temperature deviations in the scroll shell and every point of the scroll shell has a temperature value equal to  $T_{wall}$ . The following equations describe the heat transfer phenomena that occur during the scroll expander operation.

Primarily, the heat transported from the scroll shell to the ambient and vice versa is given by the next correlation:

$$\dot{Q}_{amb} = h_{amb} \cdot A_{shell} \cdot (T_{wall} - T_{amb}) \quad 2.53$$

Where  $h_{amb}$  constitutes the free convection heat transfer coefficient between the shell and the ambient, with its value standing at 0.02 kW/m<sup>2</sup>K, and  $A_{shell}$  is the shell external surface.

The heat exchanged between the refrigerant and tubes is described in the previous section in detail, while the heat transfer conducted between the CVs is not analyzed in this thesis.

Lastly, the mechanical losses of the scroll turned into heat transmitted to the scroll shell. Using the mechanical performance of the scroll,  $\eta_{ml}$ , is easy to define these mechanical losses:

$$\dot{W}_{ml} = (1 - \eta_{ml}) \cdot \dot{W}_{PV} = \dot{m}(h_{in} - h_{out}) \quad 2.54$$

As it is illustrated in the following equation, the heat delivered by the scroll to the ambient is equal to the total heat exchanged from the working fluid in the control volumes and tubes to the shell summing them with the heat due to the mechanical losses. In this study, the heat flux among the divergent CVs is disabled.

$$\dot{Q}_{tubes} + \dot{W}_{ml} + \dot{Q}_{CV} = \dot{Q}_{amb} \quad 2.55$$

### 2.3.5 Deterministic model solution algorithm

The deterministic model algorithm involves the flow, heat transfer and pressure drop model described in the previous sections. In the next figure (Figure 39) the applied solver of the deterministic model is illustrated.

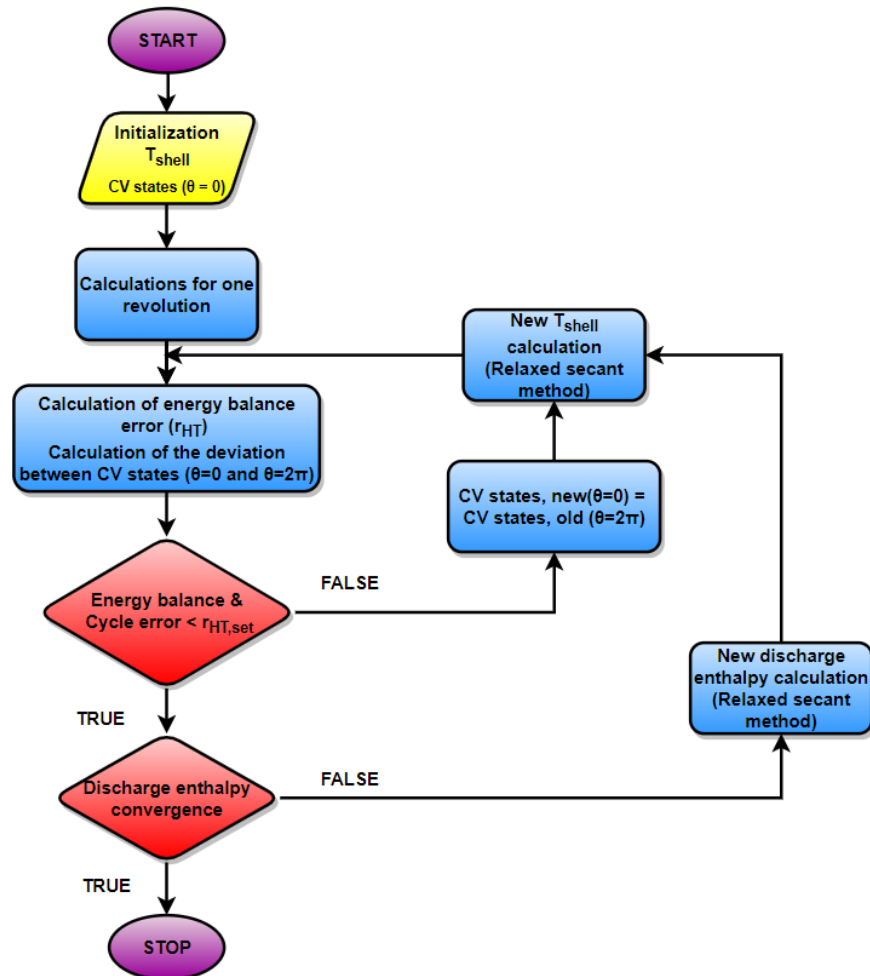


Figure 39. Deterministic model solver

The key stages of this algorithm are the following:

- By giving some initial inputs to the model, the model begins the calculations by assuming guess values for the wall temperature, mass flow rate, adiabatic efficiency (and hence state of the refrigerant at scroll outlet) and working fluid states at the CVs of the scroll at the beginning of the rotation ( $\theta=0$ rad).

- Subsequently, the heat transfer and pressure drop models for the tubes are executed so as to identify the states of refrigerant at the inlet and outlet of the scroll chambers (outlet of inlet tube and inlet of outlet tube).
- The simulation is carried out for one revolution and for sequentially timesteps (angles) starting from  $\theta=0$  until  $\theta=2\pi$ . At each timestep/angle, firstly the flow models are implemented to evaluate the mass flow rates which circulate through the CVs and between the inlet/outlet tubes and the CVs of the scroll. Next, the heat transfer model in the CVs is executed to identify the heat exchanged between the working fluid in each control volume and the shell. In the subsequent stage, relied on the calculated flow CV heat transfer and mass flow rates, the states of the working fluid in the CVs at the next timestep/angle are determined by applying the correlations of the mass and energy balance in CVs. In the PDSim model, an adaptive Runge–Kutta–Fehlberg (RK45) method is used for the incorporation of these equations.
- At the end of the rotating procedure, not only is the deviation between the state parameters of the CVs at  $\theta=0$  and  $2\pi$  defined, namely the error\_CVs, but the residual of the scroll energy balance equation is also calculated, given by the next equation:

$$r_{HT} = \dot{Q}_{tubes} + \dot{Q}_{CV} + \dot{W}_{ml} - \dot{Q}_{amb} \quad 2.56$$

While the values of error\_CVs and the energy balance residual are higher than a certain tolerance threshold, the states of the CVs at the end of the revolution are implemented as inputs in order to initialize the CVs for the next revolution. At the same time, a new guess value is selected for the shell temperature using the relaxed secant method.

- Once the error\_CVs and  $r_{HT}$  values become smaller than these particular tolerance thresholds, the discharge enthalpy is specified by using the following equation:

$$h_{disc} = \frac{\sum_{disc} \dot{m} h}{\sum_{disc} \dot{m}} \quad 2.57$$

To be more precise, the discharge enthalpy is calculated as the average enthalpy of the working fluid at the scroll outlet throughout a whole revolution. The discharge energy residual is estimated as the product of the difference of the calculated ( $h_{disc}$ ) and assumed ( $h_{disc,a}$ ) discharge enthalpies and the mass flow rate, according to the following equation:

$$r_{mh} = \dot{m}(h_{disc} - h_{disc,a}) \quad 2.58$$

Should the energy residual be lower than the specific tolerance threshold, the solver stops. Unless this happens, a new discharge enthalpy is calculated with the relaxed secant method and is used as assumed value in the next solver repetition.

### 2.3.6 Deterministic model limitations

The developed deterministic model involves several empirical or semi-empirical parameters. These variables should be verified with experimental data or computational fluid dynamics (CFD) methods in order to ensure the model's accuracy in predicting the actual performance of scroll devices. To be more precise, both evaporation and condensation heat transfer coefficients as well as the pressure drop correlations in the tubes need to be calibrated. In particular, these certain correlations should be adjusted to refer to non-homogenous flow effects and discrepancies between transport properties of pseudo-pure fluids and real fluids in the case of refrigerant-oil mixtures. Furthermore, experimental data could render the calculation of the accurate correlations for the behavior of R1233zd(E) feasible.

It must be noted that the mechanical losses in scroll expanders are difficult to be determined accurately because of the multitude of phenomena and components involved (dry friction, elasto-hydrodynamic lubrication, journal bearings, roller bearings). This is partially due to the incapability of decoupling the mechanical losses from the rest of the working process of the scroll machine. This model involves a simplified approach of a fixed mechanical efficiency. However, the experimental results could render the adaptation of accurate correlations for the mechanical efficiency of the scroll expander as a function of operating parameters such as its rotational speed feasible.

Furthermore, the discharge flow path correction factor introduced because of the existence of vena contracta should be recalibrated based on the experimental data for the two-phase scroll expander using R1233zd(E) as the working fluid. The main reason for this necessity is that the adiabatic efficiency of the scroll machine is intensively influenced by this factor. According to Bell's [47] experimental results, this factor is equal to 0.5 for the developed model.

Finally, apart from the discharge flow path correction factor, the other key empirical parameter that should be calibrated is the flow path area correction factor. The effective slip ratio, which constitutes an empirical parameter, accounts for non-homogenous flow effects and exerts a negative impact on the calculated mass flow rate, need to be estimated by taking into account experimental results. The discharge coefficient, which is determined by the geometry of the scroll expander, is necessary to be adapted so as to be attuned to the experimental data.

### 3. Deterministic model results and discussion

#### 3.1 Commercial scroll expander simulation results

In the first section of the chapter, the results of the simulation of the operation of a commercial scroll compressor model considering its use in reverse as an expander as well as a prototype scroll expander are presented. In both cases, the expanders are intended for the realization of a two-phase expansion process which occurs within an Ericsson cycle operating with working fluid R1233zd(E) in the context of the “REGEN-BY-2” research project.

The boundary conditions of the aforementioned two-phase expansion process, which are also the inputs to the deterministic model presented in the previous chapter, are summarized in Table 6.

**Table 6. Operating conditions of the expansion**

<i>Operating parameters</i>	<i>Value/State</i>
<b>Refrigerant</b>	R1233zd(E)
<b>Inlet temperature, <math>T_{inlet}</math> (°C)</b>	60-90
<b>Outlet temperature, <math>T_{outlet}</math> (°C)</b>	30
<b>Ambient temperature, <math>T_{amb}</math> (°C)</b>	25
<b>Rotational speed, n (rpm)</b>	5250 and 3000-6000
<b>Inlet vapor quality, <math>x_{inlet}</math> (-)</b>	0.65-0.85
<b>Mechanical efficiency, <math>\eta_{ml}</math> (%)</b>	98
<b>Generator efficiency, <math>\eta_g</math> (%)</b>	98

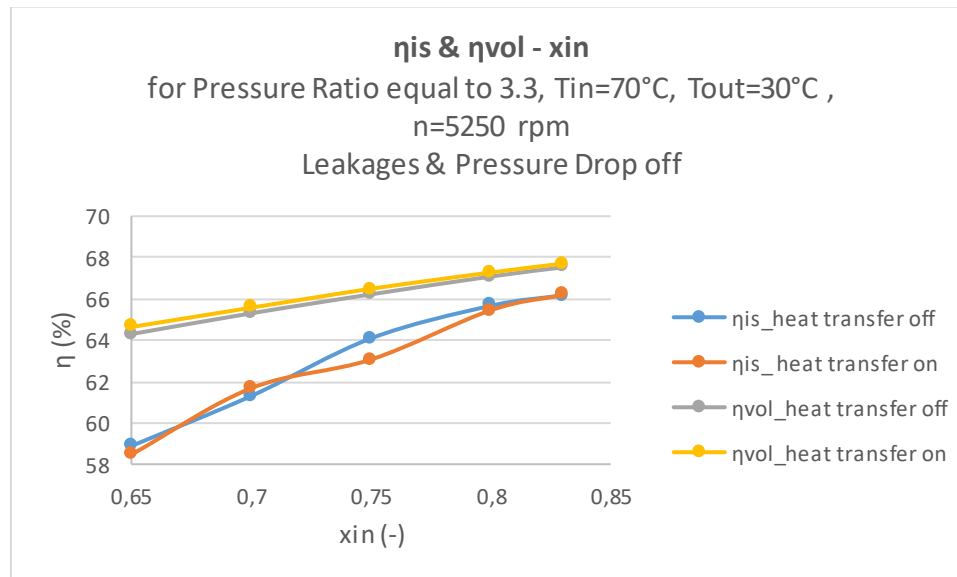
Under the base-case conditions, the suction and discharge saturation temperatures are 70°C and 30 °C respectively, with the corresponding pressure ratio amounting to 3.3. The base-case inlet vapor quality is 0.83 and the base-case rotational speed is 5250 rpm.

In order to investigate the effect of operating conditions, namely the inlet temperature and vapor quality, these are varied while all other operating parameters are assigned their base-case values.

The input geometric parameters to the deterministic model are the displacement volume, the build-in volume ratio, the maximum number of the expansion chambers, the  $\phi_{i0}$ , the  $\phi_{is}$ , the  $\phi_{ie}$ , the  $\phi_{o0}$ , the  $\phi_{os}$ , the radius of base circle, the height of scroll and the orbiting radius. It is also worth pointing out that the discharge geometry of this scroll machine is arc-Line-arc. The exact values of every geometric parameter are not published due to reasons related to confidentiality.

### 3.1.1 Investigation of heat transfer in the tubes

Figure 40 illustrates the values of both isentropic and volumetric efficiencies for different expander inlet qualities, with expander working in a certain pressure ratio for either enabled or disabled heat transfer mode in the inlet and outlet tubes of the device.



**Figure 40. Isentropic and volumetric efficiencies as functions of the inlet vapor quality for activated and deactivated heat transfer and a fixed pressure ratio**

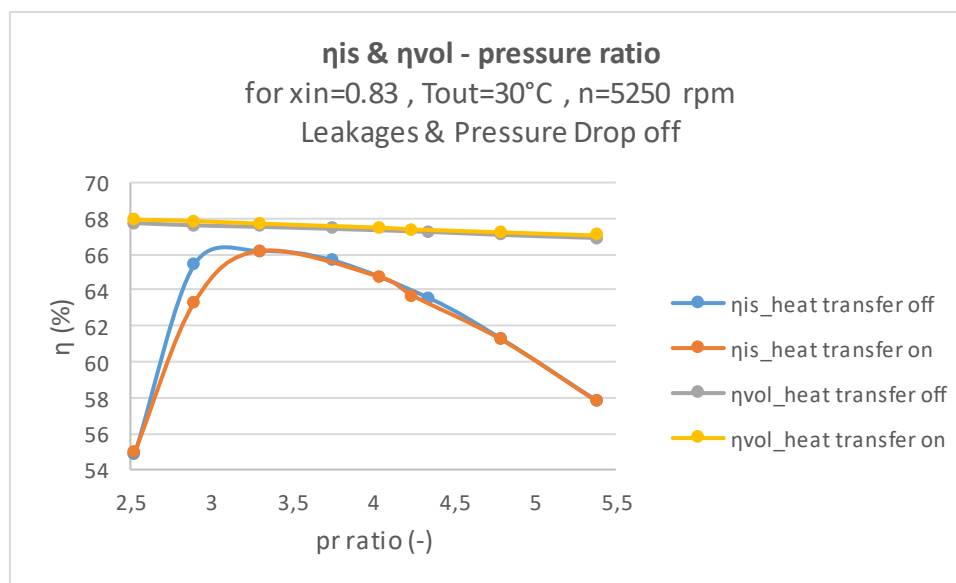
As can be clearly seen from this figure (Figure 40), the increase in the inlet vapor quality leads to increased isentropic performance. In particular, for inlet quality equal to 0.65, the isentropic efficiency reaches approximately 59%, while it peaks at almost 66% in 0.83. Meanwhile, increased inlet vapor quality results in higher generated electrical power but lower mass flow rate. Therefore, according to eq. 2.36, it is indisputable that the isentropic efficiency experiences an increase. Another noticeable feature is that the heat transfer in the tubes exerts a small impact on the isentropic efficiency, with the deviation averaging at around 1%. For inlet vapor qualities near 0.75, the percentages connected with the executions that indulge the heat transfer effects are presented lower than those that refer to the disabled heat transfer. This is due to the fact that the condensation that occurs in the outlet tube is more important than the evaporation conducted in the inlet tube of the scroll expander as the inlet quality drops. More specifically, in the inlet tube, heat is transported from the refrigerant to the tube's walls and hence the enthalpy of the working fluid in the outlet of this tube is decreased. That contributes to the drop of the produced electrical power. In comparison with this, the evaporation carried out in the outlet tube is beneficial for the expander's efficiency. To be more precise, with the enthalpy in the outlet of this specific tube being fixed, the increased heat transfer from the wall to the refrigerant means the decrease in the enthalpy in the discharge region of the expander. Thus, because of the increase in heat transfer Shah's coefficient in low vapor qualities in



condensation, the discharge enthalpy reduces at a lower rate than the suction one, and as a result, the isentropic efficiency is presented lower than the respective without involving the heat transfer phenomenon for these values of inlet vapor qualities. As the quality rises, this deviation becomes smaller because of the gradual weakening of condensation carried out in the suction tube.

Regarding the volumetric efficiency, it increases as the inlet vapor quality goes up. In particular, the increase of inlet quality contributes to the substantial reduction of refrigerant density. Since this decline is more significant than those of mass flow rate, according to equation 2.35, the volumetric efficiency experiences a growth. In inlet quality equal to 0.65 and 0.83, the values average at approximately 64.4% and 67.7% correspondingly. Finally, it is observed that the heat transfer is advantageous to a small extent in terms of volumetric efficiency.

The following figure, Figure 41, presents the influence of the heat transfer to the isentropic and volumetric performances for different pressure ratios corresponding to expander inlet saturation temperatures from 60°C to 90°C for inlet vapor quality of 0.83.



**Figure 41. Isentropic and volumetric efficiencies as functions of the pressure ratio for activated and deactivated heat transfer and a fixed inlet vapor quality**

The isentropic efficiency is maximized for a pressure ratio of 3.3, under which the volume expansion ratio matches with the expander built-in volume ratio. For lower or higher values of pressure ratios, over- and under- expansion losses occur and hence the performance of the scroll expander is penalized. In other words, the expander operation in lower pressure ratios entails the decrease of the specific volume ratio, and consequently, provokes over-expansion losses. When the imposed pressure ratio overcomes the pressure ratio of the design point, under- expansion losses take place. For  $T_{in}=60^{\circ}\text{C}$ , the isentropic performance reaches 54.97%,

and after its maximization at almost 66%, it undergoes a downward trend, until it stands at around 57.8%. These results verify that the over-expansion phenomenon is more detrimental for the isentropic efficiency. Finally, it is also worth pointing out that throughout the pressure ratio range, the deviation between the two curves is marginal.

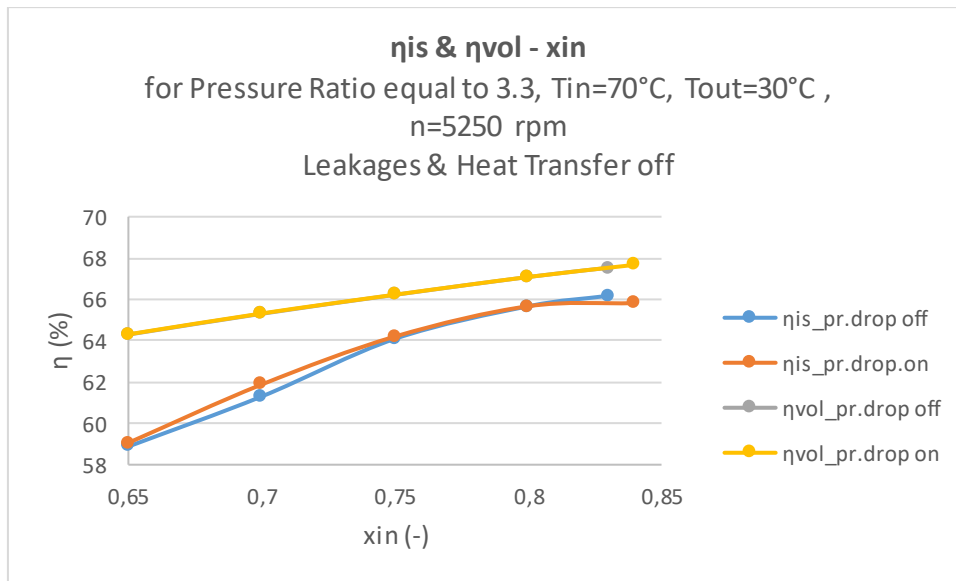
Furthermore, the increase in the inlet temperature leads to the steady linear decline of the volumetric efficiency, as can be noticed from Figure 41. Although the mass flow rate increases with the growth of the pressure ratio, the rise of density has stronger effects on the volumetric efficiency. It can also be observed that despite the positive influence of heat transfer in the volumetric efficiency, the latter peaks only at just below 68% for inlet temperature equal to 60°C.

### 3.1.2 Investigation of pressure drop in the tubes

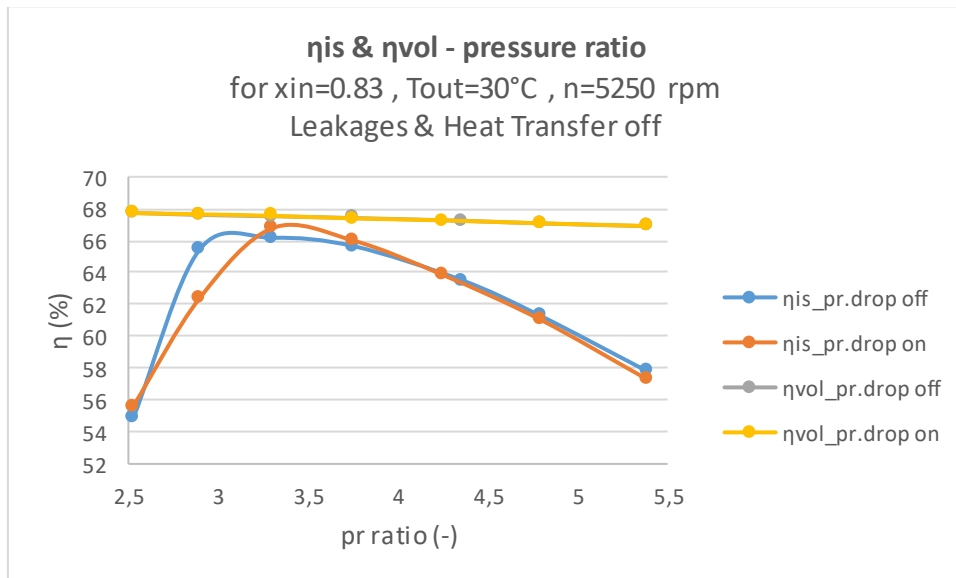
Figure 42 displays the effect of pressure drops in the tubes on both isentropic and volumetric efficiencies for different inlet vapor qualities. Increasing inlet vapor quality causes the decline of isentropic performance rise at increasing qualities. As the increase of the inlet quality provokes the decrease in the working fluid density in the suction line and the pressure drops are more intense. However, the aforementioned degradation has a minimal influence on the isentropic efficiency, which shows a moderate growth from 59% to 65.67% from inlet vapor qualities varying from 0.65 to 0.8, while it is stabilized at 65.82% for 0.84.

As it can be seen in Figure 43, for pressure ratios lower than 3.3, which is in accordance with the built-in volume ratio, the isentropic efficiency decline reaches just above 3%. When under-expansion losses take place, the reduction of this efficiency is not substantial. It can be also mentioned that the isentropic efficiency is maximized for higher pressure ratio when the pressure drop model is implemented. This is due to the fact that the pressure drops contribute to the decrease in the over-expansion losses.

Finally, the tube pressure drop does not significantly affect the volumetric performance, which exhibits a small increase due to the pressure drop in the suction.



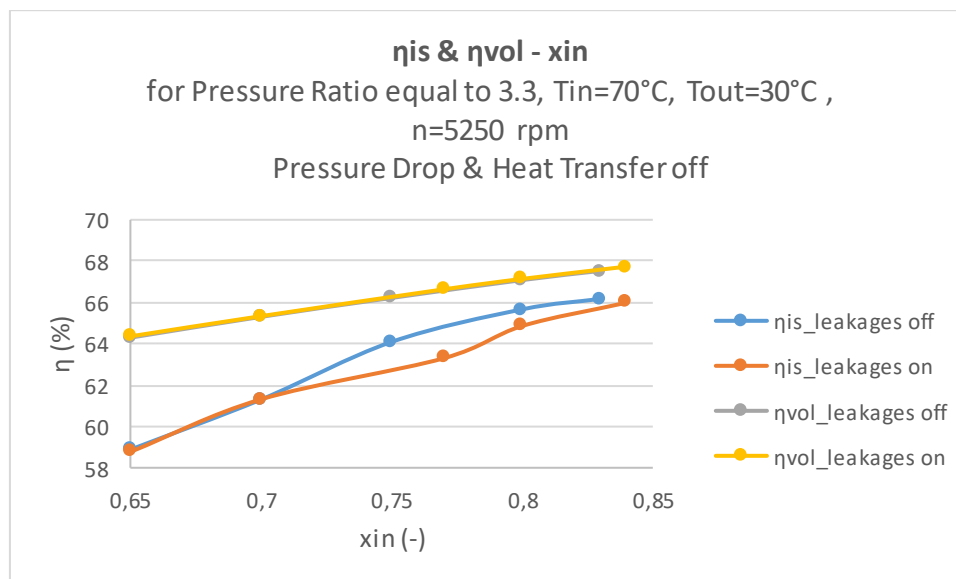
**Figure 42.** Isentropic and volumetric efficiencies as functions of the inlet vapor quality for activated and deactivated pressure drop and a fixed pressure ratio



**Figure 43.** Isentropic and volumetric efficiencies as functions of the pressure ratio for activated and deactivated pressure drop and a fixed inlet vapor quality

### 3.1.3 Investigation of leakages

Primarily, Figure 44 illustrates the influence of leakages in the isentropic and volumetric efficiencies of the scroll expander for varied inlet vapor qualities. The former performance grows for the highest qualities. Apart from that, it can be noticed that when the inlet quality becomes higher than 0.7, the negative effects of the leakage losses are more considerable. However, the related deviations never exceed 2.5%. It is important that, compared to the other two models, namely heat transfer and pressure drop, the consequences derived from the existence of leakages are more severe. Moreover, because of the use of semi-empirical correlations the leakage model, their accurate calculation requires model calibration with experimental data. Figure 44 also shows how the existence of leakages, both radial and flank ones, affects the volumetric efficiency for the divergent inlet vapor qualities. Undeniably, this influence can be considered negligible.

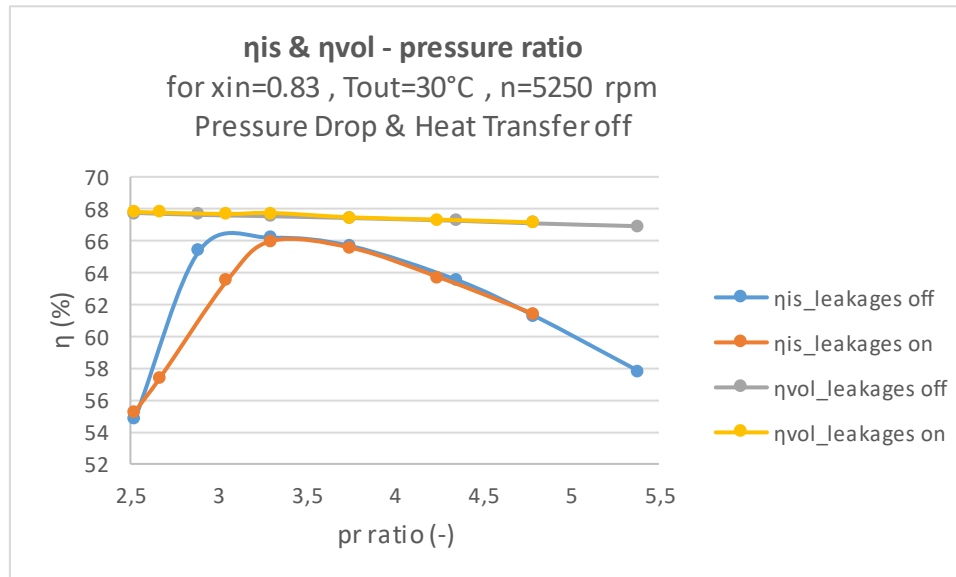


**Figure 44. Isentropic and volumetric efficiencies as functions of the inlet vapor quality for activated and deactivated leakages and a fixed pressure ratio**

In the next graph, the isentropic and volumetric performance as functions of the pressure ratio are presented for enabled and disabled leakages. Note that the semi-empirical correlation that describes the leakages are applied for pressure ratios ranged from 1.58 to 4.87. As a result, the maximum inlet temperature that is used in the simulations is 85°C.

As it can be seen in Figure 45, there is only a small divergence between the two curves just above the optimum and designed pressure ratio (3.3). The maximum value when the leakage losses are included is approximately 66%. For higher pressure ratios, the leakages bear no effect on the expander performance. It is also worth pointing out then for lower pressure ratios, the

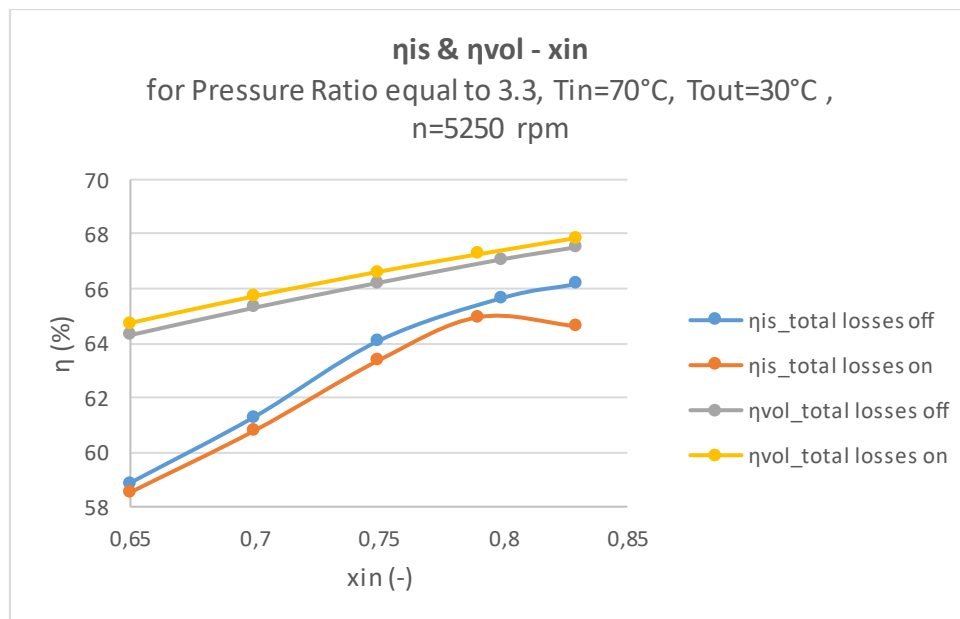
leakage losses deteriorate the over-expansion phenomenon, penalizing more the isentropic efficiency. Regarding the volumetric efficiency, the leakages exert some small positive impacts throughout the whole pressure ratio range.



**Figure 45. Isentropic and volumetric efficiencies as functions of the pressure ratio for activated and deactivated leakages and a fixed inlet vapor quality**

### 3.1.4 Total influence of the internal losses

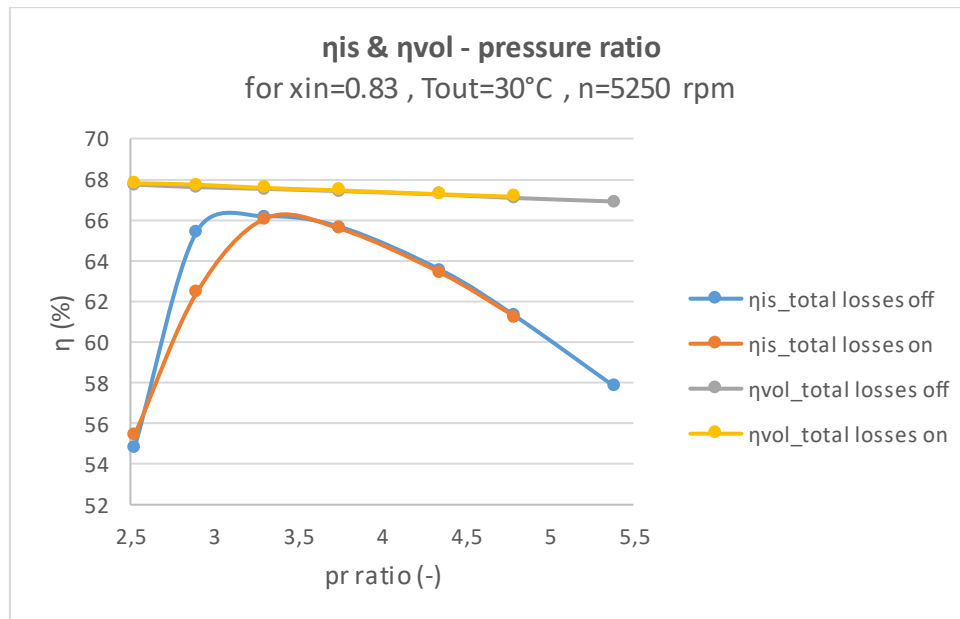
In this stage, heat transfer, leakages and pressure drop models are simultaneously enabled in an effort to examine their cumulative influence. As depicted in Figure 46 leakages and heat transfer lead to lower isentropic performance. For inlet vapor quality equal to 0.65, the isentropic efficiency is 58.53%, exhibiting a moderate increase until it peaks at around 65% for inlet quality being 0.8 and subsequently decreasing to 64.6% for inlet vapor quality of 0.83. Furthermore, Figure 46 shows the variation of the volumetric efficiency for different values of inlet vapor quality. Although the corresponding executions indicate the positive impacts that these two modes exert in the volumetric, which are caused mainly by the heat transfer operation, the influence is slightly insignificant. That is why the highest deviation between these two curves is about 0.42%. Finally, as can be seen from this graph, these performances fluctuate from 64.65% to approximately 68%.



**Figure 46. Isentropic and volumetric efficiencies as functions of the inlet vapor quality for activated and deactivated total internal losses and a fixed pressure ratio**

Figure 47 depicts the correlation between isentropic efficiency and pressure ratio when both leakages, pressure drops and heat transfer are activated. It is evident that the maximum isentropic efficiency is achieved for a pressure ratio equal to 3.3, being equal to 66%. The total influence is small because the higher deviation is around 3% and happens for a pressure ratio of 2.89.

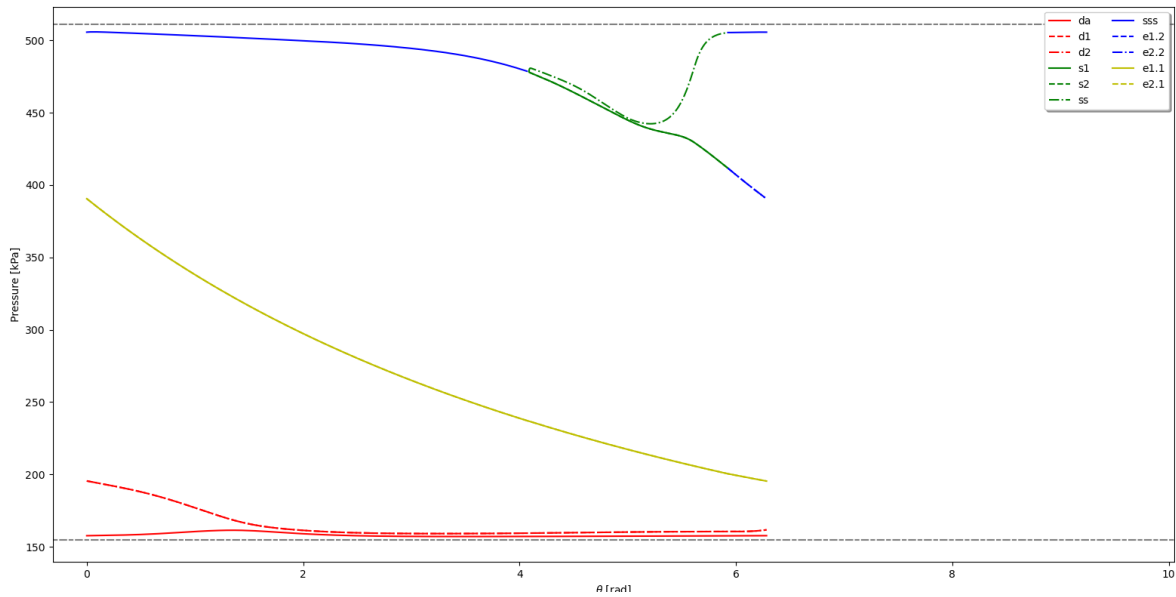
As Figure 47 demonstrates, the volumetric efficiency is slightly below 68% for a pressure ratio equal to 2.5, reaching 67.14% for a pressure ratio of 4.79. The cumulative phenomena do not affect the volumetric efficiency as the pressure ratio changes. In general, as the suction pressure is increased, the volumetric efficiency drops as the increase in the suction pressure leads to the increase in the leakage mass flow rate that circulates through the orifices and throttling losses occur in the suction and discharge ports, according to [38]. Thus, the mass flow rate is reduced, and in turn, the volumetric performance declines.



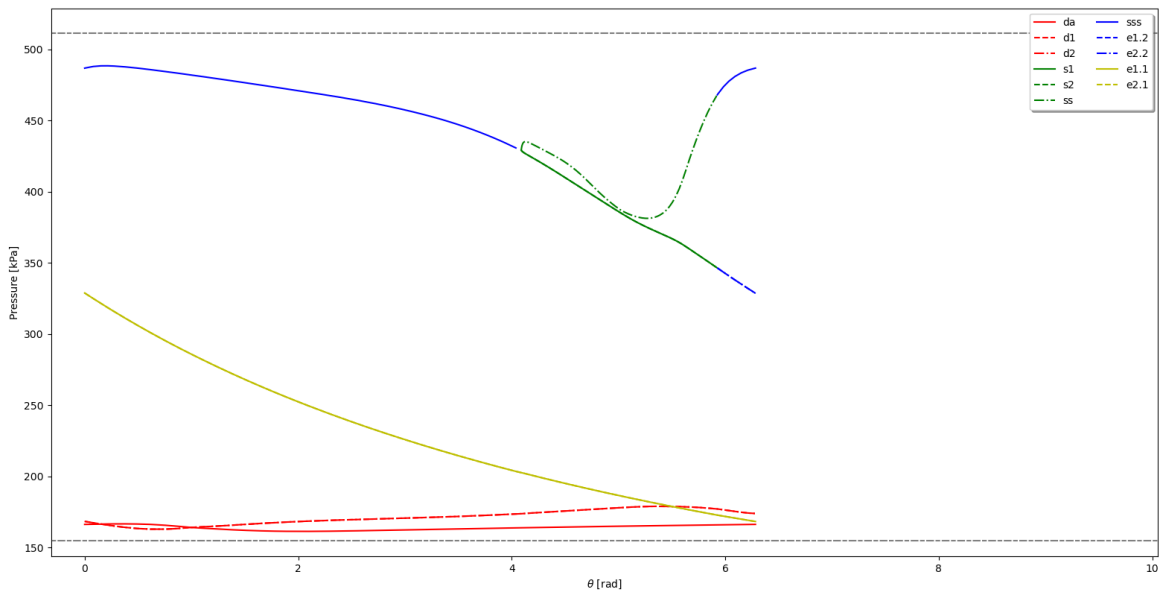
**Figure 47.** Isentropic and volumetric efficiencies as functions of the pressure ratio for activated and deactivated total internal losses and a fixed inlet vapor quality

### 3.1.5 Parametric investigation of the influence of the rotational speed

In this section, for these conditions, fixed pressure ratio and inlet vapor quality adapted to the design point, the isentropic and volumetric performances are investigated for divergent values of rotational speeds, varying from 3000rpm to 6000rpm. Firstly, the pressure drops in the tubes are activated and the impacts of leakages and heat transfer are evaluated and then, the pressure drops are disabled and this procedure is repeated. As can be seen clearly from the Figure 50, Figure 51, Figure 52 and Figure 53, both efficiencies decrease for higher rotational speed. It is indisputable that the increase in the rotational speed entails the deterioration of the throttling losses and hence the reduction of the time required for the filling of the expansion chamber. That provokes the decrease of both mass flow rate and output power, whereas these variables increase as the rotational speed goes up ideally. As a result, the volumetric efficiency is subjected to a downward trend as the Figure 50 and Figure 52 illustrate. It can be also mentioned that this phenomenon is not influenced substantially by the imposed conditions (leakages, pressure drops in tubes and heat transfer in tubes). In addition, since the increasing rotational speed provokes the decline in the suction pressure, it results in a drop in the isentropic performance. That decrease in the suction pressure is illustrated in Figure 48 and Figure 49, in which the pressure distribution in the chambers of the expander is depicted for rotational speeds equal to 3000 rpm and 6000 rpm respectively. Although more severe under-expansion losses occur in the case of 3000 rpm, the drop in the suction pressure values causes the isentropic performance decrease as the rotational speed increases.



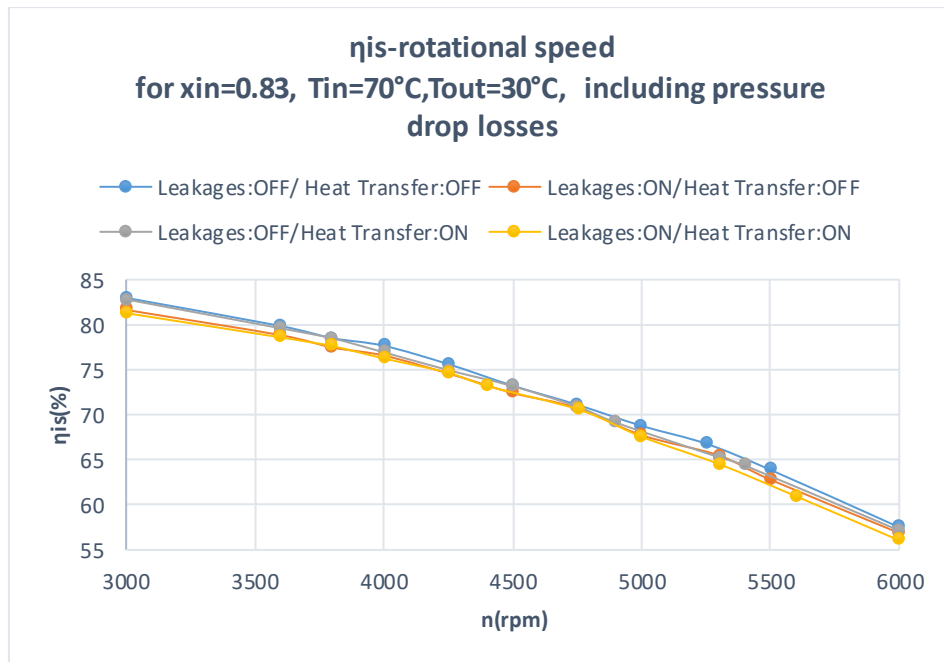
**Figure 48. Pressure distribution in scroll expander chambers as a function of the rotating angle for 3000 rpm**



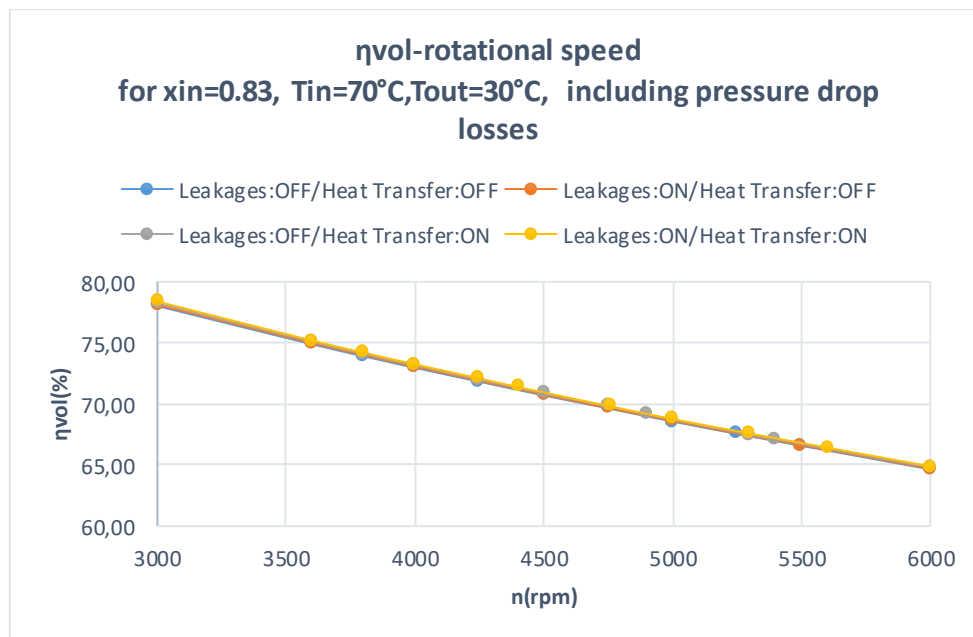
**Figure 49. Pressure distribution in scroll expander chambers as a function of the rotating angle for 6000 rpm**

In particular, the isentropic efficiency is 82% in 3000rpm and drops significantly to almost 57% in 6000rpm. Finally, it is observed that the concurrent existence of pressure drops, leakages and heat transfer exert a negative impact on the isentropic performance.

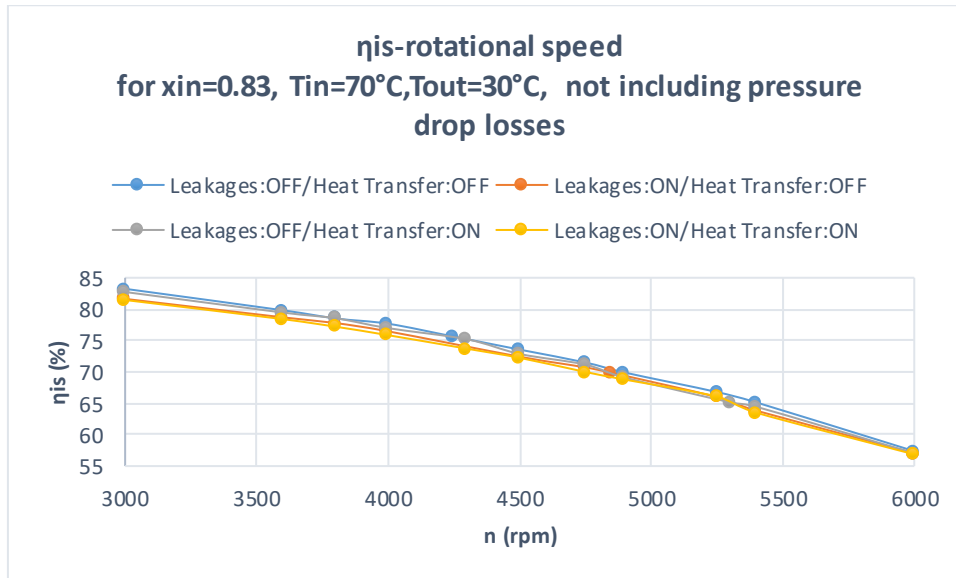




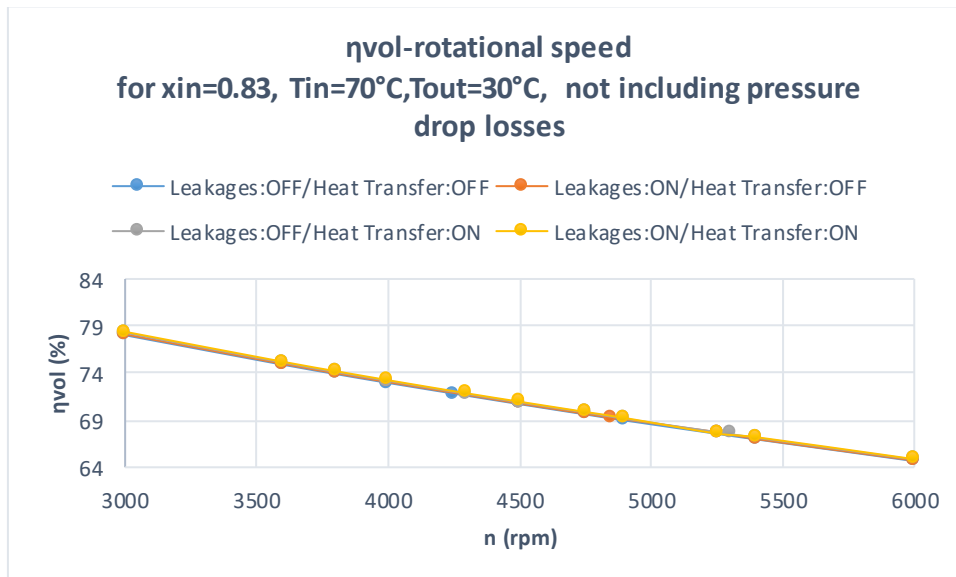
**Figure 50.** Isentropic efficiency as a function of the rotating speed for activated and deactivated both leakages and heat transfer, fixed inlet vapor quality and enabled pressure ratio



**Figure 51.** Volumetric efficiency as a function of the rotating speed for activated and deactivated both leakages and heat transfer, fixed inlet vapor quality and enabled pressure ratio



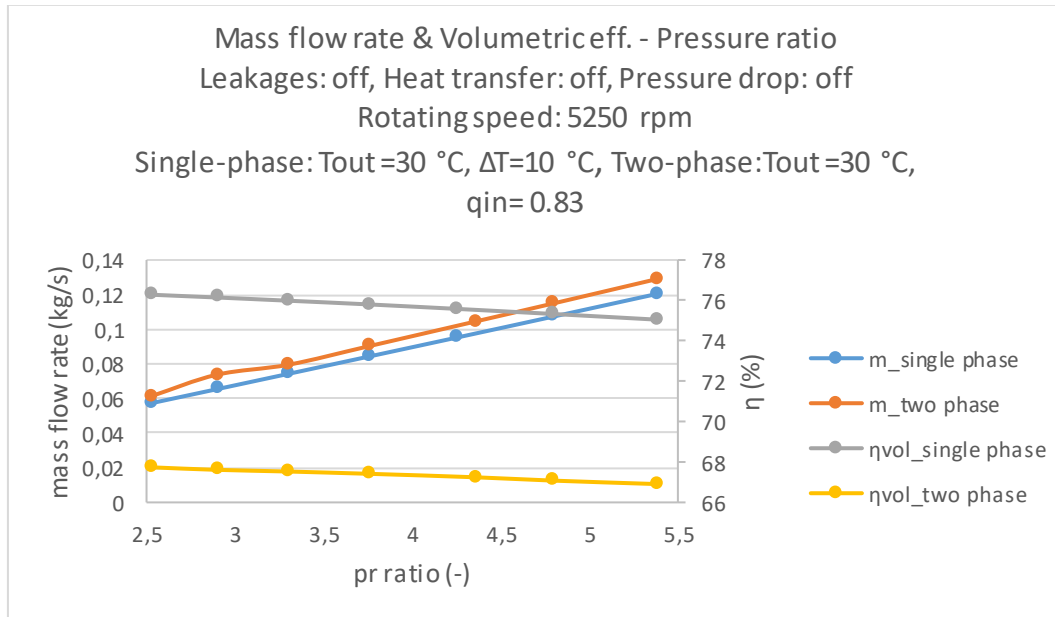
**Figure 52.** Isentropic efficiency as a function of the rotating speed for activated and deactivated both leakages and heat transfer, fixed inlet vapor quality and deactivated pressure ratio



**Figure 53.** Volumetric efficiency as a function of the rotating speed for activated and deactivated both leakages and heat transfer, fixed inlet vapor quality and deactivated pressure ratio

### 3.1.6 Comparison between single-phase and two-phase flows

Primarily, in the two-phase region, the latent heat of boiling is added to the liquid portion of the two-phase flow. This phenomenon can lead to the conversion of the liquid to vapor in the mixture, but without the rising of the mixture's temperature. Thus, the main advantage of two-over single-phase expansion is the possible increase in specific expansion work due to the higher density and mass flow rate of the refrigerant, despite the lower volumetric efficiency, as shown in Figure 54.



**Figure 54. Mass flow rate and volumetric performance as functions of pressure ratio for both single-phase and two-phase flows, leakages off, heat transfer off, pressure drop off**

Nevertheless, as shown in Figure 55, the two-phase expansion is associated with substantially lower enthalpy drop in the expander (as reflected by the lower isentropic) efficiencies, resulting in overall lower expansion work compared to single-phase expansion.

The aforementioned reduced enthalpy drop in two-phase expansion can be explained through Figure 56 and Figure 57, in which the pressure variation of the working fluid in the expansion chambers as a function of the rotation angle is depicted.

More specifically, in two-phase expansion, due to the greater mismatch between the expansion volume flow ratio and the built-in volume ratio, severe over-expansion losses occur. This is displayed in Figure 56 and Figure 57, since the deviation of the pressure at the end of the expansion chamber with the pressure in the discharge line is higher for the two-phase flow. Notably, the difference in the isentropic efficiency is about 15%.

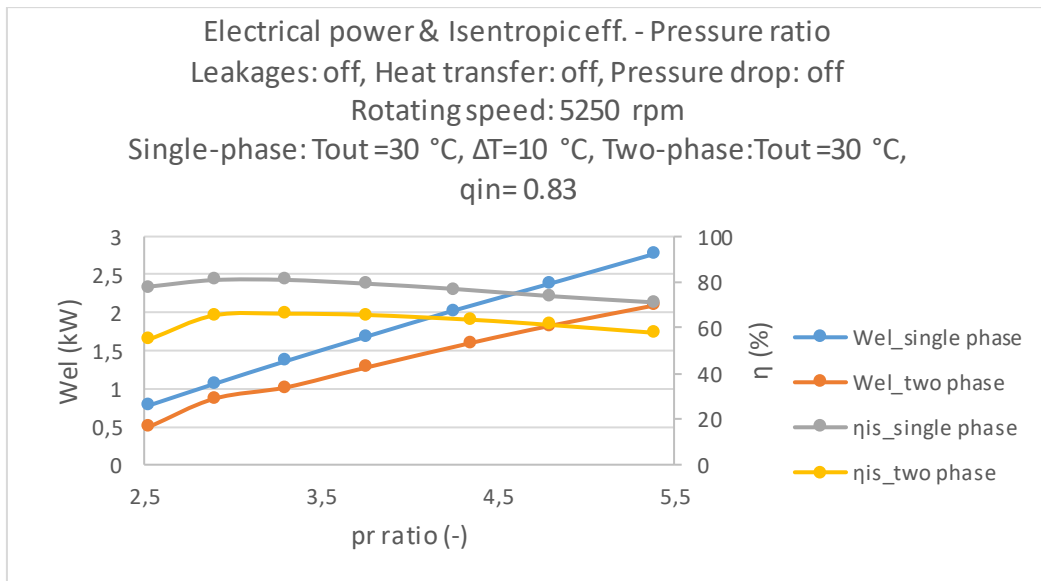


Figure 55. Electrical power and isentropic performance as functions of pressure ratio for both single-phase and two-phase flows, leakages off, heat transfer off, pressure drop off

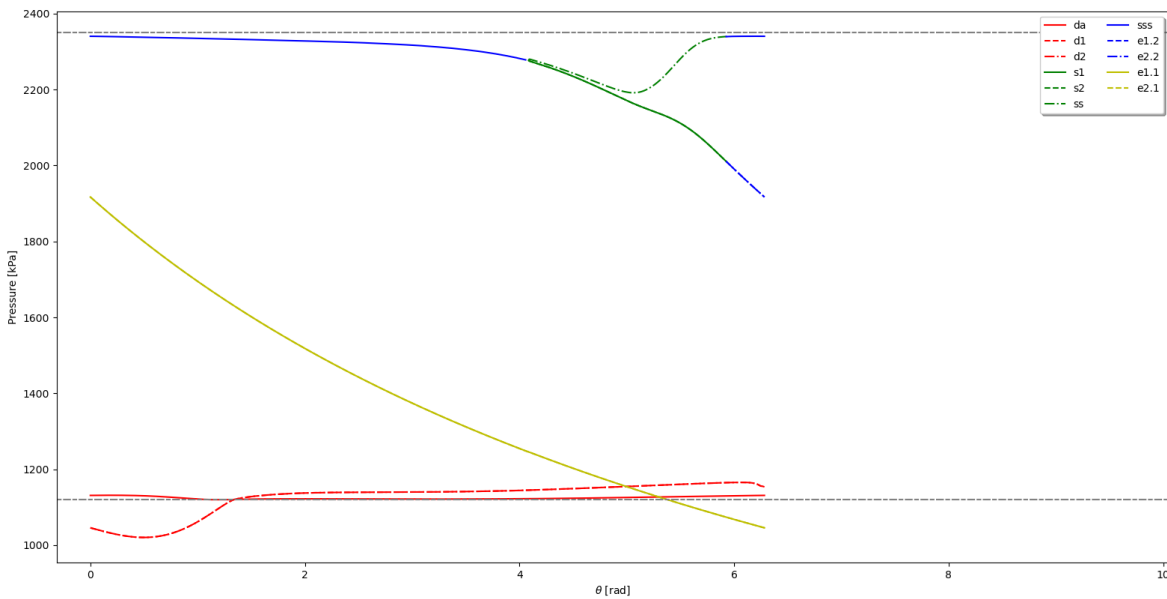
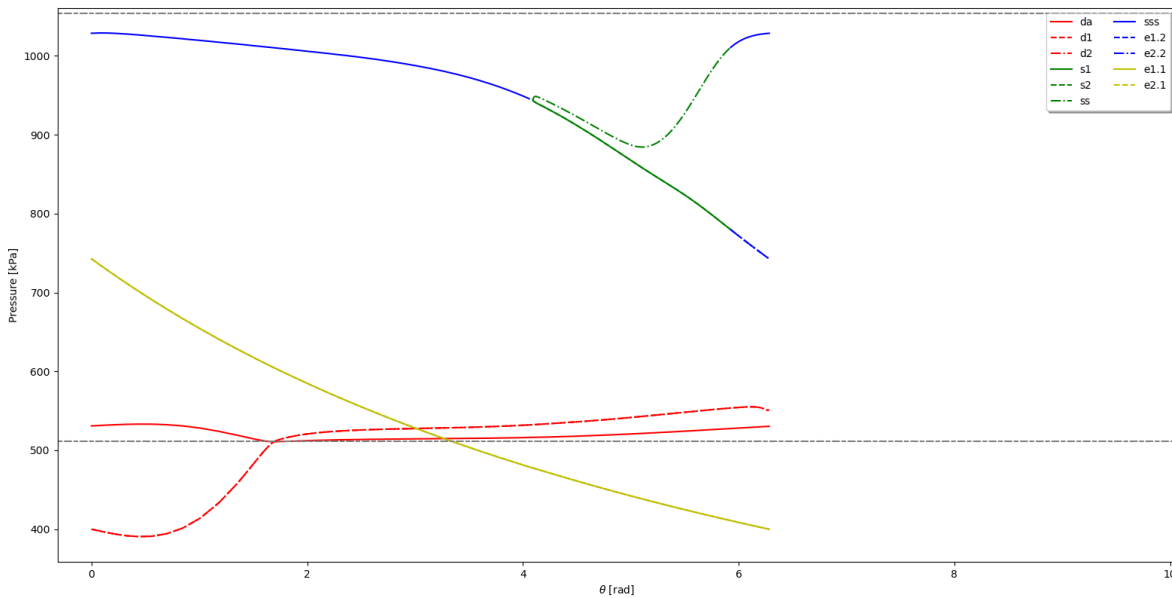
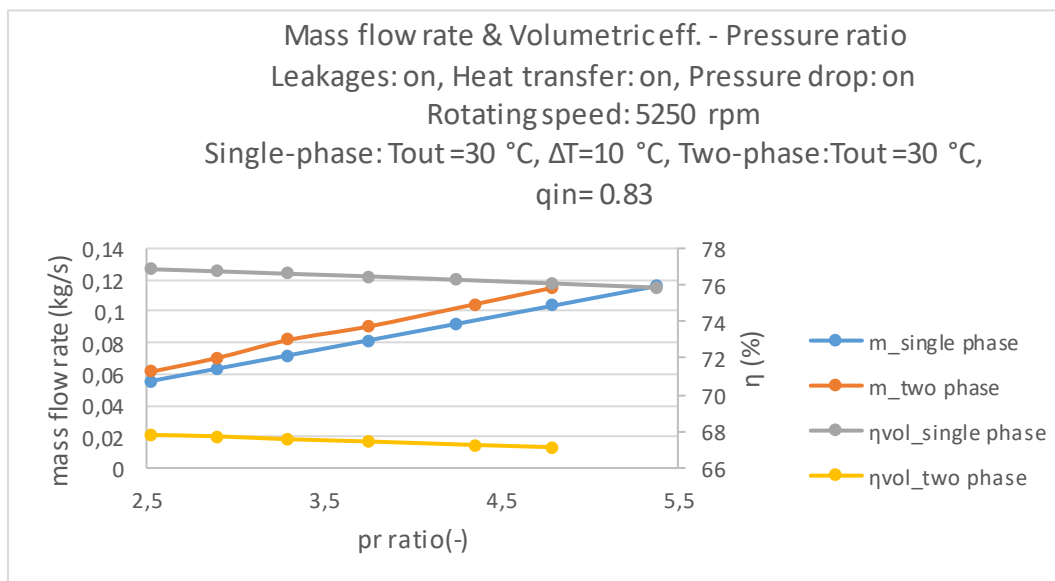


Figure 56. Pressure distribution in scroll expander chambers as a function of the rotating angle for the single-phase flow



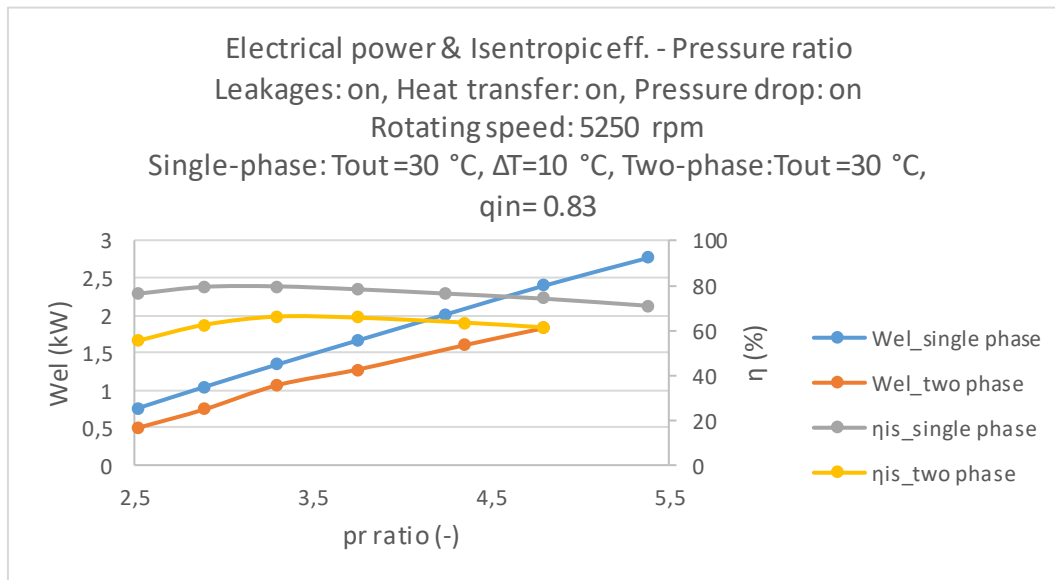
**Figure 57. Pressure distribution in scroll expander chambers as a function of the rotating angle for the two-phase flow**

The same procedure is carried out for the investigation of single-phase flow that involves leakage, heat transfer and pressure drop (Figure 58 and Figure 59).



**Figure 58. Mass flow rate and volumetric performance as functions of pressure ratio for both single-phase and two-phase flows, leakages on, heat transfer on, pressure drop on**

Even though the produced electrical power and isentropic efficiency are slightly lower when heat transfer, pressure drop and leakage losses are integrated in the executions, the qualitative results in this occasion are similar to those in which these losses are absent. This is shown in Figure 59. Comparing these data with the results illustrated in Figure 55, the isentropic efficiency experiences a marginal decrease due to the activation of the leakages, pressure drop and heat transfer. For pressure ratio equal to 3.3, the isentropic efficiency drop for single-phase expansion is around 1%, whereas for two-phase expansion reaches only about 0.1%.



**Figure 59. Electrical power and isentropic performance as functions of pressure ratio for both single-phase and two-phase flows, leakages on, heat transfer on, pressure drop on**

### 3.2 Prototype scroll expander simulation results

In this section, the impacts of some geometrical variables on the adiabatic and volumetric efficiencies for four different geometries of a prototype scroll expander. The operating and other boundary conditions are similar to the case of the commercial scroll, shown in Table 6. The nose profile in all cases is arc-arc (or two-arc). As for the given parameters,  $\varphi_{i_o}$ ,  $\varphi_{i_s}$ ,  $\varphi_{i_e}$ ,  $\varphi_{o_o}$ ,  $\varphi_{o_s}$ ,  $\varphi_{o_e}$ , the radii  $r_o$ ,  $r_b$  as well as both the thickness ( $t$ ) and the height of the scroll wraps ( $H$ ) are inputs to the geometry model. Meanwhile, a perfect meshing profile is considered; thus, the equation 2.6 is implemented. Finally, for all geometries, the pockets of the expander are considered symmetrical. The main geometrical parameters ( $\varphi_{i_s}$ ,  $\varphi_{o_s}$  and inlet port area) are firstly varied so as to examine their influence on expander performance. Afterwards,  $\varphi_{i_s}$  and  $\varphi_{o_s}$  are kept constant in order for the expander performance to be maximized and the suction port area and built-in volume ratio are varied.

### 3.2.1 Investigation of involutes angles and inlet port areas

The involute angles and inlet port area are varied simultaneously. The changes in angles take place in order to increase the suction area by exploiting the entire surface area between the scrolls. However, the volume ratio should not be decreased substantially.

In the analysis of the present section, Case 1 refers to the lowest values of these parameters, whereas the Case 4 to the highest ones. As it can be seen from the Figure 60 (a), the initial increase in all these parameters from Case 1 to Case 2 exerts beneficial impacts on the expander adiabatic efficiency, which is maximized at 81.8 % in Case 2. However, as the respective angles and the initial port area are increased further, the adiabatic performance drops steadily. It is worth pointing out that the sharp growth of the inlet port surface between the Case 3 and Case 4 results in a further decrease in this performance, standing at a little more than 65%. On the other hand, the volumetric efficiency is constantly increasing from 70% (Case 1) to 85.47% (Case 4) According to Figure 61, the electrical power also follows this trend, varying from 1.66 kW to 2.84 kW.

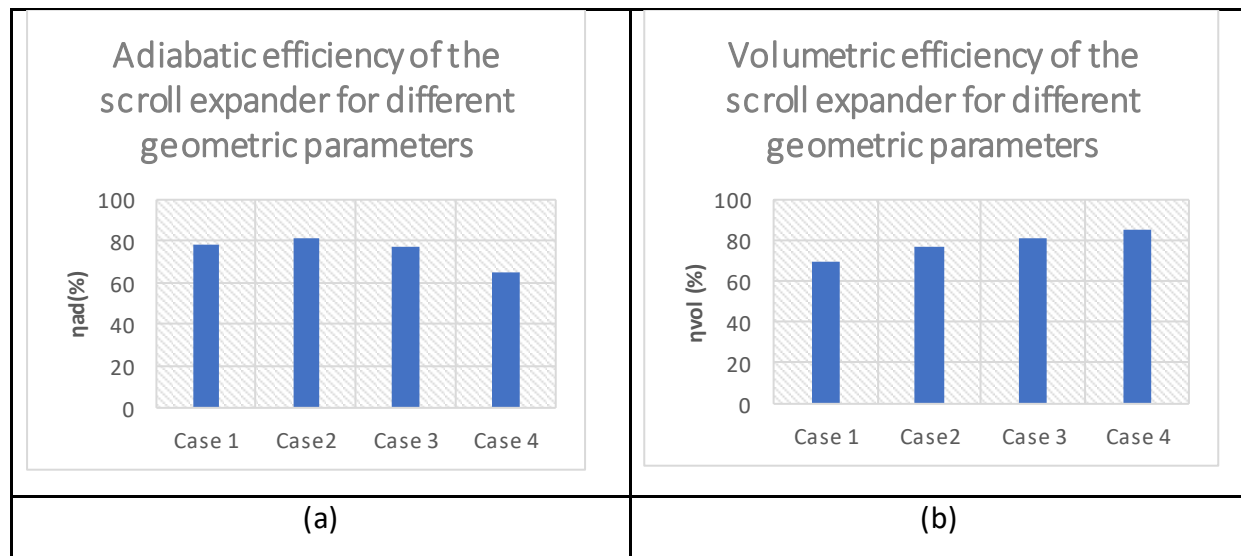
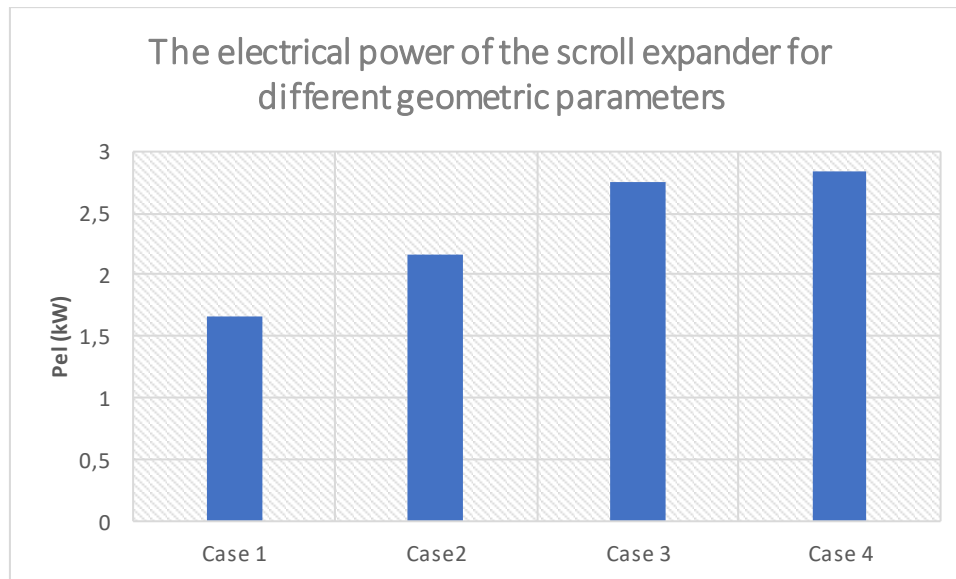


Figure 60.(a) Adiabatic and (b) volumetric efficiency for each geometry case



**Figure 61. Produced electrical power for the four applied cases**

In the investigated expander geometry, suction chambers  $s_1$  and  $s_2$  are turned into expansion chambers  $e_{1.3}$  and  $e_{2.3}$ , and then into  $e_{1.2}$  and  $e_{2.2}$ , and after into  $e_{1.1}$  and  $e_{2.1}$  respectively. The existence of additional expansion chambers  $e_{1.1}$  and  $e_{2.1}$  requires a relatively high built-in volume ratio. This is followed by the creation of the discharge chambers,  $d_1$  and  $d_2$ , in the discharge angle. The pocket  $da$  is formed at the end of the expansion process.

Primarily, in the next line graphs, namely in Figure 61, Figure 62, Figure 63 and Figure 64, the pressure distribution in the chambers of the expander for the four cases is shown. In all diagrams, there is a continuity in pressures that characterizes each pocket. As it can be observed, at the beginning of the expansion procedure, the pressure of  $sss$  chamber drops because of the intense decline of the effective suction area. That is due to the fact that the suction port is cut off by the rotating scroll wrap, according to Lemort et al. (2009) [30]. Furthermore, the pressure is represented on an equal footing at the split angle for the  $ss$  and for the  $s_1$  and  $s_2$ , which constitute the suction chambers. However, in terms of the central pocket ( $ss$ ), the relative pressure decreases steadily until it reaches its minimum value as a result of the rise of the suction chamber volume. Hereupon it increases since the flow area between the inlet port and the suction chamber grows and hence the throttling losses go down. On the other hand, the pressure of the two symmetrical chambers ( $s_1$  and  $s_2$ ) declines due to the leakages occurred through scroll wrap clearance. Subsequently,  $s_1$  and  $s_2$  are replaced by the expansion chambers, namely  $e_{1.3}$  and  $e_{2.3}$  and then by  $e_{1.2}$  and  $e_{2.2}$  and possibly by  $e_{1.1}$  and  $e_{2.1}$ , with the substantial decline of the corresponding pressures, while  $ss$  is transformed to  $sss$ . It should be mentioned that the downward trend is more abrupt in cases of the  $e_{1.3}$  and  $e_{2.3}$  formation and the  $e_{1.2}$  and  $e_{2.2}$  creation than this of  $e_{1.1}$  and  $e_{2.1}$ . This is because, at the switching from  $s_1$  and  $s_2$  to  $e_{1.3}$  and  $e_{2.3}$  correspondingly, the refrigerant that circulates from the suction pockets to the expansion



ones has extremely high velocity. This phenomenon is also encouraged by the important radial leakages that take place in this certain stage. These results can be also verified by the study of M. Wei et al. [20]. The higher volume increase during the creation of  $e_{1.1}$  and  $e_{2.1}$  contributes to the gradual decrease of their pressure loads. Finally, the dominant pressure in chambers  $d_1$ ,  $d_2$  and  $d_a$  should be almost equal to the respective pressure of the discharge line. However, due to the model's instability, these values vary throughout the expander rotation.

In Figure 62, Figure 63, Figure 64 and Figure 65, the influence of the  $\varphi_{i,s}$ ,  $\varphi_{o,s}$  and inlet port area on the pressure profile in each chamber is depicted.

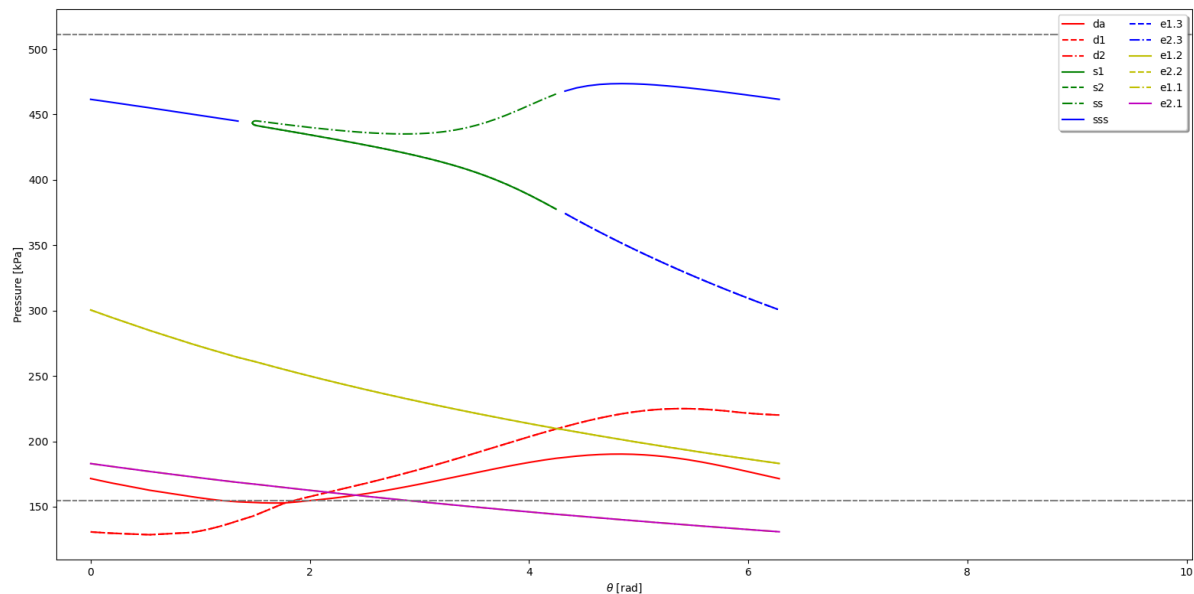
First of all, it is observed that the increase in these geometrical parameters entails the rise of the pressure loads in the suction chambers. In particular, in Case 1, the suction pressure does not exceed 500 kPa, but in Case 4 (Figure 65), the pressure in  $sss$ ,  $ss$ ,  $s_1$  and  $s_2$  overcomes this number. As for the impacts of the suction pressures on the volumetric efficiency, it is essential to highlight that the suction pressure does not affect it but influences the adiabatic performance of a scroll expander considerably. To be more precise, this growth contributes to the increase in the adiabatic efficiency. However, this trend is not depicted in Figure 60 (a) because of the intense over- or under- expansion losses that take place and are described in the next paragraphs in detail. Moreover, the extremely small inlet port area in Case 1 leads to pressure losses that occur between the inlet port and the suction chamber. This is one of the reasons why the adiabatic performance in Figure 60(a) is presented lower for Case 1 comparing with the efficiency displayed for Case 2. It is also observed that as the initial involute angles go up and the surface of the suction line increases, the split and discharge angles are transferred into higher rotating angles. Case 4 constitutes the most noticeable case since the suction stage begins with the  $ss$ ,  $s_1$  and  $s_2$  pockets instead of the creation of  $sss$ .

The values of pressure that characterize the expansion stage are inextricably linked to those of the suction process. In other words, the higher the amount of the fluid pressure in the suction pockets, the larger the imposed pressures in the expansion chambers. It is also worth pointing out that in Case 4, due to the excessive increase in the inlet port area and the growth of  $\varphi_{i,s}$  and  $\varphi_{o,s}$ , which are related to the reduction of the volume ratio, resulting in the nonexistence of  $e_{1.1}$  and  $e_{2.1}$ . From a design standpoint, the dimensions of the scroll expander should be smaller in this case.

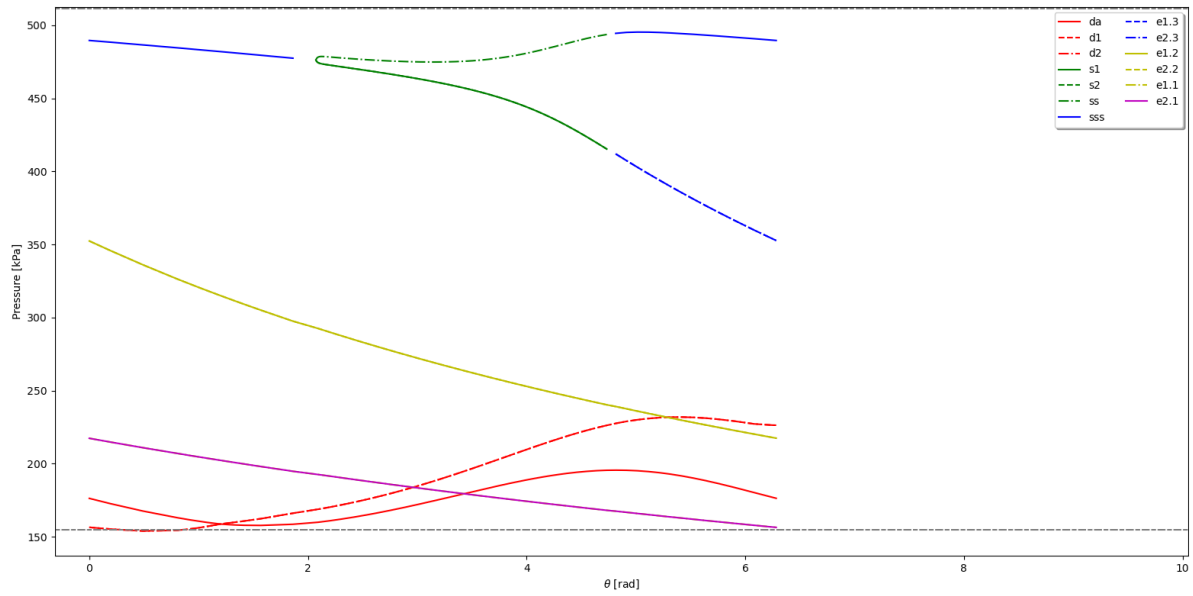
According to Figure 62 that refers to Case 1, in which the built-in volume ratio is the highest, over-expansion losses occur because the pressure in the discharge line is higher than the pressure at the expansion chamber at the end of the cycle. That may lead to a back flow, and consequently, there is a need for valve involvement into the simulation model. As Figure 63 illustrates for the Case 1, the pressure at the end of  $e_{2.1}$  chamber is equal to the pressure of the discharge line, leading to the nonexistence of both over- and under- expansion losses. This fact combined with the relatively high suction pressure values result in an optimized adiabatic efficiency. In the rest cases, namely in Case 3 and Case 4, only under- expansion losses occur,

based on Figure 64 and Figure 65 correspondingly. These under-expansion losses are directly associated with the fact that the pressure at the end of  $e_{2,1}$  is higher than the pressure in the discharge line (the lowest broken grey line). Although the over-expansion losses are more detrimental for the scroll expander's efficiencies than the under-expansion losses in general, the scroll expander exhibits the lowest adiabatic performance for the Case 4 due to the largest deviation between the pressure at the end of the expansion chamber and the discharge line pressure.

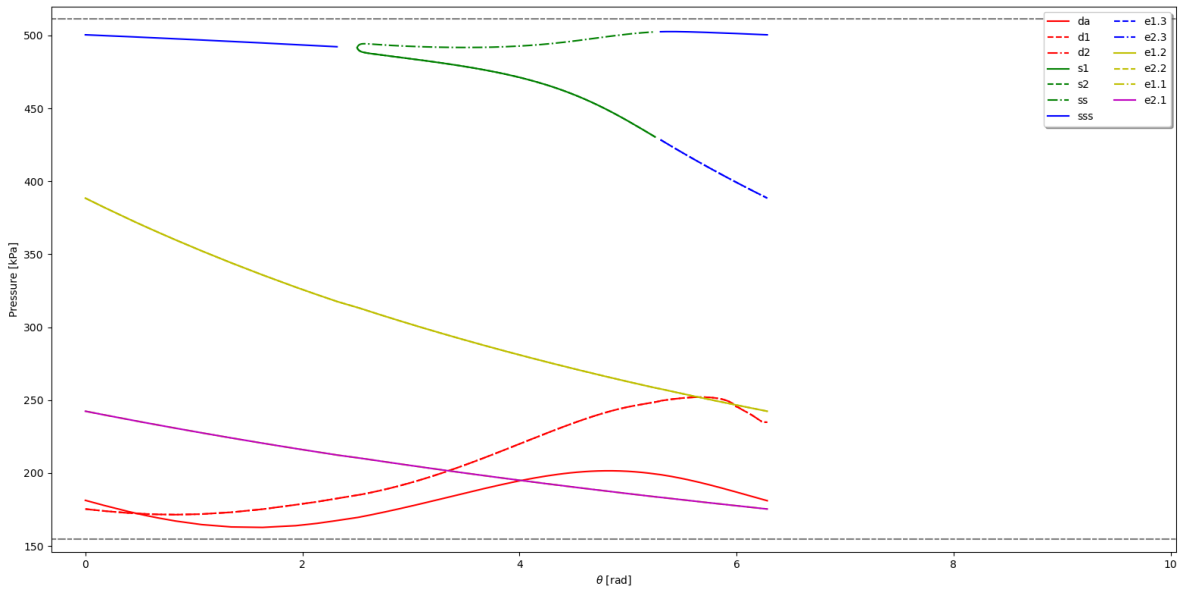
Regarding the volumetric efficiency, the mass flow rate upward trend is dominant due to the substantial increase in the inlet port area and thus resulting in the rise of the volumetric performance of the expander. (Figure 60 (b))



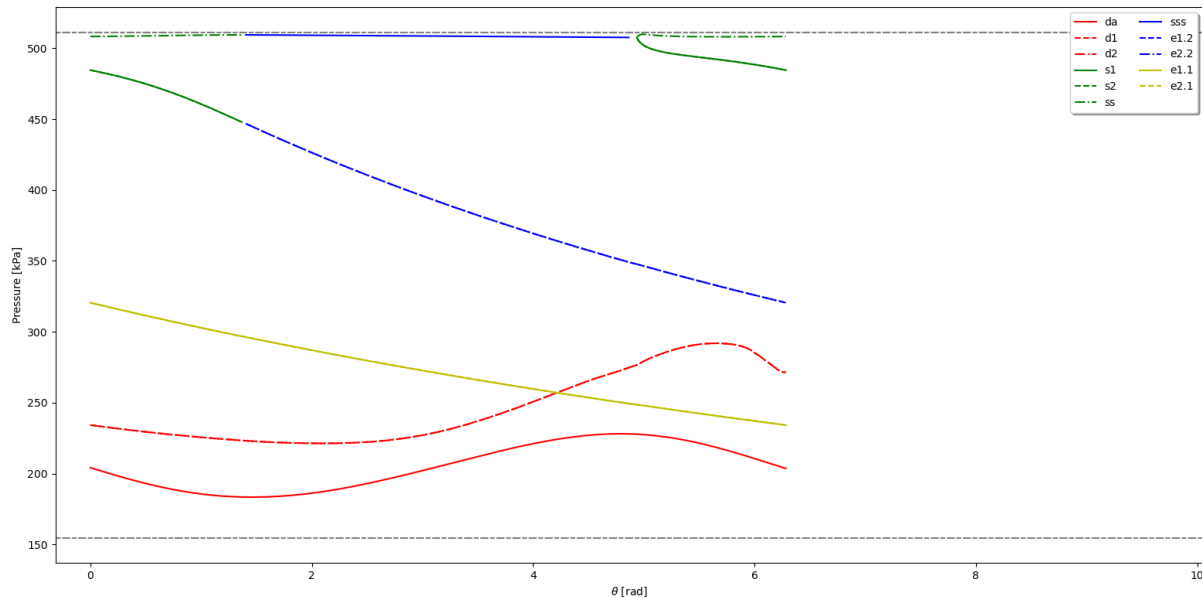
**Figure 62. Pressure distribution in scroll expander chambers as a function of the rotating angle (Case 1)**



**Figure 63.** Pressure distribution in scroll expander chambers as a function of the rotating angle (Case 2)



**Figure 64.** Pressure distribution in scroll expander chambers as a function of the rotating angle (Case 3)



**Figure 65. Pressure distribution in scroll expander chambers as a function of the rotating angle (Case 4)**

First of all, the subsequent graphs (Figure 66, Figure 67, Figure 68, Figure 69) illustrate the values of pocket's volumes throughout the overall expansion procedure. Taking into consideration the following figures, the volume values do not differ significantly among the cases. However, the split and the discharge angles are presented in divergent rotating angles in the same way as the corresponding pressure graphs. It is also observed that in all cases there is a discontinuity in the volume lines that refer to sss and ss,  $s_1$  and  $s_2$  pockets in the split angle. That is because the sss chamber is divided into ss and  $s_1$  and  $s_2$  equally. Furthermore, in both suction and expansion stages the volumes in the expander chambers increase gradually facilitating the electrical work generation. In terms of the discharge volumes, it should be mentioned that at the beginning of the rotation the volumes in the discharge area (da) undergo a marked growth, and then, they experience a downward trend that is due to the important decrease of the volumes in chambers  $d_1$  and  $d_2$ . This is also the reason why the pressures in the above line graphs rise in the discharge pockets for all cases. The values of the volumes that are dominant in each chapter of every case are disclosed due to confidentiality reasons.

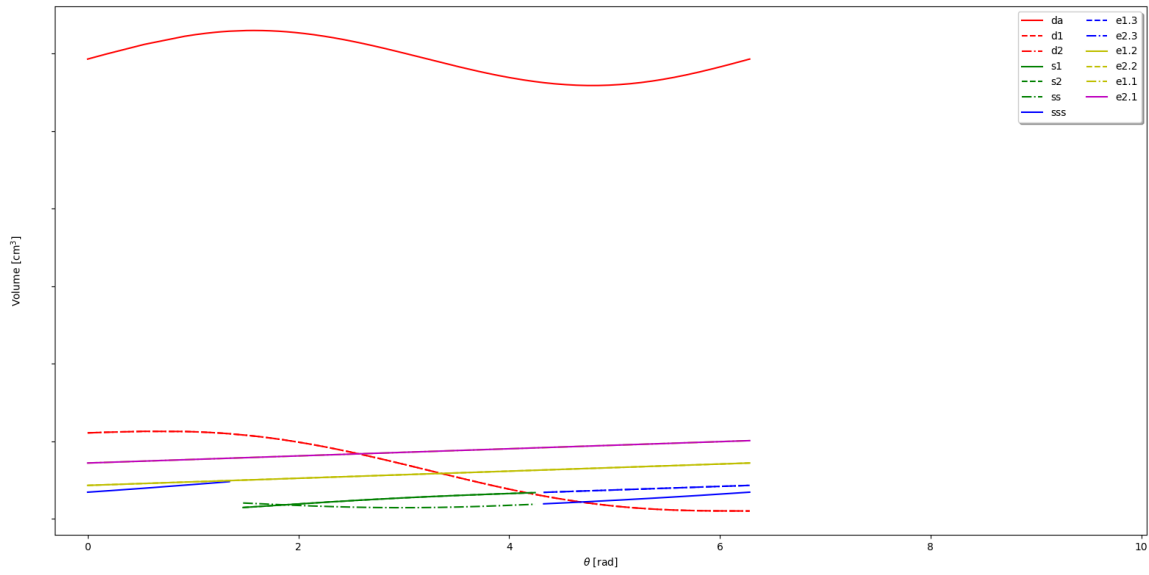


Figure 66. Volume changes in scroll expander chambers as a function of the rotating angle (Case 1)

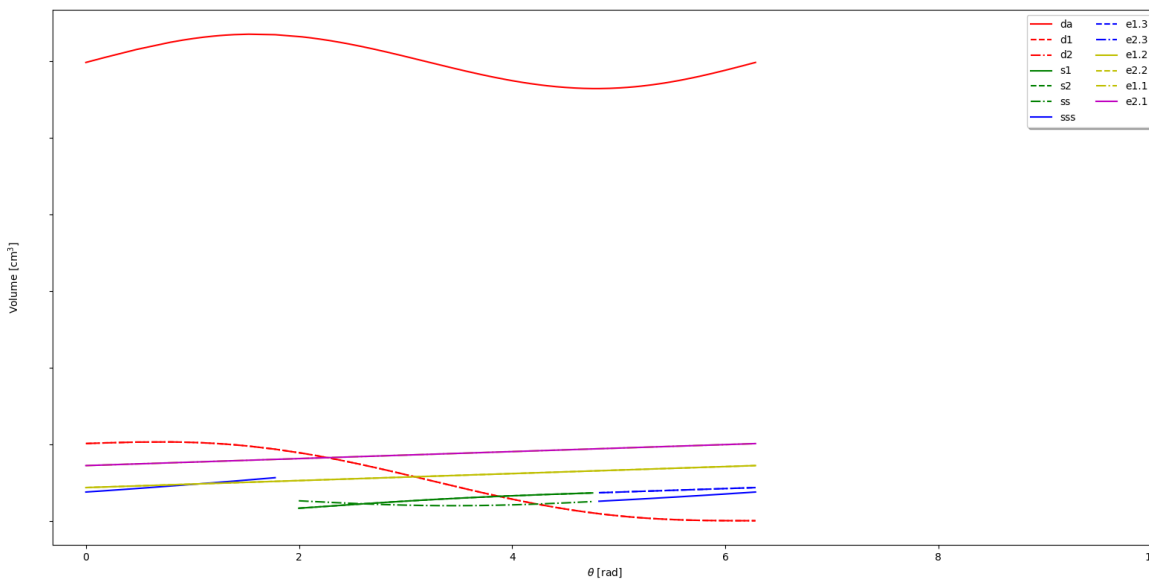
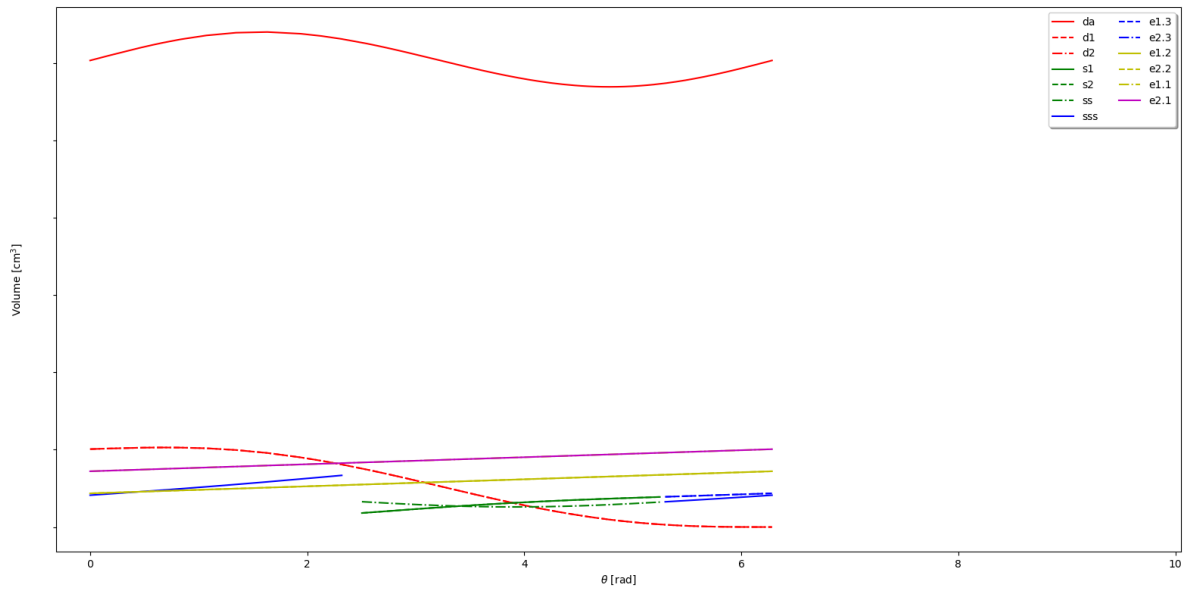
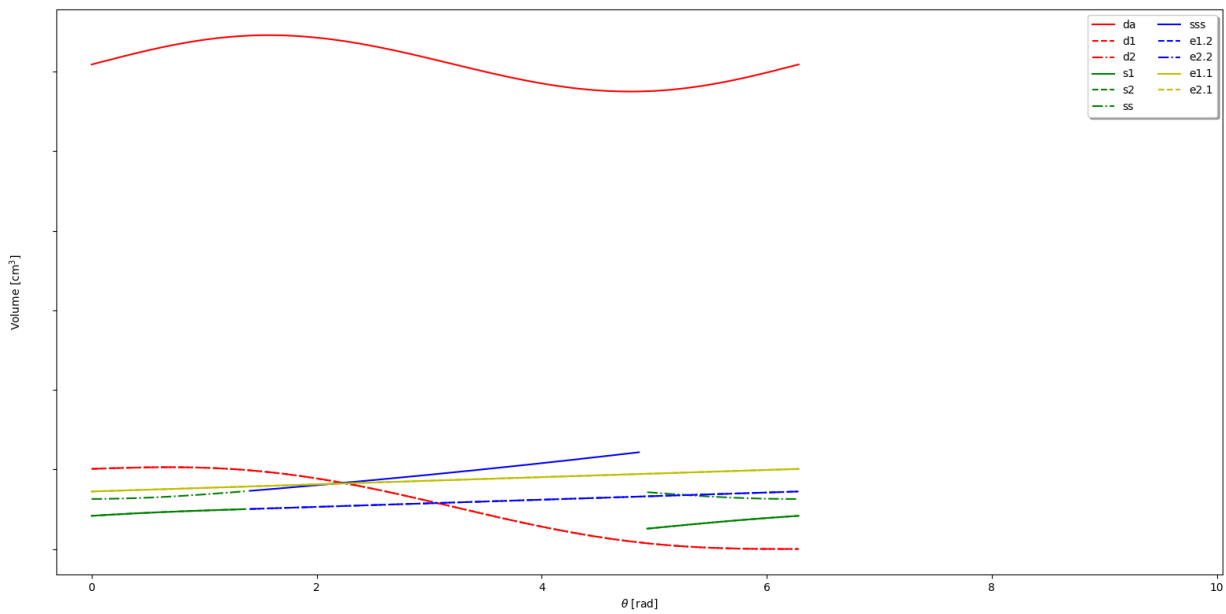


Figure 67. Volume changes in scroll expander chambers as a function of the rotating angle (Case 2)



**Figure 68. Volume changes in scroll expander chambers as a function of the rotating angle (Case 3)**

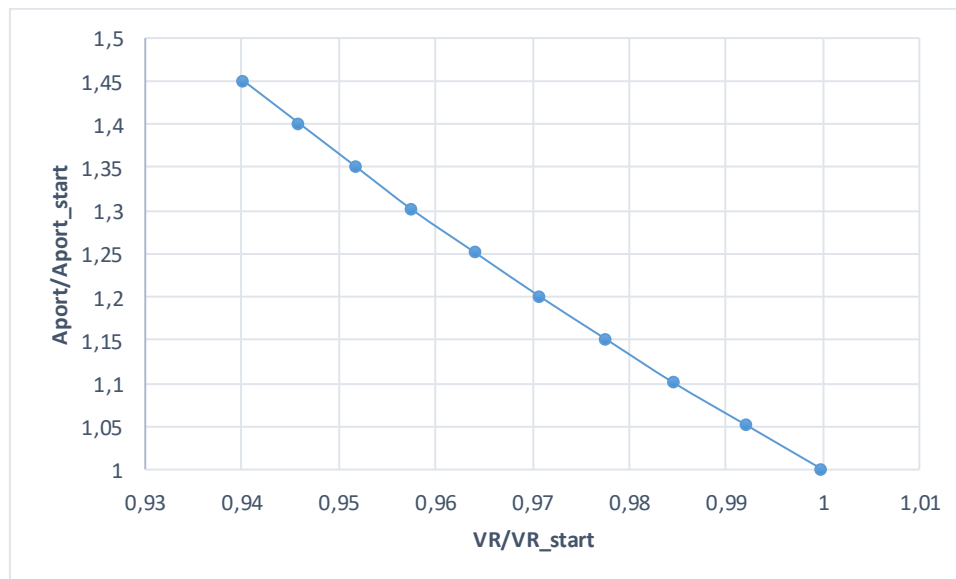


**Figure 69. Volume changes in scroll expander chambers as a function of the rotating angle (Case 4)**

### 3.2.2 Investigation of inlet port area and built-in volume ratio

Taking into consideration the results of the section 3.2.1,  $\varphi_{i_s}$  and  $\varphi_{o_s}$  are fixed and equal to those corresponding to Case 2. To achieve the adiabatic efficiency maximization, an investigation between the Cases 2 and 3 is conducted. In this analysis, both inlet port area and volume ratio change simultaneously, with change step of the former being equal to 10mm. Moreover, the operational conditions are the same as those described in the section 3.1.

As it can be seen clearly from Figure 70, the inlet port area experiences a downward trend as a function of the built-in volume ratio. It is noted that the exact values of these parameters are not given due to the confidentiality of project Regen by 2. As a result, the values of inlet port area and volume ratio are illustrated in a nondimensional form, by dividing each variable with the initial ones.



**Figure 70. Correlation between the inlet port area and the volume ratio in a nondimensional form**

Therefore, the equation that describes the relationship between the inlet port area and volume ratio is the following:

$$A_{port} = a \times e^{-b \times VR} \quad 3.1$$

Where VR constitutes the volume ratio and a, b are constant values obtained from the production company.

In terms of the adiabatic efficiency, the respective feature undergoes a marked rise for the first two values of inlet port area, while it drops considerably as the inlet port area grows (Figure 71). The exact opposite trend of the adiabatic performance is presented in Figure 72. The adiabatic efficiency is maximized for a built-in volume ratio, for which the filling factor approaches unity. More specifically, the maximum adiabatic performance amounts to 81.83%. Moreover, it can be observed that for the lowest inlet port areas and highest volume ratios, the adiabatic performance drops. These downward trends are due to the suction pressure drops. In particular, as the inlet port diameter becomes smaller, the pressure drops that occur between the suction line and suction chamber deteriorate. Note also that the increase in the volume ratio entails the increase in the length of the scroll wraps, and in turn, results in increased leakage losses. Therefore, a decrease approximately 0.3% in adiabatic efficiency takes place when the inlet port area reaches the starting value. However, the adiabatic performance undergoes an abrupt decline by increasing the inlet port area or decreasing the volume ratio below the built-in volume ratio. Since the increase in the inlet port area entails the growth of the suction volume, and consequently, the ratio of discharge and suction volumes declines. In other words, it drops from 81.83% to 79.54% because of the over-expansion that happens in volume ratios lower than the internal ratio of the scroll expander. The fact that the pressure in the discharge line is higher than the pressure in the chamber situated at the end of the expansion provokes the expander's under filling affiliated with negative repercussions on the adiabatic performance. That means that the losses connected with over-expansion are more severe than those derived from under-expansion. It should be mentioned that if the imposed volume ratio is close to the built-in volume ratio, either the over-expansion losses or the under-expansion losses are minimized. These results can also be verified from the related literature. [30], [34], [52]

The volumetric efficiency increases with the inlet port area. More specifically, for the starting value of inlet port area, it is 77.6% while it is increased to 80.52% for the latest port area value. As the port diameter is increased, the working fluid mass flow rate is increased at a higher rate than the ratio of the displacement volume to volume ratio. As a result, based on equation 2.44, when the built-in volume ratio is increased, it exerts negative impacts on the volumetric efficiency. Finally, it is also essential that a higher built-in volume ratio of a scroll expander leads to higher pressure difference between the expander suction and discharge chambers, hence causing increased leakages. Consequently, the mass flow rate is reduced because of the increase in the leakage flow, leading to lower values of volumetric performance.



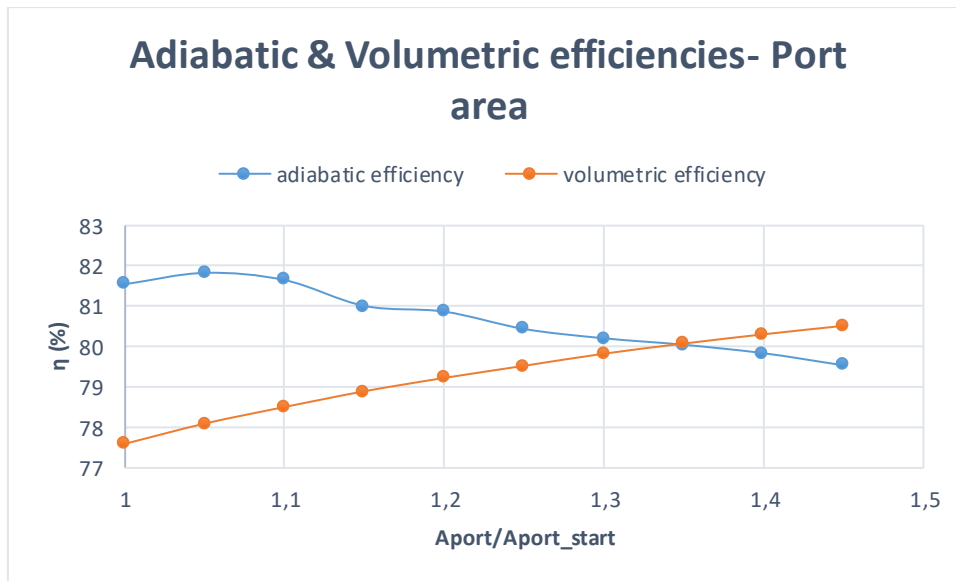


Figure 71. Adiabatic and Volumetric efficiency as functions of the nondimensional inlet port area for an investigation between Case 2 and Case 3

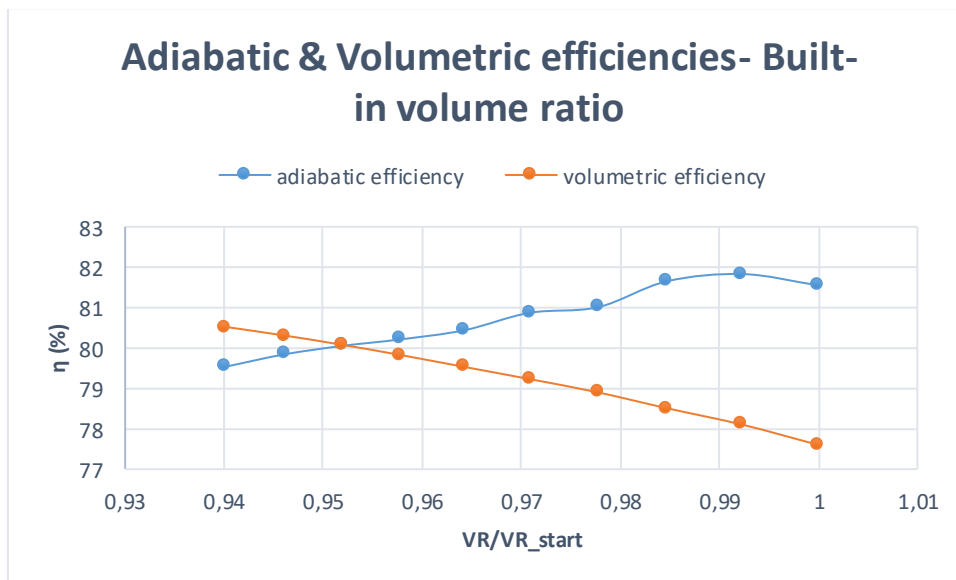


Figure 72. Adiabatic and Volumetric efficiency as functions of volume ratio for an investigation between Case 2 and Case 3

## 4. Discussion

In this work, a deterministic model is developed in order to describe the expansion of pure R1233zd(E) in the two-phase region. To achieve this, the existing open-source PDSim is modified by adding the heat transfer and flow models. Through a series of sensitivity analysis involving divergent pressure ratios, inlet vapor qualities and rotational speeds, this deterministic model is applied in order to examine the performance of a commercial scroll expander and the way that it is influenced by of the various types of internal losses. Subsequently, the model is executed for the single-phase of R1233zd(E) to compare the results connected with the expander efficiency with the respective of those affiliated with the two-phase expansion. In the next stage, the geometrical model of a prototype expander is introduced to investigate the impacts of the involute angles and inlet port area on the adiabatic and volumetric efficiencies of the scroll expander. Finally, for fixed involute angles, the inlet port area and the built-in volume ratio are changed simultaneously, and thus, the adiabatic and volumetric performance are expressed as functions of them.

Based on the results, a positive correlation between the isentropic efficiency of the commercial expander and the inlet vapor ratio can be observed. More specifically, if all internal losses modules are activated and the inlet vapor quality fluctuates from 0.65 to 0.85, the isentropic performance varies between almost 59% and 65% correspondingly. The same trend can be mentioned also for the isentropic efficiency as a function of the pressure ratio. Namely, the isentropic performance amounts to a little less than 56% for a pressure ratio of 2.5 and undergoes an increase until it reaches approximately 61% for pressure ratio equal to 4.75, peaking at 66% when pressure ratio is almost 3.75. In terms of rotational speed, the increase of this variable entails the decline of the isentropic efficiency. In other words, in case of including the total losses, this performance reaches just above 78% for 3000 rpm, whereas after being subjected into a downward trend, it stands at around 65%. However, if a single-phase expansion occurs, the isentropic efficiency experiences a marked decrease, reducing from 76% to 71% for pressure ratios 2.5 and 5.38 respectively. That means that although the increase in the mass flow rate in the case of the wet expansion, the expander yields better efficiencies for the single-phase conditions.

First of all, according to the results of this work, the existence of the internal losses leads to the isentropic efficiency penalization only for pressure ratios lower than its design point. In other words, they deteriorate the over-expansion losses and the under-expansion losses remain almost intact. It can be also observed that the tube heat transfer losses exert a negligible influence on the isentropic efficiency when compared to pressure drop and leakage losses. However, the maximum deviation reaches only 3%. The drop of the isentropic efficiency due to the tube heat transfer is also insignificant. The main reason why the effects of internal losses are insignificant is that the correlations implemented for the description of heat transfer,

leakages and pressure drop losses introduce empirical and semi-empirical variables and it is difficult to be fully representative without being calibrated by accurate experimental data.

By using the geometrical model of the prototype scroll expander and increasing both the starting inner and outer involute angles and the inlet port area, the changes that happen in the adiabatic and volumetric efficiencies are investigated. More precisely, by means of adiabatic efficiency, the respective percentage goes up from 78% to almost 82%, and then it decreases until it reaches 65%. On the other hand, the volumetric performance is influenced positively by these alterations, being increased from 69% to 85% as these geometrical parameters grow. Finally, by using fixed values of the starting angles of both inner and outer involutes, the inner port area and the built-in volume ratio are changed. It should be mentioned that these parameters follow opposite trends. As the inlet port area rises, the adiabatic performance rises from 81.5% to just below 82%. The adiabatic efficiency peaks at almost 82%, when the pressure ratio is almost the same with the design one. For higher inlet port areas, the adiabatic performance drops. These results are in line with the literature, namely with studies Lemort et al. (2009) [30], Ziviani et al. (2017) [34] and [52], as it has been described in detail in section 3.2.2. At the other end of the spectrum, the volumetric performance is subject to a gradual decline with the increase of the built-in volume ratio, taking values between 77.6% and 80.5%.

## 5. Future work

The existed modified PDSim model renders the calculation of the two-phase expansion of pure R1233zd(E) feasible. However, in terms of the two-phase expansion of refrigerant-oil mixtures, in order for the thermodynamic properties of R1233zd(E)-oil mixtures to be determined by the model, additional fluid data is required associated with the thermodynamic properties of the used oil. Consequently, this data should be integrated into the PDSim model so as to calculate the scroll expander performance taking into account the oil properties for a specific oil fraction.

Moreover, several key variables of this model should be validated and calibrated relied on experimental results. More specifically, some used parameters are retrieved from empirical or semi-empirical models. To certify the model's accuracy in estimating the scroll expander's efficiencies, these variables should be verified by carrying out some experimental tests or by applying computational fluid dynamics (CFD) methods. These parameters referred to the evaporation and condensation heat transfer correlations in the tubes and the scroll chambers as well as to the pressure drops correlations in the tubes. Furthermore, the experimental tests or the numerical analysis could ensure that both non-homogenous flow impacts and differences between the transport properties of pseudo-pure fluids and real fluids for refrigerant-oil mixtures would be involved in the heat transfer and pressure drop equations.

## 6. List of Tables

Table 1. Working range for innovative scroll, screw and piston expanders [5] .....	17
Table 2. Non-exhaustive list of theoretical studies on expanders .....	31
Table 3. Non-exhaustive list of experimental studies on expanders.....	38
Table 4. Coefficients used for the radial leakage model .....	52
Table 5. Coefficients used for the flank leakage model .....	53
Table 6. Operating conditions of the expansion.....	63

## 7. List of Figures

Figure 1.Types of expanders [2] .....	13
Figure 2.Typical schematic of a scroll expander [6] .....	15
Figure 3.The principle of a single- screw expander [8] .....	15
Figure 4.Schematic of piston expander structure [14] .....	17
Figure 5.Operating principle of a scroll expander [15] .....	18
Figure 6.Under (a) and over (b) expansion losses [15] .....	19
Figure 7.Flank and radial leakages occurring in a scroll expander [17] .....	19
Figure 8.Vapor Compression Cycle configuration using expansion valve .....	20
Figure 9.P-h diagram for Vapor Compression Cycle .....	21
Figure 10.Typical ORC configuration .....	22
Figure 11.T-s diagrams for neopentane, n-Pentane, R1233zd(E), R1234ze(Z) and R245fa .....	23
Figure 12.Computational domain of Wei’s scroll expander model [20] .....	24
Figure 13.Scroll expander efficiencies for different suction pressures [21] .....	25
Figure 14.Scroll expander efficiencies for different discharge pressures [21] .....	25
Figure 15.Fluctuation of expansion ratio due to the change in rotating speed [22] .....	26
Figure 16.Fluctuation of isentropic indicated efficiency due to the change in rotating speed [22] .....	26
Figure 17.The variation of isentropic and volumetric efficiencies with the concurrent increase of the suction pressure [23] .....	27
Figure 18.Computational unstructured mesh of the scroll expander [27] .....	27
Figure 19.Pressure distribution in the working chambers on a cross-section area perpendicular to z-axis [27] .....	28
Figure 20.Scroll efficiencies as a function of expansion ratio for the short scroll expander [28] .....	29
Figure 21.Scroll efficiencies as a function of expansion ratio for the long scroll expander .....	29
Figure 22.Micro-CHP configuration [28] .....	30
Figure 23.Types of volumetric expanders [29] .....	32
Figure 24.T-s diagram of Miao et al. ORC configuration [31] .....	33
Figure 25.Expander shaft power as a function of air temperature and R123 mass flow rate [31] .....	34
Figure 26.The effects of internal losses on expander isentropic efficiency for rotational speeds of 3000rpm [32] .....	34
Figure 27.Total isentropic efficiency (circle markers) and cycle efficiency (triangle markers) for three expander build-in volume ratios and different pressure ratios [34] .....	35
Figure 28.Structure of the Lei’s single screw expander prototype [9] .....	36
Figure 29.Expander isentropic efficiency for divergent expansion ratios, vapor temperatures and pump rotational speed equal to (a) 300 rpm and (b) 400 rpm [36] .....	37
Figure 30.Isentropic efficiency of expander as a function of the pressure ratio for a range of rotational speeds and inlet pressures [37] .....	37

Figure 31.Lemort’s semi- empirical model of a scroll expander [30] .....	42
Figure 32.A common class in PDSim for a compressor or an expander model.....	43
Figure 33.Pheudo-code of a compressor in Python-like form [48] .....	44
Figure 34.Scroll expander’s generated chambers during one rotation [50] .....	45
Figure 35.The illustration of the two-arc geometry [47] .....	47
Figure 36.The geometric parameters of an Arc-Line-Arc machine [47].....	48
Figure 37.Mass flow ratio calculations for the radial leakages depending on the Reynolds number and the radial leakage gap [47] .....	51
Figure 38.Mass flow ratio calculations for the flank leakages depending on the Reynolds number and the radial leakage gap [47] .....	53
Figure 39.Deterministic model solver .....	60
Figure 40.Isentropic and volumetric efficiencies as functions of the inlet vapor quality for activated and deactivated heat transfer and a fixed pressure ratio .....	64
Figure 41.Isentropic and volumetric efficiencies as functions of the pressure ratio for activated and deactivated heat transfer and a fixed inlet vapor quality .....	65
Figure 42.Isentropic and volumetric efficiencies as functions of the inlet vapor quality for activated and deactivated pressure drop and a fixed pressure ratio .....	67
Figure 43.Isentropic and volumetric efficiencies as functions of the pressure ratio for activated and deactivated pressure drop and a fixed inlet vapor quality .....	67
Figure 44.Isentropic and volumetric efficiencies as functions of the inlet vapor quality for activated and deactivated leakages and a fixed pressure ratio .....	68
Figure 45.Isentropic and volumetric efficiencies as functions of the pressure ratio for activated and deactivated leakages and a fixed inlet vapor quality .....	69
Figure 46.Isentropic and volumetric efficiencies as functions of the inlet vapor quality for activated and deactivated total internal losses and a fixed pressure ratio .....	70
Figure 47.Isentropic and volumetric efficiencies as functions of the pressure ratio for activated and deactivated total internal losses and a fixed inlet vapor quality .....	71
Figure 48.Pressure distribution in scroll expander chambers as a function of the rotating angle for 3000 rpm .....	72
Figure 49.Pressure distribution in scroll expander chambers as a function of the rotating angle for 6000 rpm .....	72
Figure 50.Isentropic efficiency as a function of the rotating speed for activated and deactivated both leakages and heat transfer, fixed inlet vapor quality and enabled pressure ratio .....	73
Figure 51.Volumetric efficiency as a function of the rotating speed for activated and deactivated both leakages and heat transfer, fixed inlet vapor quality and enabled pressure ratio .....	73
Figure 52.Isentropic efficiency as a function of the rotating speed for activated and deactivated both leakages and heat transfer, fixed inlet vapor quality and disactivated pressure ratio .....	74
Figure 53.Volumetric efficiency as a function of the rotating speed for activated and deactivated both leakages and heat transfer, fixed inlet vapor quality and disactivated pressure ratio .....	74
Figure 54.Mass flow rate and volumetric performance as functions of pressure ratio for both single-phase and two-phase flows, leakages off, heat transfer off, pressure drop off.....	75

Figure 55. Electrical power and isentropic performance as functions of pressure ratio for both single-phase and two-phase flows, leakages off, heat transfer off, pressure drop off.....	76
Figure 56. Pressure distribution in scroll expander chambers as a function of the rotating angle for the single-phase flow .....	76
Figure 57. Pressure distribution in scroll expander chambers as a function of the rotating angle for the two-phase flow .....	77
Figure 58. Mass flow rate and volumetric performance as functions of pressure ratio for both single-phase and two-phase flows, leakages on, heat transfer on, pressure drop on.....	77
Figure 59. Electrical power and isentropic performance as functions of pressure ratio for both single-phase and two-phase flows, leakages on, heat transfer on, pressure drop on.....	78
Figure 60. (a) Adiabatic and (b) volumetric efficiency for each geometry case .....	79
Figure 61. Produced electrical power for the four applied cases .....	80
Figure 62. Pressure distribution in scroll expander chambers as a function of the rotating angle (Case 1).....	82
Figure 63. Pressure distribution in scroll expander chambers as a function of the rotating angle (Case 2).....	83
Figure 64. Pressure distribution in scroll expander chambers as a function of the rotating angle (Case 3).....	83
Figure 65. Pressure distribution in scroll expander chambers as a function of the rotating angle (Case 4).....	84
Figure 66. Volume changes in scroll expander chambers as a function of the rotating angle (Case 1) .....	85
Figure 67. Volume changes in scroll expander chambers as a function of the rotating angle (Case 2) .....	85
Figure 68. Volume changes in scroll expander chambers as a function of the rotating angle (Case 3) .....	86
Figure 69. Volume changes in scroll expander chambers as a function of the rotating angle (Case 4) .....	86
Figure 70. Correlation between the inlet port area and the volume ratio in a nondimensional form.....	87
Figure 71. Adiabatic and Volumetric efficiency as functions of the nondimensional inlet port area for an investigation between Case 2 and Case 3 .....	89
Figure 72. Adiabatic and Volumetric efficiency as functions of volume ratio for an investigation between Case 2 and Case 3.....	89





## 8. References

- [1] Plant Engineer's Handbook, DENNIS A SNOW, 2002.
- [2] A. P. Weiss, "VOLUMETRIC EXPANDER VERSUS TURBINE-WHICH IS THE BETTER CHOICE FOR SMALL ORC PLANTS," in *3rd International Seminar on ORC Power Systems*, Brussels, Belgium, 2015.
- [3] R B Peterson, H Wang, T Herron, "Performance of a small-scale regenerative Rankine power cycle employing a small expander," *P. I. Mech. Eng. A-J. Pow.*, pp. 271-282, 2008.
- [4] Panpan Song, Mingshan Wei, Lei Shi, Syed Noman Danish, Chaochen Ma, "A review of scroll expanders for organic Rankine cycle systems," *Applied Thermal Engineering*, pp. 54-64, 2015.
- [5] O. Dumont, L. Talluri, D. Fiaschi, G. Manfrida, V. Lemort, "Comparison of a scroll, a screw, a roots, a piston expander and a Tesla turbine for small-scale organic Rankine cycle," in *Paper ID: 14Page 15thInternational Seminar on ORC Power Systems*, Athens, Greece, 2019.
- [6] Pardeep Garg, G.M. Karthik, Prashant Kumar, Pramod Kumar, "Development of a generic tool to design scroll expanders for ORC," *Applied Thermal Engineering*, pp. 878-888, 2016.
- [7] Biao Lei, Wei Wang, Yu-Ting Wu, Chong-Fang Ma, Jing-Fu Wang, Lei Zhang, Chuang Li, Ying-Kun Zhao, Rui-Ping Zhi, "Development and experimental study on a single screw expander," *Energy*, pp. 43-52, 2016.
- [8] A. S. Panesar, "A study of organic Rankine cycle systems with the expansion process performed by twin screw machines," Brighton, East Sussex, United Kingdom, 2012.
- [9] Biao Lei, Wei Wang, Yu-Ting Wu, Chong-Fang Ma, Jing-Fu Wang, Lei Zhang, Chuang Li, Ying-Kun Zhao, Rui-Ping Zhi, "Development and experimental study on a single screw expander integrated into an Organic Rankine Cycle," *Energy*, vol. 116, pp. 43-52, 2016.
- [10] Guoqiang Li, Yuting Wu, Ye qiang Zhang, Ruiping Zhi, Jingfu Wang and Chongfang Ma, "Performance Study on a Single-Screw Expander for a Small-Scale Pressure Recovery System," *Energies*, 2017.
- [11] Guoqiang Li 1, Yuting Wu, Ye qiang Zhang, Ruiping Zhi, Jingfu Wang and Chongfang Ma, "Performance Study on a Single-Screw Expander for a Small-Scale Pressure Recovery System," *Energies*, Vols. 10,6, 2017.

- 
- [12] V. Lemort, G. Ludovic, A. Legros, S. Declaye, S. Quoilin, "A comparison of piston, screw and scroll expanders for small scale Rankine cycle systems," in *Proceedings of the 3rd International Conference on Microgeneration and Related Technologies*, 2013.
- [13] B. Zhang, X. Peng, Z. He, Z. Xing, P. Shu, "Development of a double acting free piston expander for power recovery in transcritical CO<sub>2</sub> cycle," *Applied Thermal Engineering*, vol. 27, pp. 1629-1636, 2007.
- [14] B.Zhang,X.Peng,Z.He,Z.Xing,P.Shu, "Development of a double acting free piston expander for power recovery in transcritical CO<sub>2</sub> cycle," *Applied Thermal Engineering*, vol. 27, no. 8-9, pp. 1629-1636, 2007.
- [15] Fadhel Ayachi, Elias Boulawz Ksayer, Pierre Neveua, Assaad Zoughaib, "Experimental investigation and modeling of a hermetic scroll expander," *Applied Energy*, pp. 256-267, 2016.
- [16] Sylvain Quoilina, Martijn Van Den Broekb, Sébastien Declaye, Pierre Dewallef, Vincent Lemort, "Techno-economic survey of Organic Rankine Cycle (ORC) systems," *Renewable and Sustainable Energy Reviews*, pp. 168-186, 2013.
- [17] A. Iglesias, D. Favrat, "Innovative isothermal oil-free co-rotating scroll compressor–expander," *Energy Conversion and Management*, pp. 565-572, 2014.
- [18] S. Lecompte, B. Ameel, D. Ziviani, M. van den Broek, M. De Paepe, "Exergy analysis of zeotropic mixtures as working fluids in Organic Rankine Cycles," *Energy Conversion and Management*, vol. 85, p. 727–739, 2014.
- [19] Panpan Song, Mingshan Wei, Zhen Liu, Ben Zhao, "Effects of suction port arrangements on a scroll expander for a small scale ORC system based on CFD approach," *Applied Energy*, vol. 150, pp. 274-285, 2015.
- [20] Mingshan Wei, Panpan Song, Ben Zhao, Lei Shi, Zhixing Wang, Chaochen Ma, "Unsteady flow in the suction process of a scroll expander for an ORC waste heat recovery system," *Applied Thermal Engineering*, vol. 78, pp. 460-470, 2015.
- [21] Hyun Jin Kim, Jong Min Ahn, Sung Oug Cho, Kyung Rae Cho, "Numerical simulation on scroll expander–compressor unit for CO<sub>2</sub> trans-critical cycles," *Applied Thermal Engineering*, vol. 28, p. 1654–1661, 2008.
- [22] Gao Xiaojun, Li Liansheng, Zhao Yuanyang, Shu Pengcheng, "Research on a Scroll Expander Used for Recovering Work in a Fuel Cell," *Thermodynamics*, vol. 7, pp. 1-8, 2004.

- [23] L. Guangbin, Z. Yuanyang, L. Yunxia<sup>1</sup>, and L. Liansheng, "Simulation of the dynamic processes in a scroll expander-generator used for small-scale organic Rankine cycle system," *Power and Energy*, vol. 225, pp. 141-149, 2011.
- [24] LWang,Y Zhao, L Li,GBu,andPShu, "Research on oil-free hermetic refrigeration scroll compressor," *Power and Energy*, vol. 221, pp. 1049-1056, 2007.
- [25] Gu, Z. L., Yu, Y. Z., and Feng, S. Y., Scroll compressor and other scroll machines, China: Shaanxi Science and Technology Press, 1998.
- [26] Yu Chen, Nils P. Halm, Eckhard A. Groll, James E. Braun, "Mathematical modeling of scroll compressors—part I: compression process modeling," *Refrigeration*, vol. 25, pp. 731-750, 2002.
- [27] P P Song, M S Wei, L Shi and C C Ma, "Numerical simulation of three-dimensional unsteady flow in a scroll expander applied in waste heat recovery," in *IOP Conference Series Materials Science and Engineering*, 2013.
- [28] Stefano Clemente, Diego Micheli, Mauro Reini, Rodolfo Taccani, "Energy efficiency analysis of Organic Rankine Cycles with scroll expanders for cogenerative applications," *Applied Energy*, vol. 97, pp. 792-801, 2012.
- [29] Olivier Dumont, Antoine Parthoens, Rémi Dickes, Vincent Lemort, "Experimental investigation and optimal performance assessment of four volumetric expanders (scroll, screw, piston and roots) tested in a small-scale organic Rankine cycle system," *Energy*, vol. 165, pp. 1119-1127, 2018.
- [30] Vincent Lemort, Sylvain Quoilin, Cristian Cuevas, Jean Lebrun , "Testing and modeling a scroll expander integrated into an Organic Rankine Cycle," *Applied Thermal Engineering*, vol. 29, p. 3094–3102, 2009.
- [31] Zheng Miao, Jinliang Xu, Kai Zhang, "Experimental and modeling investigation of an organic Rankine cycle system based," *Energy*, vol. 134, pp. 35-49, 2017.
- [32] D. Ziviani, N. A. James, F. A. Accorsi, J. E. Braun, and E. A. Groll, "Experimental and numerical analyses of a 5 kWe oil-free open-drive scroll expander for small-scale organic Rankine cycle (ORC) applications," *Applied Energy*, vol. 230, p. 1140–1156, 2018.
- [33] Z. Liu, M. Wei, P. Song, S. Emhardt, G. Tian, and Z. Huang, "The fluid-thermal-solid coupling analysis of a scroll expander used in an ORC waste heat recovery system," *Applied Thermal Engineering*, vol. 138, p. 72–82, 2018.

- [34] Davide Ziviani, Sergei Gusev, Stefan Schuessler, Abdennace rAchaichia, James E.Braun, Eckhard A.Groll, Michel De Paepe, Martijnvan den Broek, "Employing a Single-Screw Expander in an Organic Rankine Cycle with Liquid Flooded Expansion and Internal Regeneration," *Energy Procedia*, vol. 129, pp. 379-386, 2017.
- [35] Fadhel Ayachi, Elias Boulawz Ksayer, Pierre Neveu, Assaad Zoughaib , "Experimental investigation and modeling of a hermetic scroll expander," *Applied Energy*, vol. 181, pp. 256-267, 2016.
- [36] Roberto Bracco, Stefano Clemente, Diego Micheli, Mauro Reini , "Experimental tests and modelization of a domestic-scale ORC (Organic Rankine Cycle)," *Energy*, vol. 58, pp. 107-116, 2013.
- [37] Sébastien Declaye, Sylvain Quoilin, Ludovic Guillaume, Vincent Lemort, "Experimental study on an open-drive scroll expander integrated into Experimental study on an open-drive scroll expander integrated into," *Energy*, vol. 55, pp. 173-183, 2013.
- [38] Hao Tang, Huagen Wu, Xiaolin Wang, Ziwen Xing , "Performance study of a twin-screw expander used in a geothermal," *Energy*, vol. 90, pp. 631-642, 2015.
- [39] S. M. E. Hoque, "Experimental Investigation of An R134a Based Organic Rankine Cycle," Master of Applied Science in The Faculty of Engineering and Applied Science Mechanical Engineering, University of Ontario Institute of Technology, 2011.
- [40] Liu Guangbin, Zhao Yuanyang, Yang Qichao, Wang Le, Tang Bin, Li Liansheng, "Theoretical and experimental research on scroll expander used in small-scale organic Rankine cycle system," *Process Mechanical Engineering*, no. <http://dx.doi.org/10.1177/0954408913506701>, 2013.
- [41] Muhyiddine Jradi, Jinxing Li, Hao Liu and Saffa Riffat, "Micro-scale ORC-based combined heat and power system using a novel scroll expander," *Low-Carbon Technologies*, vol. 9, pp. 91-99, 2014.
- [42] R. Zanelli, D. Favrat, "Experimental Investigation of a Hermetic Scroll Expander-Generator," in *International Compressor Engineering Conference*, Purdue, 1994.
- [43] M. Kane, D. Larrain, D. Favrat, Y. Allani , "Small hybrid solar power system," *Energy*, vol. 28, p. 1427–1443, 2003.
- [44] Takeo Saitoh, Noboru Yamada, Shin-ichiro Wakashima, "Solar Rankine Cycle System Using Scroll Expander," *Environment and Engineering*, vol. 2, pp. 708-719, 2007.

- [45] D. Manolakos, G. Papadakis, S. Kyritsis, K. Bouzianas, "Experimental evaluation of an autonomous low-temperature solar Rankine cycle system for reverse osmosis desalination," *Desalination*, vol. 203, pp. 366-374, 2009.
- [46] Naijun Zhou, Xiaoyuan Wang, Zhuo Chen, Zhiqi Wang, "Experimental study on Organic Rankine Cycle for waste heat recovery from low-temperature flue gas," *Energy*, vol. 55, pp. 216-225, 2013.
- [47] I. H. Bell, "THEORETICAL AND EXPERIMENTAL ANALYSIS OF LIQUID FLOODED COMPRESSION IN SCROLL COMPRESSORS," Purdue University, 2011.
- [48] Ian H. Bell, Davide Ziviani, Vincent Lemort, Craig R. Bradshaw, Margaret Mathison, W. Travis Horton, James E. Braun, Eckhard A. Groll, "PDSim: A general quasi-steady modeling approach for positive displacement compressors and expanders," *International Journal of Refrigeration*, vol. 110, pp. 310-322, 2020.
- [49] Davide Ziviani, Ian H. Bell, Xinye Zhang, Vincent Lemort, Michel De Paepe, James E. Braun, Eckhard A. Groll, "PDSim: Demonstrating the capabilities of an open-source simulation framework for positive displacement compressors and expanders," *International Journal of Refrigeration*, vol. 110, pp. 323-339, 2020.
- [50] Ian Bell, Vincent Lemort, Eckhard Groll, James E. Braun, Galen King, "Liquid-Flooded Compression and Expansion in Scroll Machines – Part I: Model Development," *International Journal of Refrigeration*, vol. 35, pp. 1878-1889, 2012.
- [51] [Online]. Available:  
<http://achp.sourceforge.net/ACHPComponents/FluidCorrelations.html#shah1976>.
- [52] Brandon J. Woodland, James E. Braun, Eckhard A. Groll, W. Travis Horton, "Experimental Testing of an Organic Rankine Cycle with Scroll-type Expander," in *International Refrigeration and Air Conditioning Conference*, Purdue, 2012.